CHARACTERISATION AND PROPERTIES IMPROVEMENT OF ARMOUR CERAMICS

By

OLANIYI SAMUEL FAKOLUJO, B.Sc., M.Sc.

Thesis submitted to the

Faculty of Graduate and Postdoctoral Studies

In partial fulfillment of the requirements

For the Doctorate in Philosophy degree in Advanced Materials and Manufacturing

Ottawa-Carleton Institute for Mechanical and Aerospace Engineering

Faculty of Engineering

University of Ottawa

ABSTRACT

As firearms continuously become more sophisticated, there have been commensurate efforts to optimize the ballistic performance of armours, with ceramic materials currently at the forefront of such studies. These efforts have focused on improving processing and microstructural design with reinforcements using dispersion particles, carbon nanotubes (CNT) and boron nitride nanotubes (BNNT). In most studies, ballistic testing has been used to identify parameters affecting the performance.

The research documented here focuses on: (1) the investigation of two commercial ceramics, namely silicon carbide (SiC) and zirconia toughened alumina (ZTA). The primary material properties evaluated for the characterization included: hardness, fracture toughness, flexural strength and Young's modulus. Other properties investigated included the microstructure, porosity/density, and mode of failure or fracture. (2) Ballistic depth of penetration (DOP) testing for six candidate ceramic armour systems including three monolithic ceramics (Al_2O_3, SiC and B_4C) and three nanotube toughened ceramic composites (Al_2O_3-BNNT, Al_2O_3-single walled CNT and SiC-BNNT).

SiC showed a hardness of 2413 HV, which is far beyond the requirements for armour ceramic. In contrast, ZTA barely met the hardness requirement of 1500 HV, but showed improved toughness of 4.90 MPa $m^{1/2}$ beyond values reported for monolithic alumina. SiC and ZTA showed that microstructural design improves fracture toughness but processing introduces defects that can substantially reduce other armour related properties such as the strength. The results of the Charpy and drop tower impact tests are in agreement with indentation fracture toughness results suggesting a great degree of reliability of this cost efficient method. The addition of nanotubes produced an increase in toughness and a decrease

in hardness in the ceramics, which resulted in an overall drop in performance during ballistic depth of penetration (DOP) tests. A microstructure-quasi-static mechanical properties-ballistic performance relationship was established which led to the development of a novel ballistic performance index and a new DOP model. The proposed ballistic performance index yielded a ranking, which agrees better with experimental observations than the currently published indices. The developed semi-empirical model suggests that the ballistic performance of ceramics is improved with increased fracture toughness, reduced flaw size and higher density.

ACKNOWLEDGEMENT

The journey of this doctorate program was facilitated with the backing of the Almighty God and people who contributed to my success in one form or another.

First and foremost, all glory for the accomplishment of this thesis goes to my creator, the Alpha and the Omega of everything good. He has provided me a wonderful opportunity to be a part of this program and He has supported me through this journey from start to finish.

My deep appreciation goes to my supervisors, Dr. Michel Nganbe and Dr. Ali Merati of National Research Council, (NRC) Montreal Road, Ottawa. Dr. Nganbe has been an exemplary supervisor, who has provided total support, guidance, counselling, patience and untiring assistance to see me through the program. I am also indebted to Dr. Merati, who provided the opportunity in the research field as well as providing facts, and above all his constructive criticisms have helped me a lot to accomplish the goal.

I would like to acknowledge the Defence R & D Canada (DRDC ValCartier), Quebec, Canada for providing the materials, data, as well as creating an enabling working environment. Similarly, I am very grateful to the National Research Council Canada (NRC), Aerospace Portfolio, for allowing the use of their facilities for the experimental work throughout the period of the program. In particular, I would like to thank Ms. Olga Lupandina and Mr. Richard Desnoyer, both staff of NRC for their great assistance on some aspects of the experimental work. Dr. Keun Su Kim of security & Disruptive Technologies Portfolio at NRC, was of great assistance in providing the nanotubes, the experimental work and proof-reading portion of the write-up on nanotubes.

I am also thankful to some staff and students of the University of Ottawa. Firstly Ms. Cynthia Bail, now ex-library assistance on Mechanical engineering subjects, for her untiring

assistance in guiding for the search of materials (publications). Secondly, two of my colleagues, now Dr. Shaba Hassan and Mr. Erfan Nazi, a Ph. D. candidate, for their invaluable inputs during the models' development and Mr. Richard York for last minutes editing of the thesis. To all the technical staff in the workshop I say "thank you".

My acknowledgement will be incomplete if I failed to express my heartfelt appreciation to my fathers-in-the-Lord: Bishop Jacob Afolabi, Pastor Cornelius Babalola, and Pastor Tunde Aribido for their inspirational words and prayer, which contributed immensely spiritually to see me through.

I would like to show my heartfelt gratitude to some special individuals who contributed to editing the work; Dr. David Adeosun (Guelph), in Canada, Dr. Tokunbo Makanju of Dalhousie University in Nova Scotia, Canada and Dr. Adeyemi Esuola (Ottawa). Also, to Prof. Chidi Oguamanam, a professor of law at the University of Ottawa, I say "thank you" for his counselling and words of encouragement.

I am highly indebted to my incredible friend, Mr. Oladipo Salau, for his love, support and facilitation of financial support.

I also like to acknowledge the financial support of the Tertiary Education Trust Fund (TETFund) of Nigeria, as well as the provision of study leave granted by my employer, Yaba College of Technology, Nigeria.

Finally, I must give special recognition to my immediate family members, first of which is my best friend, my love, and chief adviser, Funmilayo Sarah Fakolujo, whose endless support, motivation and inspiration has been very helpful in the accomplishment of this task. To my children, Isaiah, for participating in a little way on the editing, Olayiwola and Rebecca, I say thank you. And to my dearest mum, Mrs. Adunola Beatrice Fakolujo, I say a big "thank

you" for your prayers, love and deepest affection, which contributed to my success in life. I also remember and appreciate my Dad late Pa John Olowookere Fakolujo for giving me a good foundation in life.

TABLE OF CONTENTS

LIST OF TABLES

LIST OF FIGURES

GLOSSARY:

Units and Notations

↑	% increase
↓	% decrease
μm	Micrometre
A	Armstrong
a	Half indent diagonal
a_f	Flaw size
A_D	Areal density
c	Crack length measured from the centre of an indent to the end of the crack in Vickers hardness test
c_v	Sonic velocity
cm	Centimetre
C_O	Wave propagation velocity
E	Young's modulus
E_o	Pore-free Young's modulus
g	Gram
GPa	Giga Pascal
I_D	D-band intensity
I_G	G-band intensity
J	Joule
Kgf	Kilogram force
K_{IC}	Fracture toughness
Km/s	Kilometre per second
l	Crack length measured from the the centre of an indent to the end of the crack in Vickers hardness test
m	Metre
mg.	Milligram
ml	Millilitre
mm	Millimetre

MPa	Mega Pascal
N	Newton
nm	Nanometre
P	Porosity
Pr	Depth of penetration with ceramic
Px	Depth of penetration without ceramic
R_D	Reduction in penetration depth
rpm	Rotation per minute
sccm	Standard cubic centimetre per minute
t_t	Thickness of ceramic tile
TD	Theoretical density
υ	Poisson ratio
V_L	Longitudinal velocity
V_{LO}	Pore-free longitudinal velocity
vol.	Volume
V_T	Transverse velocity
V_{TO}	Pore-free transverse velocity
wt.	Weight
η	Efficiency index
ρ	Density
ρ_b	Density of backing material
ρ_o	Pore-free density
ρ_t	Density of ceramic tile
σ_a	Applied stress
σ_c	Compressive strength
σ_f	Fracture strength

Nomenclature

Al_2O_3	Alumina
AP	Armour piercing

ASTM	American Society for Testing and Materials
B_4C	Boron carbide
BE	Ballistic efficiency
BeO	Berrylium oxide
BNNT	Boron nitride nanotubes
BOCVD	Induction heating boron oxide CVD
CaO	Calcium oxide
Ce	Cerium
CNT	Carbon nanotubes
CT	Critical thickness
Cu	Copper
CVD	Chemical vapour deposition
DEF	Differential efficiency factor
DOP	Depth of penetration
DTT	Drop tower test
EDS	Energy dispersive spectroscopy
FC	Failure-causing crack
Fe	Iron
Fe_2N	Iron Nitride
Fe_3C	Iron III chloride or cementite
Fe_3N	Iron Nitride
FGA	Functional graded armour
FGM	Functionally graded armour
h-BN	Hexagonal boron nitride
HIP	Hot isostatic pressed
HK	Knoop hardness
HP	Hot pressed
HV	Vickers hardness
I	Iodine
IG	Intergranular fracture
ISE	Indentation size effect

KV	Kilovolts
MEF	Mass efficiency factor
MgO	Magnesium oxide
Mn	Manganese
MnO_2	Manganese oxide
MWCNT	Multi-walled carbon nanotube
Nb	Niobium
NDE	Non-destructive evaluation
NIJ	National institute of justice
NiO	Nickel oxide
NRC	National research council
NRCan	Natural resources of Canada
OM	Optical microscopy
Pb	Lead
Pd	Palladium
PH	Precipitation hardening steel
PS	Pressureless sintered
RHA	Rolled homogeneous armour
RoR	Ring-on-ring
SE	Space efficiency
SEF	Stopping efficiency factor
SEM	Scanning electron microscopy
SiC	Silicon carbide
SiO_2	Silica
Sn	Tin
SPS	Spark plasma sintering
SWCNT	Single walled carbon nanotube
TE	Thickness efficiency
TEF	Total efficiency factor
TG	Transgranular fracture
TGA	Thermo-gravimetric analysis

Ti	Titanium
TiB_2	Titanium diboride
TiO_2	Titanium oxide
TOF	Time of flight
V	Vanadium
WC	Tungsten carbide
WS	Weight saving
XRD	X-ray diffraction
ZrO_2	Zirconia
ZTA	Zirconia toughened alumina

CHAPTER 1

INTRODUCTION

1.1 Background and Motivation

Bullet resistant vests were invented as a protective armour to enhance survivability from gun shots. They have witnessed dramatic improvements in response to ever-increasing sophistication of threats, leading to a transition from monolithic steel armours to composite armours with ceramic front plate [1]. The major problem with traditional steel armours was the weight penalty, which substantially affect mobility. Hence, lightweight and high hardness have made ceramics the materials of choice for protective armour systems [1]. Although, current ceramic armours provide high level of protection, the level of casualties could be reduced even further considering the ever increasing complexity of armour piercing (AP) projectiles. Also, modern fire arms are characterised by extreme rapid sequences of multiple shots, referred to as multi-hit [2]. As multi-hit and lightweight capabilities are becoming imperative when selecting armours, further optimisation of ceramics performance, especially, their fracture toughness is crucial.

Simulation studies as well as experimental tests to determine failure mechanisms during ballistic impact have helped to identify the roadmap for ceramic armour improvement [3, 4]. They showed that increasing fracture toughness and strength through the introduction of ceramic matrix composites and the improvement of manufacturing processes are the most promising ways forward [5-7]. Therefore, researchers, end users and manufacturers are working on developing reinforcements for ceramics, with the goal of improving their toughness and strength without compromising their lightweight attributes. So far, Carbon Nanotubes (CNTs) and Boron Nitride Nanotubes (BNNTs) have been identified as promising

candidates in this regard [5, 8]. Although SiC, Al_2O_3 and B_4C have been identified as good candidates for ceramic matrices, SiC and Al_2O_3 are preferred because of their better process ability and lower costs [9].

In line with fabrication process optimisations, the characterisation of mechanical properties has always been of great interest. Current standard characterisation methods, however, often lead to a strong variability in results [10-12]. It is well established that the method and results of property measurements depend strongly on the microstructure of the ceramic. Therefore, the characterisation of ceramics has attracted volumes of research contributions with the view to improve methodologies [13, 14]. For instance, ceramic hardness measurements are very inconsistent due to the indentation size effect (ISE). ISE is a phenomenon whereby the measured hardness varies greatly at low loads. Therefore, hardness values are often provided with reference to the test load used [10]. This inconsistency has led to the development of multiple models with the goal of providing some measurement reliability [13, 14]. Also, the measurement of the fracture toughness through the indentation method has attracted contributions that have so far produced a great deal of uncertainties [15].

Another field of research on armour ceramics improvement is determining the role of the microstructure and mechanical properties on ballistic performance using the depth of penetration (DOP) test method. The DOP test is an experimental ballistic test consisting in attaching a ceramic tile to a ductile backing material and firing at the assembly. This test has been found very effective to evaluate the relative ballistic performance and efficiency of ceramics on confined and metal-backed materials using performance indices. Chief among these performance indices are the differential efficiency factor (DEF) and the mass efficiency factor (MEF) [16, 17]. While it has been cautioned that using the same performance index on

soft-backed materials may be misleading [18], the application of DOP test results on soft-backed ceramic armours proved adequate.

Using the DOP results to correlate microstructure and quasi-static properties to performance has brought about useful information on microstructure correlations. The work of Krell [19] concluded that the microstructure is the main factor driving ballistic performance. In line with this, some studies have investigated the influence of inclusions [20], grain size, grain size variability [21, 22], and porosity [23]. Although studies have shown that quasi-static mechanical properties including; hardness, fracture toughness, fracture strength and Young's modulus are relevant to ballistic performance, the degree of their relevancy is still unknown. Currently, the compressive strength [16] and hardness [1, 24] are often used to screen ceramics. The importance of the Young's modulus was also recognised [19, 25] while the contribution of the fracture toughness is still unclear [19, 26-28]. Nevertheless, some studies indicated that a toughness increase can improve the multi-hit capability of ceramics [29-31]. The scope of this PhD-research work is summarised in Figure 1.1.

1.2 Objective of the Study

The overall objectives of this work are to: (1) Characterise armour related properties of zirconia toughened alumina (ZTA) and silicon carbide (SiC).(2) Characterise pristine carbon and boron nitride nanotubes (CNT and BNNT) and investigate their potential for toughening armour ceramics. And (3) correlate quasi-static mechanical properties and microstructure defects to DOP using experimental and modelling approaches.

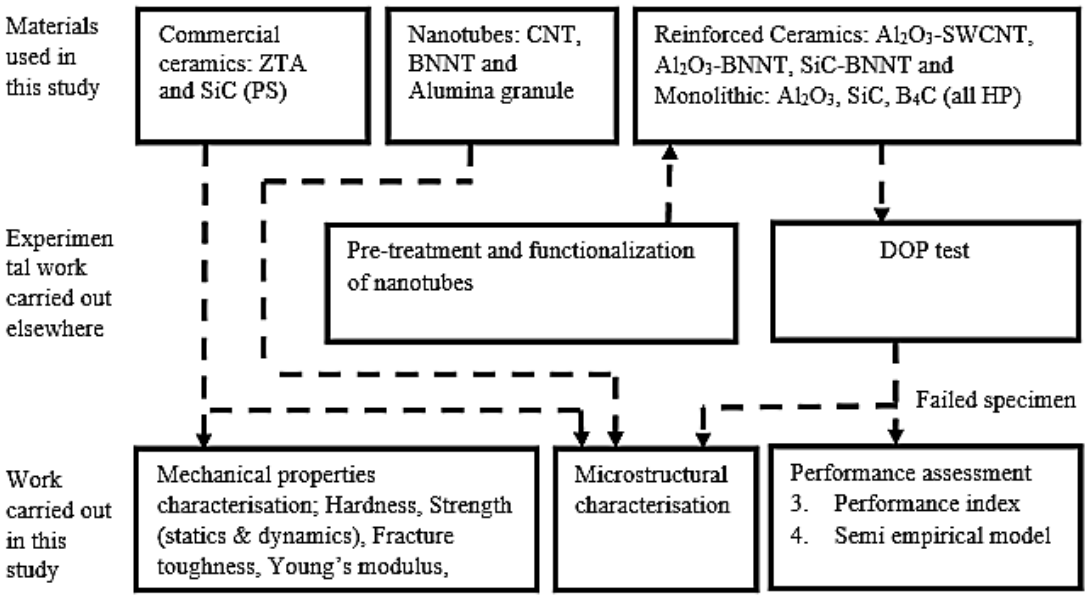

PS is pressureless sintered and HP is hot pressed.

Figure 1.1: Schematic of the optimisation chart used for improvement of ballistic performance of ceramic materials in this study.

Specific objectives of the study include:

i. Evaluating relevant quasi-static properties of zirconia toughened alumina and silicon carbide for armour performance and investigating the reliability of characterisation methods for mechanical properties.

ii. Improving methods for measuring the indentation fracture toughness of the above materials and relevant microstructural features.

iii. Contributing to the understanding of the role of microstructure in the property improvement and establishing microstructure-property relationships.

iv. Characterising the physical properties of Carbon nanotubes (CNT) and Boron Nitride nanotubes (BNNT), and establishing the influence of impurities and defects on processing and final mechanical properties.

v. Correlating microstructure and mechanical properties to ballistic performance (DOP).

CHAPTER 2

LITERATURE REVIEW

2.1 Ceramics in Armour Systems

Ceramics are a group of inorganic engineering materials consisting of metallic and non-metallic components. This group is characterised by interatomic bonds, which are either totally ionic or predominantly ionic while having some covalent characteristics. The term ceramics comes from the Greek word "keramikos", which means "burnt stuff", thus indicating that the desirable properties of these materials are normally achieved through a high temperature firing (Fig. 2.1) [32]. Ceramics can be further classified as: oxides, carbides, nitrides, glass, carbon and graphite, porcelain and ceramic fibres. They can also be more broadly classified as traditional or advanced engineering ceramics. The advanced ceramics group is further classified based on material's functional properties such as: thermal-chemical, mechanical, thermal conductive, electrical, magnetic and electromagnetic. Of these classes, armour ceramics belong to the advanced group designed for high strain rate impact loading. The properties needed for such a function include: high modulus of elasticity, high compressive strength, high hardness, wear resistance and, above all, light weight [32].

One of the greatest challenges of using armour ceramics lies in overcoming their poor tensile strength and low toughness when compared to metals [33]. The poor tensile strength is primarily due to inherently low dislocation density and the fact that, unlike metals, they feature very few slip planes for plastic deformation [33]. As a result of poor deformation, armour ceramics have a low energy absorbing capability and can therefore fail catastrophically under loading (Fig. 2.2). It is known that optimising the processing parameters can influence their

microstructure significantly and, consequently, improve their properties [32]. Process optimisations is one of the main focuses of most researchers working on armour ceramics.

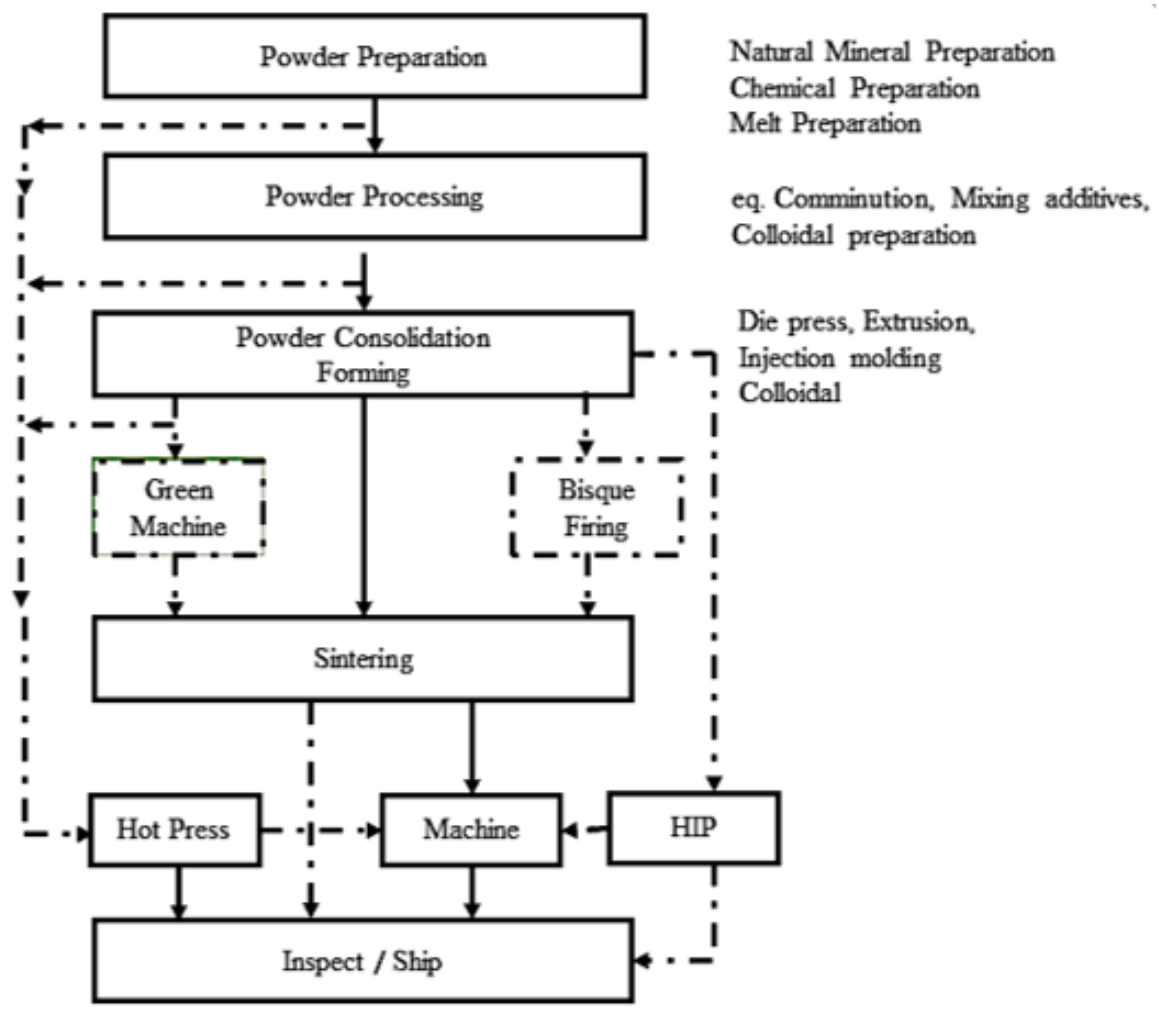

Figure 2.1: Schematic outline of sintering-based fabrication of ceramics [32]

The design of armour started with the use of leather and has evolved into the current armour plates. The trend in armour applications can also be found in the work of Reijer [1]. In the context of this study, armour is defined as a bullet resistance system used to prevent injuries to personnel from high-speed impacts from bullets. Armours are often used in the form of plates, most often designed to cover the chest, the back and some important parts of the body.

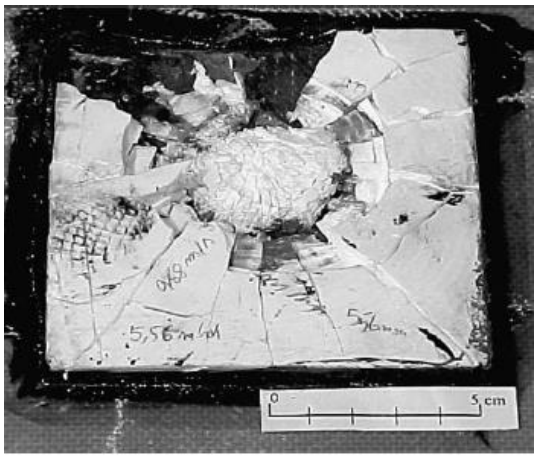

Figure 2.2: Fractured ceramic on impact showing a lateral crack propagation [21].

2.1.1 Emergence of Ceramics in Armour

The evolution of modern armour started with the use of hard steel inserted in polymer matrix or ballistic cloth, referred to as flak jackets or bulletproof vests. With the advent of better armour piercing projectiles (AP), steel was deemed too heavy as it needed to be used in large thickness to defeat AP bullets. The resultant excessive weight of steel made wearers uncomfortable and reduced their mobility. Hence, the development of more effective and lightweight armour systems became inevitable [9, 34].

The search for lightweight materials for armour applications emerged during the Vietnam War in the early sixties [34] and this search led to the use of ceramic in protective armour systems. Alumina (Al_2O_3) was the first ceramic to be used due to its low cost and ease of manufacture. Other ceramics which were developed and used alongside alumina included boron carbide (B_4C), silicon carbide (SiC), titanium diboride (TiB_2) and beryllium oxide (BeO). These materials were found to be equally effective [34], though much more expensive and difficult to manufacture compared to alumina. Table 2.1 presents some armour ceramics, including their properties and relative costs to alumina [9, 35].

Table 2.1: Some armour ceramics and their properties including their relative cost to alumina [9, 35].

Ceramics	**Density, g/cm^3**	**Vickers Hardness GPa**	**Knoop Hardness on 2kg Load kg/mm^3**	**Fracture Toughness K_{IC} MPa.m$^{0.5}$**	**Young's Modulus, GPa**	**Sonic Velocity, km/sec**	**Flexural Strength, MPa**	**Grain Size (µm)**	**Fracture Mode**	**Areal Density**	**Relative Cost**
Alumina, sintered	3.60-3.95	12-18	1291	3.0-4.5	300-450	9.5-11.6	200-400	N/A	N/A	20.2	1
Alumina-Zirconia, sintered	4.05-4.40	15-20	N/A	5.0-5.5	300-340	9.8-10.2	350-550	N/A	N/A	N/A	N/A
Silicon Carbide, sintered	3.10-3.20	22-23	1905	3.0-4.0	400-420	11.0-11.4	300-340	2.5	IG,TG	16.7	N/A
Silicon Carbide, hot-pressed	3.25-3.28	20	1924	3.8-4.5	440-550	11.2-12.0	500-730	3.5	TG	16.2	5
Silicon Nitride, hot-pressed	3.20-3.45	16-19	N/A	6.3-9.0	N/A	N/A	690-830	N/A	N/A	N/A	5
Boron Carbide, hot-pressed	2.45-2.52	29-35	2066	2.0-4.7	440-460	13.0-13.7	200-500	10-15	TG	13.0	10
Titanium Diboride, sintered	4.55	21-23	N/A	8.0	550	N/A	350	N/A	N/A	N/A	N/A
Titanium Diboride, hot-pressed	4.48-4.51	22-25	1849	6.7-6.95	550	11.0-11.3	270-700	N/A	N/A	23.4	10
Aluminum Nitride, hot-pressed	3.20-3.26	12	N/A	2.5	280-330	N/A	300-400	N/A	N/A	N/A	N/A

IG - Intergranular; TG – Transgranular, N/A: Not available

2.1.2 Design of Ceramic Armours

Stand-alone, ceramic cannot be used for armour applications due to its poor cracking resistance. As a result, the design of ceramic armour usually includes three or four components: the covering face or spoil foil, the ceramic plate, the adhesive, and the backing [4]. The hard ceramic front plate is designed to either shatter or blunt the tip of the bullet, and to reduce its penetrability [34]. The backing material, however, is tough and primarily designed to slow down the bullet and absorb its kinetic energy, thereby preventing its penetration [34]. Figure 2.3 shows examples of typical armour ceramic designs. It is well understood from the literature [3, 36] that the study of failure mechanisms of armour systems opened the door for diverse designs aimed at optimising their performance and creating lightweight armour. Two components designs include: (1) ceramic/metal or polymer [37]; (2) ceramic composite/metal or polymer [38]; (3) Ceramic/composite [39]; and (4) biomorphic systems of ceramic/ceramic [40]. In addition to the above there are laminated or hybrid armour systems [41] (Fig. 2.3b) such as ceramic-metal-composite armours [18], and other novel geometries and configuration [4].

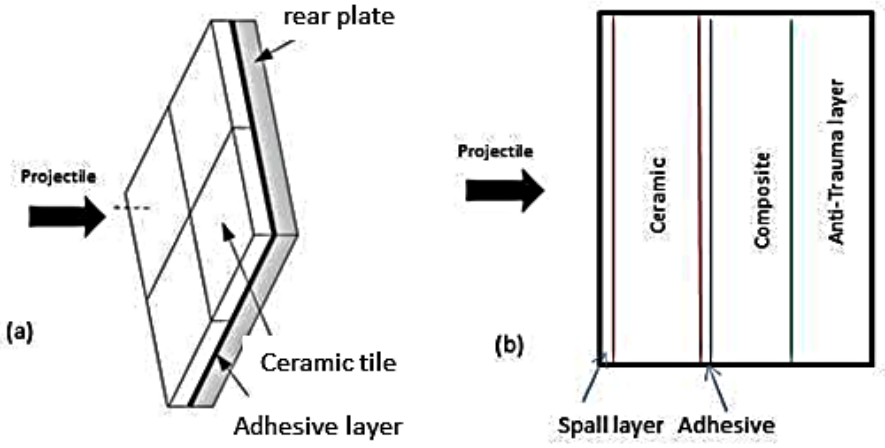

Figure 2.3: Examples of armour designs: (a) layout of a dual armour [42]; (b) hybrid ceramic armour.

It is recognized today that design of ceramic armour systems is based on the specific application, manufacturing ability, threat level, cost limitations [7] and the required material properties. Thus, the ballistic performance of ceramic armour is system-dependent; no single design is optimal for all threats.

2.2 Armour Related Properties of Ceramic

The study of impact failure mechanisms of ceramics has shown that their ballistic performance is dependent on both conventional and non-conventional properties [7, 43]. In addition to the lightweight and high hardness, other convectional properties include high compressive strength and high Young's modulus, as well as optimal microstructure and fracture toughness. The non-conventional properties include the fragmentation mode and fragments characteristics during ballistic impact, which are governed by the microstructure of the ceramic [19].

The key material properties that may be used to guide the selection of ceramics for light armours are: density, hardness, grain size, amount of minor phase, phase stability, fracture and toughness [7, 18], which are summarised in Table 2.2.

Table 2.2: Materials properties and their influence on ballistic performance [35].

Property	Effects on Ballistic Performance
Microstructure: Grain size, minor phases, porosity, inclusions, second phase and phase transformation	Density, hardness, elastic modulus, strength, fracture toughness, fracture mode (intergranular, transgranular or mixed)
Physical and mechanical properties:	
Density	Weight
Hardness	Shatter or blunt the projectile and absorb part of its energy
Elastic modulus	Stress wave propagation
Strength	Multi-hit resistance, field durability
Fracture toughness Fracture mode (inter or transgranular)	Energy absorption and crack propagation resistance

2.2.1 Physical and Mechanical Properties

To date, the armour performance has not been successfully correlated to a single mechanical property due to the dynamic nature of ballistic events [19]. Therefore, multiple quasi-static mechanical properties are often collectively used to assess the ceramic performance in armour systems [7].

2.2.1.1 Density

The density of ceramics is controlled primarily by the chemical composition and defects that occur in the form of pores and inclusions usually introduced during fabrication [32]. The theoretical density is often used for identifying ceramics for ballistic applications. For composite armour ceramics, it can be evaluated using the content and the theoretical density of each constituent. The density measurement through porosity assessment has found widespread application in Non-Destructive Evaluations (NDE) including the Ultrasonic Time-of-Flight (TOF) testing. Some of the merits of this method include: rapid application, good reliability, and ability to use thicker materials and, good sensitivity, which makes it possible to distinguish small density variations of up to 0.01g/cm^3 [44]. The density is then evaluated using semi-empirical equations such as equation 2.1 [44].

$$\boldsymbol{\rho = \rho_0(1 - P)} \tag{2.1}$$

Where the pore-free density is ρ_o; ρ is the density to be determined and P is the porosity.

The relative local density variation is often quantified as a percentage of the theoretical density. Density variations can lead to variabilities in ballistic performance in ceramics [46] that cannot be detected by conventional bulk density measurement techniques. It must be noted that density variations can originate from poor surface finish of ceramics, porosity, pore size, pore shape, and poor grain size distribution [44].

2.2.1.2 Hardness

Hardness is defined as the measure of a material's resistance to localised deformation, or indentation [45]. Table 2.3 shows hardness values of common armour projectiles and ceramics.

Table 2.3: Hardness values of some armour ceramics and threats [46].

	Prominent Armour Ceramics			**Projectile's core material**	
Material	SiC	99.9% Al_2O_3	B_4C	WC	RHA Steel
Vickers Hardness (HV)	1800-2800	1500-1900	2800-3400	1200-1550	700-920

The fracture and deformation characteristics of ceramics during hardness testing have long been the focus point of studies that aimed to understand the characterisation of both the hardness and the fracture toughness [46]. Ceramics generally exhibit high hardness, but also a high tendency for crack-formation [47]. In light of this, Vickers or Knoop indentions are often used for hardness measurement according to ASTM standards C1327-08 [48] and 1326-13 [49], respectively. Of these two methods, the Knoop indentation comes with a slightly higher recommendation [24] because it is less vulnerable to crack formation. In addition to the Vickers and Knoop indentation, some studies have also used the instrumented indentation method to measure hardness, which is based on the force-displacement behaviour during testing at low loads [50]. A good understanding of the mechanics of the elastic-plastic contact during indentation, as depicted in Figure 2.4 [51], is required in order to better assess the true hardness of ceramics.

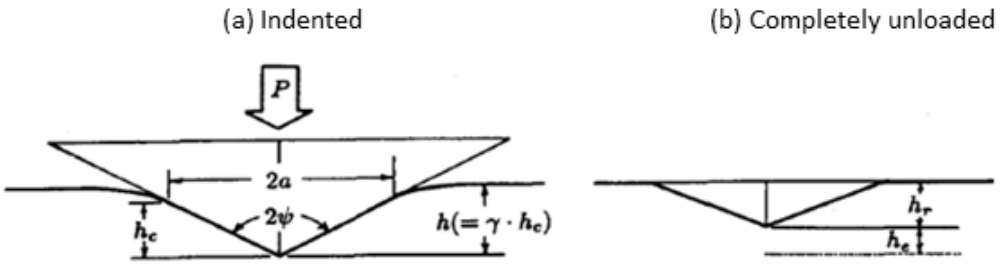

Figure 2.4: Geometry and coordinates of indentation contact [51]: he is the height of the elastic domain; hr is the plastic domain; hc is the actual depth of indentation; a is the impression of half diagonal of indent; ψ is the semi-apex angle of the indenter; and γ is a geometrical factor.

.

The elastic-plastic contact leads to a load dependency of the measured hardness (Fig. 2.5) [14] partly due to microstructural heterogeneities arising from grain size variability, second phase/inclusions and pores [45, 51].

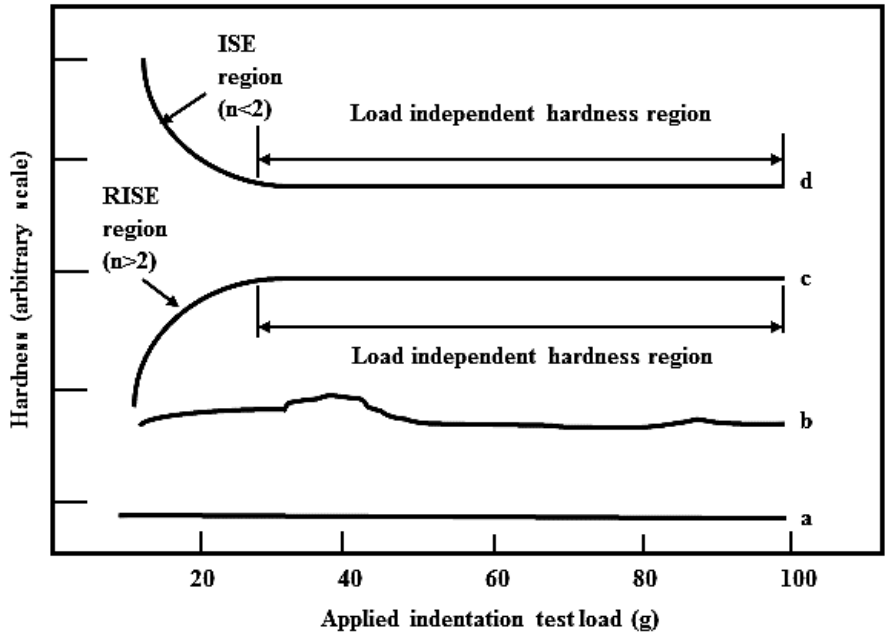

Figure 2.5: Hardness vs. load showing the different load dependencies of the measured hardness [14]: (a) constant hardness; (b) kink hardness; (c) reversed indentation size effect; (d) indentation size effect.

The load dependency requires further study of the load-hardness relationship in order to better understand the uncertainty that can be caused by microstructural features, measuring instruments and the operator [47]. Other challenges include: difficulties to correctly measure indentations due to potential crosshair indentation cracking, vibration and optical resolution limits [47]. Published literature provides guidelines for testing procedures [12, 52]. The load-dependency of the hardness ends at a transition point marking the beginning of a load-independency [14] (Fig. 2.5). This point has been suggested to represent the onset of fracture, to shed light on the relationship between hardness and brittleness, and consequently to be characteristic for the energy dissipation capability of ceramics [45].

2.2.1.3 Fracture Toughness

The objective of improving the fracture toughness is to increase the energy absorption capacity of armour ceramics during crack propagation, and to consequently improve the multi-hit capability. Higher fracture toughness confers onto the ceramic the ability to resist comminution and enhance the eroding capability on the projectile during the penetration stage [9].

It has been established that the fracture toughness depends on the composition and processing route of the material. The assessment of the fracture toughness has generated a lot of interest within the research community. Conventional methods including the single edge pre-cracked beam test (SEPB), the surface crack in flexure (SCF), and the chevron-notched beam test (CNB) contained in ASTM 1421-10 [53] are considered expensive and time-consuming. Researchers have therefore given considerable attention to the indentation method using the Vickers indenter, which is considered simple, low cost and fast [54]. A lot of controversies have followed the use of this method because of inconsistencies and high degree

of uncertainty in the results [15]. This uncertainty is attributed to the fact that the crack generated and used to evaluate the indentation fracture toughness is ill-defined and incomparable to the rapid crack propagation recorded in the standardised fracture toughness test [15]. Some studies did, however, indicate that there is still great potential in the use of this method [54-56].

Further tests have been suggested to corroborate the fracture toughness measurement using the indentation method. They include low velocity impact tests using Charpy and drop weight. These impact tests have demonstrated good results and applicability to provide a comparative qualitative measure of the energy absorption capability of armour ceramics [57].

2.2.1.4 Strength

The strength of ceramics determines the mechanism of and level of resistance to deformation and failure during the ballistic penetration stage [7, 43]. Although the exact strength threshold value for fracture resistance specific for either pressure, bend or shear is unknown, it is widely accepted that the strength is a property of significance in armour performance. In most cases, the fracture or flexural strength measured using a transverse beam test or a 3 or 4 point bending test, as contained in ASTM standard C1162-02 [58], is substituted for the tensile strength in brittle materials such as ceramics. On the other hand, in view of the edge effect, equi-biaxial methods, including the piston-on-three-ball, the ball-on-ring and the ring-on-ring tests, are used according to ASTM standard C1499-09 [59]. Although the ring-on-ring test has significant advantages over the other two methods [60], it is very sensitive to the size and relative dimensions of the specimen.

The flexural strength of a ceramic material is highly dependent on both its inherent resistance to fracture and the size and severity of flaws. Thus, according to the Griffith basic

principle of fracture mechanics, the largest flaw in the ceramic determines the level of fracture strength according to equation 2.2 [61]. From this equation, the flaw-causing crack can be calculated given the fracture strength and fracture toughness of the material.

$$\boldsymbol{\sigma_a = \frac{K_{IC}}{Y\sqrt{\pi a}}} \tag{2.2}$$

Where σ_a is the applied stress; K_{IC} is the fracture toughness; a is the half size of the largest flaw in the material; Y is the shape parameter of the flaw which is a function of crack shape and size.

2.2.1.5 Young's Modulus

The Young's modulus governs the speed of shock waves. When the Young's modulus of the ceramic armour is higher than that of the projectile, the speed of the shock wave is reduced leading to reduced fragmentation [18, 40], and increased ballistic performance The presence of volumetric flaws in the form of cracks, porosity and inclusions affects the Young's modulus. The Young's modulus is often measured using ultrasonic tests. The results of ultrasonic tests are affected by factors such as the thickness of the sample, the level of porosity [44, 62], the crystal structure, the bonding and the orientation of the material [63]. Other methods for evaluating the Young's modulus include: (1) using instrumented indentation hardness test data and the Oliver-Pharr method [64]; (2) the analysis of flexural strength test data; (3) the analysis of cracks formed at Knoop indents [14]; and (4) the porosity-controlled method using the pore volume fraction and semi-empirical models such as equation 2.3 [65, 66].

$$\mathbf{E = Eo\ (1 - 1.9P + 0.9P^2)} \tag{2.3}$$

Where E_o is the pore-free modulus of elasticity; E is the modulus of elasticity of the porous ceramic and P is the pore volume fraction.

2.2.2 Microstructure

The paradigm of microstructure, properties and processing illustrates the interdependency between these three subjects as shown in Figure 2.6. This translates into the ability to control physical and mechanical properties through microstructural design. The microstructure is known to control the performance of ceramics during ballistic events through alteration of crack propagation and energy dissipation mechanisms [9, 43]. A uniform microstructure is often the goal, although a low percentage of well-distributed porosity can still give high ballistic strength [23].

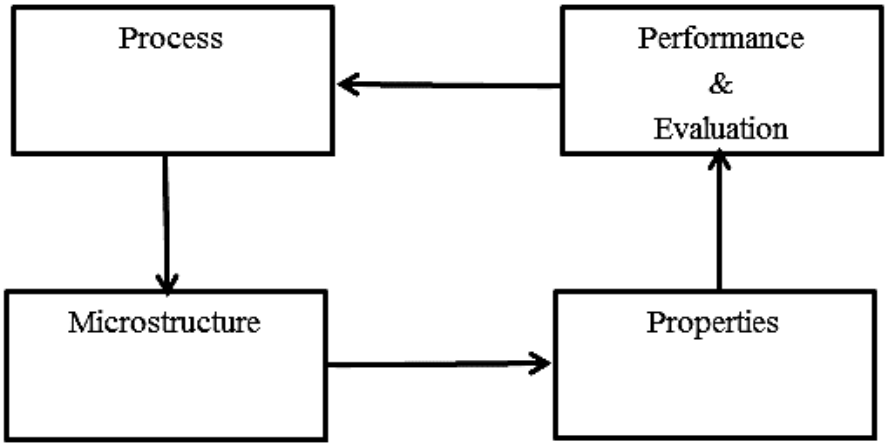

Figure 2.6: Paradigm of microstructure, properties and production process.

The major challenge in ceramic processing is to obtain a microstructure that provides the best combination of properties. Variables that control the microstructure of ceramics include: the starting raw material (particle size, shape and purity), compaction process, sinterability of the powder, final grain size, shrinkage, porosity and flaw population, additives and densification method [67-69]. It is very important that all the production stages including

powder production, compaction and sintering are carried out in an optimal fashion in order to achieve good microstructure [70].

2.2.2.1 Powder Preparation

The raw materials for a batch powder include the powder, additives, fluxing agents and a few others, all of which are aimed to produce a high green compact that will lead to a high density final sintered product [67]. It was demonstrated that a proper selection of starting materials with a good batch composition, initial particle size and particle size distribution makes it possible to optimise the microstructure and obtain the desired grain size and physical properties [67]. The overall goal of a good batch powder preparation is to achieve a high green density after compaction. This is achievable when the powder demonstrates good particle dispersion and flow behaviour during pressing, which will eventually serve to reduce the shear strength of the powder. Desired are granular precursors with good spherical shape, a high flow ability and a good arrangement that lead to effective compaction [71]. Also, the use of fluxing agents such as MgO, CaO, SiO_2 was known to influence the properties of sintered products. For instance, MgO is commonly used to help obtain finer grains and inhibit grain growth in alumina [71]. The volume fraction of fluxing agents should be limited in order to avoid excessive reaction with the ceramic powder in the sintered product.

2.2.2.2 Sintering

Defect populations such as microcracks, density gradient, pores and agglomerates in sintered ceramic mostly originate from either the forming stage or the compaction process. These defects are formed when the powder packing structure is evolving [72], hence the need for a proper compaction process designed to: minimise defects, achieve high relative density, good green strength and consequently best sintered product properties.

The aim of sintering is to create a homogeneous microstructure in the sintered product that will have less flaws, high relative density, well-controlled grain size and shape. Sintering can be controlled using sintering aids, the application or non-application of pressure and the sintering profile. Sintering aids are generally used to reduce the sintering temperature leading to a reduced grain growth and improved properties in the sintered product. For example, MgO, SiO_2, TiO_2, TiO_2-MnO_2, CaO-Al_2O_3 and glass are commonly used as liquid forming additives to improve the densification and mechanical properties of pristine alumina [73]. Furthermore, MgO and NiO are often used as sintering aids to inhibit grain growth, with MgO also acting as an impurity scavenger [73]. The importance of sintering aids to improve densification was demonstrated in many studies [70]. Sinter additives have also been found to drastically improve fracture toughness. For example, processing additives can improve the fracture toughness of monolithic SiC from 2.6 to 8.7 MPa.√m [74], though in doing so the hardness was found to be compromised.

The densification method is known to be influenced by pressure. For example, in the production of zirconia toughened alumina, hot pressing (HP) produces better microstructure and improved properties (less pores) than pressureless sintering (PS). Also, hot isostatic pressing [HIP] provides higher strength and controls the size of defects better than PS [75]. Moreover, HIP often provides uniform and isotropic properties that result in high fracture toughness, high strength and low residual stresses [75]. For SiC, using HP or HIP may create a better microstructure, but post heat treatment may be required when HP is used to obtain a desired grain size [74]. As undesired chemical reactions and grain growth can occur during sintering, lowest possible sinter temperature and shortest possible sinter durations are often preferred [76, 77]. As an example, using PS in SiC may lead to a decomposition reaction,

which is usually seen when oxide additives like Al_2O_3 and SiO_2 are used [69]. Furthermore, incomplete burn-off of additives during sintering may lead to carbonaceous residues, which may contaminate the microstructure, thus causing cracks or shape distortions in the final product [77].

In the case of alumina composites containing nanotubes as reinforcement, the sinter behaviour is different to that of pristine alumina. First, undispersed or agglomerated CNTs can contain large pores whose size can increase as the sintering temperature increases [78]. Moreover, reactions between alumina and the reinforcement should be minimised without compromising the material relative density. It must be noted that literature strongly recommends temperatures below 1150^oC for sintering alumina composites reinforced with CNT [76], since CNTs can be destroyed and converted into graphite above that temperature [76]. Spark-plasma sintering (SPS) or similar methods, in which the heating rate is as high as 600 ^oC/min, can help in avoiding nanotube destruction [79].

2.2.2.3 Sintered Microstructure

Just like porosity, the grain size of ceramics is considered a key parameter that can influence the mode of failure during ballistic impacts [21, 35]. While small grains favour intergranular and correspondingly higher fracture toughness, large grains lead to transgranular failure with low fracture toughness, as well as residual stresses that reduce strength [74]. The grain size is generally controlled by the initial particle size of the powder, sintering additives, sintering temperature and second phase inclusions. Presented in Figure 2.7 is the effect of grain size on K_{IC} and hardness of alumina. Note however, that large grain aspect ratios also favour increased K_{1C} [67]. The effect of grain size on the strength can be described by the

Hall-Petch equation 2.4 [72] postulating that fine-grains lead to increase in hardness and strength.

$$\mathbf{M = Mo + Kd^{-\frac{1}{2}}} \tag{2.4}$$

Where M represents either the strength or the hardness; M_o is the corresponding constant; K is the slope or the Hall-Petch constant; and d is the mean grain size.

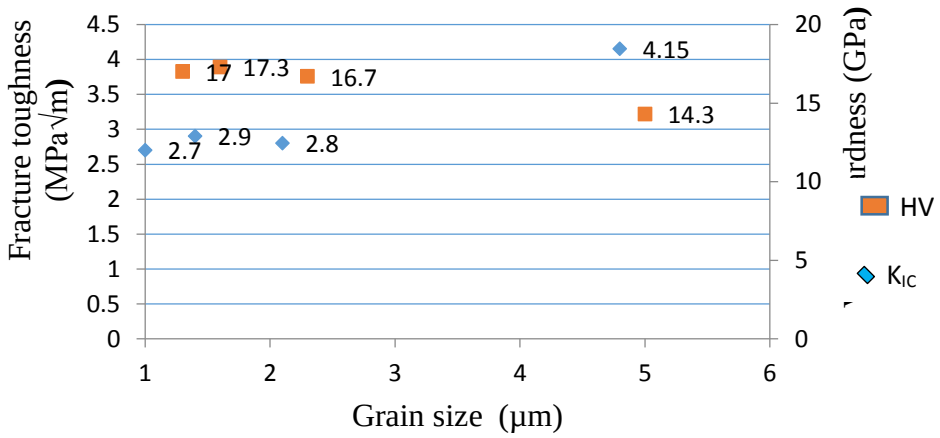

8 Figure 2.7: Hardness and fracture toughness dependency on the grain size for alumina [72].

One of the key methods to extend the applicability of ceramics is through toughening by second phase particles. Zirconia, for instance, is used as a second phase to increase the toughness and strength in zirconia toughened alumina (ZTA). ZTA possesses a fracture toughness of up to 12 MPa√m, which is much higher than 3 MPa√m for monolithic Al_2O_3 [80]. The work of Evans summarises the different toughening mechanisms in ceramic and their limitations [80]. An increase in fracture toughness is often accompanied by a change from transgranular to intergranular fracture, which favours energy dissipation. It has also been found that the mechanism of toughening used in monolithic ceramics can be: crack deflection, crack bridging, microcracking or frictional grain bridges. It must also be noted that the

influence of the fracture toughness on the ballistic performances of ceramics has long been a controversial issue due to the inability to correlate individual mechanical properties to the ballistic performance. Nonetheless, it is universally accepted that ceramic ballistic performance, particularly the multi-hit performance, requires improvement in many areas, including in fracture toughness. Because of this, both carbon nanotubes and boron nitride nanotubes have been identified as good reinforcements for monolithic ceramics [5, 8]. Additional information concerning the influence of nanotubes on ceramics properties is presented in section 2.4.

Porosity arises as a result of the incomplete interlocking of the powder grains of the ceramic starting materials. This usually occurs in alumina when pressureless sintering is used. In such situations, the porosity effect can be explained by the pore volume fraction, pore structure and grain bonding of the matrix. Porosity decreases the strength and the elastic modulus of ceramics. The effect of pores on the relative strength and Young's modulus of alumina is given in Figure 2.8 [66, 72]. More often than not, porosity also promotes failure and leads to conoid formation and fragmentation during impact [20]. The inhomogeneous distribution and size of pores also have a deleterious effect on other materials properties. For example, the hardness increases with a higher density and smaller pore size in Al_2O_3. It is also accepted that a non-uniform distribution and high concentration of porosity leads to a wide variation in hardness and scatter in strength [32]. This is the reason why ceramics have a low reliability, and the method of characterisation of their properties depends on the microstructure. For example, the hardness of ceramics with high porosity is best characterised using the Knoop Indenter [24]. Several works in the existing literature have strived to establish

the porosity-Young's modulus relationship using semi-empirical equations; one of the most common models is given in Equations 2.3 [44, 65].

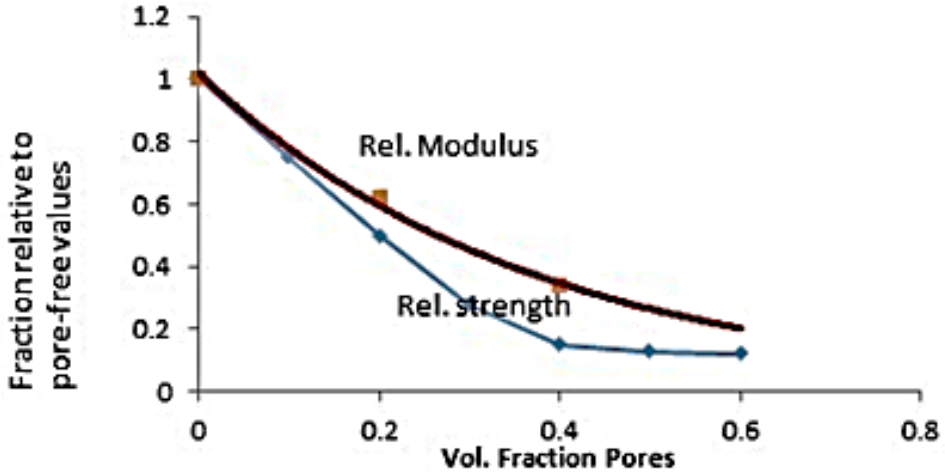

Figure 2.8: Effect of pores volume fraction on strength and Young's modulus of Alumina [65, 66].

Inclusions may be present in the form of unrecovered additives after processing, or as agglomerations of nanotubes when they are not well dispersed in the ceramic matrix [5, 22]. Inclusions may also come from the furnace or mould environment during fabrication. In general, inclusions are deleterious to ceramics and their properties. For example, a non-homogeneous distribution of additives not recovered during sintering may result in the creation of residual porosity [68]. Furthermore, gas adsorption during sintering at high temperature can lead to bloating or cracking of the material [72]. Inclusions act as flaws similar to porosity. However, Bakas and Demibra showed that a certain level of micro defects or smaller inclusions and pores homogeneously distributed could still result in good ballistic performance in both Al_2O_3 and SiC [22, 23].

2.2.3 Ballistic-Related Properties of Ceramic

2.2.3.1 Sonic Velocity

The sonic velocity is defined as the speed of sound waves through a medium and is an extrinsic property of ceramics that contributes to wave propagation during the penetration of projectiles [9]. It is proportional to the energy dissipation capacity of the ceramics and as such, a higher sonic velocity can lead to a higher ballistic performance [7, 27]. A sonic velocity of ceramic plates far higher than that of the projectile reduces penetrability. The sonic velocity is controlled by the porosity and the Young's modulus [45]. For examples, B_4C has a sonic velocity of 14,200 m/s because of its low density and its high modulus of elasticity. Al_2O_3 on the other hand, has a sonic velocity of 8,500 to 11,500 m/s depending on its purity. A much lower sonic velocity of 4,900 m/s is measured for steel, which is used in most bullets or projectiles [9]. The sonic velocity is measured using ultrasonic methods. Longitudinal (V_L) and shear or transverse (V_T) waves are generated and received by transducers. The ultrasonic velocity test can be carried out in different ways depending on the information to be obtained. The ultrasonic velocity is a function of the porosity level and microstructural characteristics such as grain size and phases [44].

2.2.3.2 Areal density

The areal density (A_D) is an exclusive property of armour systems primarily used to evaluate and rank them with respect to ballistic performance [16]. This ranking is defined as an expression of the weight carried when the area covered by the armour is known, or as the ballistic protection efficiency [16, 17].

Mathematically, the areal density (A_D) is defined in Equation 2.5 [46].

$$A_D = \frac{\rho A t}{A} = \rho t \tag{2.5}$$

Where ρ is the bulk density of the material; t is the thickness; and A is the covered area.

Figure 2.9 shows the range of areal densities required for different ballistic threat levels [81]. This Figure is constructed to give a comparison of ceramic and steel as armour materials, showing their relative performance. The ballistic performance or efficiency is also often used to evaluate armour ceramics and is expressed as a function of the areal density as [16]:

$$\eta = \frac{\rho_b \times R_D}{A_D} = \frac{\rho_b \times R_D}{\rho_t \times t_t} \tag{2.6}$$

Where η is the efficiency, ρ_b is the density of the backing material; R_D is the reduction in penetration depth in the backing material; ρ_t and t_t are the density and the thickness of ceramic, respectively; and A_D is the areal density as defined earlier.

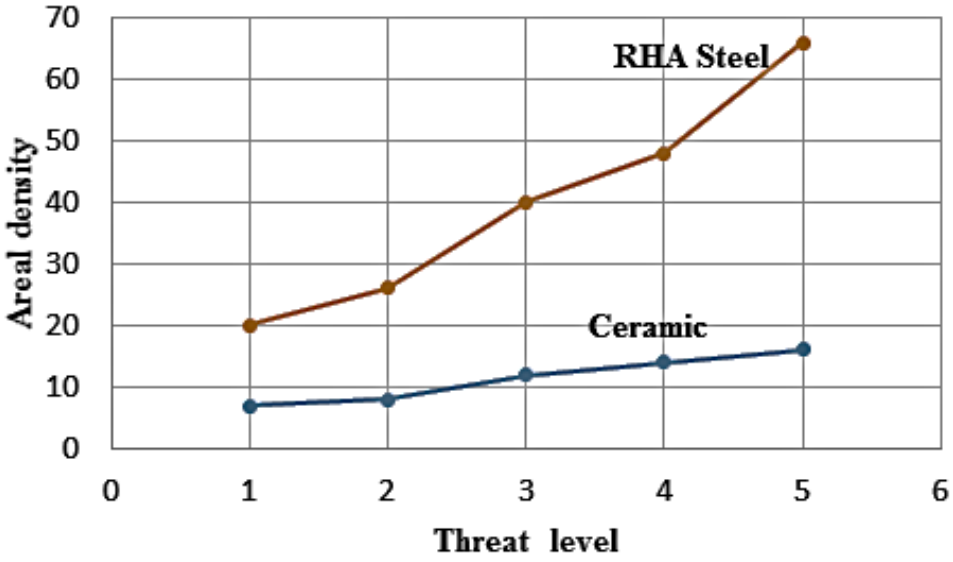

Figure 2.9: Areal density vs. threat level for ceramic and RHA steel armour materials [81].

2.2.3.3 Confinement

Confinement is a cover, a backing or a framing used to radially or laterally constrain an armour ceramic during impact events. Confinement is a direct method of increasing the compressive strength of ceramics during ballistic tests or events. The pressure applied may be in a bi-axial (radial confinement) or tri-axial (radial plus cover confinement) dimension [17]. This method has been shown to improve the ballistic performance of ceramics through the control of crack development and delayed fragmentation. The effect of this delayed crack development is that some failure modes are inhibited, the toughness is increased and the overall ballistic performance is increased. In particular, the reflected waves (called the tensile waves) that are the activators of fragmentation in the ceramics during ballistic events are greatly reduced [82].

2.2.3.4 Multi-Hit Capability

The capacity of armour ceramics to withstand a single shot has been the single evaluation criterion in previous decades. Armour ceramics do, however, generally lose their protective capacity with successive impacts. Therefore, multi-hit capability has become a major armour requirement in recent years.

The multi-hit requirement is usually specified in terms of distance given by the minimum number of projectile-calibre diameters allowed between impact locations without adversely affecting the protection provided by the armour design [46]. The multi-hit capability has also been found to be a function of ceramic toughness or crack resistance, which is found to significantly affect the fragmentation process [30]. The multi-hit performance is excellent in steel armours and was proven to be quite good in Functionally Graded Materials (FGM) based on ceramics with metal phases (also known as cermet). This was demonstrated using

ceramic-to-metal through-thickness gradients in so called Functionally Graded Armour (FGA) composites [46]. Another example of FGM is the Rolled Homogeneous Armour (RHA), in which cermet has shown great multi-hit capability. RHA has a large weight disadvantage, however, which prevents its widespread use in body armours.

2.2.3.5 Edge Effect

The Edge Effect is characterised by the inability of the induced stress wave generated by the high strain rate projectile to efficiently propagate across the ceramic boundary during ballistic events. In such cases, the ceramic cracks along its edges due to the reflected stress wave, as shown in Figure 2.10 [83], and is deemed not to perform optimally. Usually, impacts closer to the edge of the ceramic exacerbate this behaviour, particularly when the ceramic thickness is undersized [83]. One of the solutions to avoid this effect is to confine the ceramic along the edges.

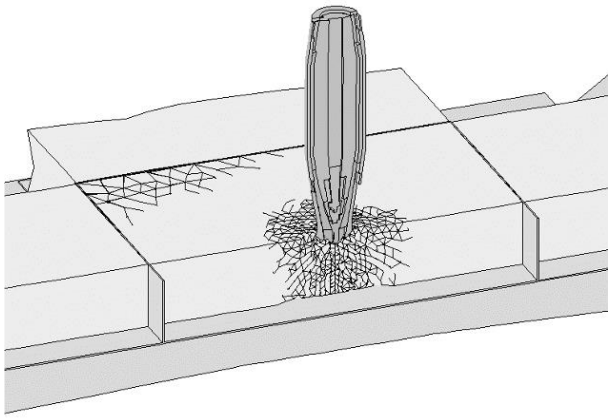

Figure 2.10: Edge cracking of a ceramic tile due to tensile stress wave reflections [83].

2.2.4 Ballistic Performance

The evaluation of the ballistic performance of armour ceramics is an integral part of armour design and is often expressed in term of depth of penetration, which is the distance the

projectile travels into the armour ceramic or the backing material before it is stopped. This evaluation has been a difficult task in the past due to the high number of variables involved in ballistic events [17]. These variables include the attributes of the projectile, the nature of the ceramic and the configuration of the test set-up. The evaluation is carried out using theoretical and experimental methods.

The theoretical method is sometimes referred to as the "predictive method" and has widely been applied in numerous fields of armour ceramic testing, including numerical and analytical techniques. While the numerical method has been widely used to assess ballistic performance [84], it fails to identify trends unless multiple configurations of ballistic test set-up are considered, which can cause the design process to be long and tedious [85]. The analytical technique, which is frequently used, is based on the development of expressions derived from equations inherent to continuum mechanics. Although it has the ability to analyse a very high number of parameters, as is often needed when considering ballistic events, its accuracy depends on the simplified hypotheses adopted or the appropriateness of the penetration mechanism used [86, 87]. The experimental method includes real life bullet testing or the use of representative projectiles, which can be made using hard steel or tungsten carbide rods. In most cases, the experimental tests provide depth of penetration data that can be used to validate and optimise theoretical models providing trends for armour improvements [88].

2.2.4.1 Depth of Penetration

The primary goal of armour design is to protect the target. Thus, the depth of penetration (DOP) test, which uses life bullets, accompanied with its simplicity to set-up and the speed at which the results are obtained, has become one of the best of numerous methods of evaluation. Moreover, it has the overall advantage of guaranteeing that the armour will be

efficient when used three-dimensionally [85]. As such, the DOP method has been widely used to characterise and evaluate armour ceramic performance because it provides a conceptual and practical tool that helps judge the impact of changes introduced to a system [87]. The DOP method also provides researchers with valuable information to help optimise armour ceramics as well as to rank them in comparative studies [17].

The DOP method can also provide information on phenomenological events, allowing researchers to correlate properties to armour ceramic performance [89]. Applicable standards include: the US National Institute of Justice (NIJ) Standard No 0101.06 of 2008 [90], the MIL-STD3768 of the United States Military [91] and the North Atlantic Treaty Organisation (NATO) STANAG 2920 standard for ballistic resistance to body armour [92].

The validity of DOP results depends on many variables such as: (1) backing material, (2) bonding between ceramic and backing material, (3) ceramic confinement, and (4) test setup [17, 28]. All these factors are considered in the set-up of the ballistic test and their shared overall goal is to improve the performance of armour ceramics. A good example of DOP test set-up is shown in Figure 2.11.

When it comes to backing materials, the factors involved in their selection include mechanical properties, thickness and confinement. The mechanical properties determine the acoustic impedance of the armour and the wave magnitude during the ballistic event. For example, steel has higher impedance and a higher ballistic performance than aluminum and has been therefore widely used as backing material in DOP testing [17, 93]. Thick backing plates can help eliminate edge effects and induce pressure [16]. They can also delay the occurrence of tensile stresses on the ceramic and, by doing so, make good ballistic evaluation possible [16, 17]. While the use of softer backings like composites may

change the results of the DOP test [18], tests using polycarbonate as backing have been found to give satisfactory results [81, 94]. Regarding the adhesive used for bonding of the ceramic to the backing material, its thickness and method of bonding have been found to influence ballistic performance [42].

DOP test results generally show large statistical variations of 40% on average, which is partially due to large variations in the mechanical and microstructural properties of the ceramic [18]. Therefore, obtaining reliable results requires that many tests be effectuated. Thus, the accuracy of DOP tests depends on whether or not multiple tests are done under identical conditions [17, 85].

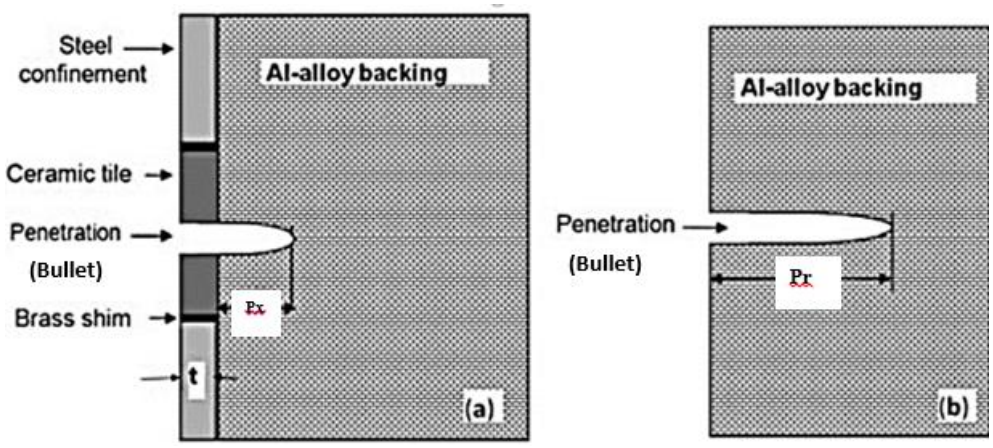

Figure 2.11: Schematic of DOP test configuration: (a) residual DOP (Px); and (b) reference DOP (Pr) in the backing material [30].

Most often, and in order to obtain accurate ballistic performance, a wide experimental program designed to cover a range of projectile velocities and ceramic thicknesses must be implemented. DOP test results for one configuration cannot be extrapolate to another armour system configuration. Predictive approaches are difficult as material type, geometrical and size of the ceramic and projectile can substantially change the results [85]. Therefore, only

hypotheses on optimal ballistic efficiency or performance criteria are often postulated in the literature to help interpret the results of the DOP tests.

2.2.4.2 DOP Correlation to Static Properties

As a result of complex stresses developing during ballistic impacts, it is challenging to correlate ceramics properties to ballistic performance [7, 43]. No single property can be reliably correlated to the ballistic performance and DOP tests only provide an end result of multiple interactions [17, 85]. Nevertheless, some mechanical properties, such as the dynamic compressive strength, have been used to rank the ballistic performance of ceramics [16]. The compressive strength is known to affect the erosive property of ceramics during the penetration process [34]. Another mechanical property found to be of great importance to ceramic ballistic performance is the hardness [1, 24]. The hardness influences the dwell time [95], reduces the projectile penetration potential, blunts and fractures the projectile core [1, 34]. The Young's modulus governs the speed of shock waves and sonic velocity and plays a major role in fracturing the projectile [34]. The correlation of ceramic fracture toughness to ballistic performance is still being studied. For now, it is understood from the study by Woodward that the kinetic energy of the projectile used to fracture the ceramic front plate is less than 0.2%, with the remaining energy absorbed during the penetration stage following ceramic fracture. Furthermore, it was shown that an increase in ceramic fracture toughness can result in less fragmentation, thus causing less penetration resistance [28]. Therefore, it could be concluded that an increase in ceramic fracture toughness may not improve the ballistic performance [19]. Other studies, however, have shown that improved toughness in ceramics led to improved ballistic performance [30, 31, 96].

On the other hand, the use of microstructure to quantitatively explain ballistic performance on ceramics is gaining ground [19, 20]. This trend becomes inevitable in view of the fact that using mechanical properties alone has been found inconclusive. Moreover, non-conventional properties can be related to ceramic fragmentation, which is known to be governed by microstructural variables including pores, inclusions, grain size and microcracks [19, 21, 43]. These variables are believed to influence the geometry and size of the fragments [34, 82]. Thus, improving the microstructure is key for armour ceramics and increased ballistic performance with less variability [17, 19, 22, 85].

The field of empirical equations to predict armour performance has not received much attention, unlike their analytical and numerical counterparts. Useful correlations between basic armour ceramic properties and their ballistic performance are, however, currently being considered [88, 97]. Empirical equations are often algebraic equations developed in order to extrapolate experimental results. Also, the huge amount of data generated from the numerical analysis can be used to formulate empirical equations and to establish the influence of individual parameters [88]. One of the most used empirical equations is the energy dissipation criterion according to Equation 2.7 developed by Nesphor [27]. It suggests that higher fracture toughness is unfavourable to ballistic performance. This is in sharp contrast to the general trend to improve the fracture toughness of armour ceramics in the drive to improve their ballistic performance and multi-hit capability [7].

$$\boldsymbol{D = \frac{0.36\, Hv.E.c}{K_{IC}}} \tag{2.7}$$

Where Hv is the Vickers hardness, E is the Young's modulus, c is the sonic velocity, K_{IC} is the fracture toughness and D is the energy dissipation criterion.

2.2.4.3 DOP Performance Index

The analysis of ballistic performance through the DOP test results has long focussed on using performance criteria to produce a single value [17, 85]. The difficulty of using a performance index is that ranking criteria are system-dependent [85, 98]. There are three main fundamental performance criteria reported in the literature, namely: the Differential Efficiency Factor (DEF), the Mass Efficiency Factor (MEF), and the Critical Thickness (CT) [16, 17, 46].

The DEF introduced by Rosenberg has been adopted and used in many studies [17]. It represents the differential of measured DOP on the backing material alone with that measured when a front plate is used. DEF is always given as a function of the ceramic areal density, and is very sensitive to ceramic thickness. Similar to the DEF is the Mass efficiency factor (MEF), which denotes the mass effectiveness of the ceramic to the backing material [17]. This index additionally incorporates confinement parameters. The critical thickness index presents the thickness required for the ceramic alone to stop the projectile. Further performance criteria currently used include: the Thickness Efficiency (TE), the Space Efficiency (SE), the Total Efficiency Factor (TEF), the DEF scaling from 0 to 1, the Weight Saving (WS), and the Stopping Efficiency Factor (SEF). The performance criteria are summarised in Table 2.4. Most of these indexes were developed using test set-ups with thick metal backing and confinement [16, 17] that have been found to yield improved ballistic performance [34, 99]. Soft backing test set-ups can produce different results [18].

Table 2.4: Ballistic efficiency indices used to evaluate the performance of ceramics in armours.

Ballistic Performance Criteria	**Equation**	**Literature**
Differential Efficiency Factor (DEF)	$\rho_b \frac{(Px-Pr)}{\rho_{t*}t_t}$	Rosenberg [16]
Thickness Efficiency (TE) or Space Efficiency (SE)	$\frac{p_x-p_r}{t_t}$	Madhu [17]
Mass Efficiency Factor (MEF) or Stopping Efficiency Factor (SEF)	$\frac{TE*\rho_b}{\rho_t}$	Madhu [17]
Weight Saving (WS)	[1 - $\frac{\rho_b*t_t+\rho_b}{\rho_{b*}Px}$]x 100	Hazell [94]
DEF Scaling from 0 to 1	1 - $\frac{\rho_b*Pr+\rho_t*t_t}{\rho_b*Px}$	Bless & Rosenberg [100]
Ballistic Efficiency (q^2) Product of MEF and TE	TE * MEF	Madhu [17]
Total Efficiency Factor (TEF)	$\frac{\rho_b*Px}{\rho_t*t_{t+}\rho_{b*}Pr}$	Meyer [101]
Critical Thickness	$\frac{t_t*Px}{(Px-Pr)}$	Hazell [46]
Ceramic Efficiency	1 - $\frac{Pr}{Px}$ *100	Yadav [102]

Where ρ_b and ρ_t are densities of backing material and ceramic, respectively; Pr and Px are penetrations with ceramic and without ceramic in place; and t_t is the thickness of the ceramic.

2.3 Failure Mechanisms

Armour ceramics operate under high strains and high strain rates when confronted with projectiles, leading to the development of complex stresses that control the material failure [34]. The complex stresses lead to crack nucleation, growth and coalescence [34, 82]. Therefore, the principal failure mode of armour ceramics is cracking and fragmentation. The level of cracking and fragmentation is determined by the threat level and its parameters, as well as the properties of the ceramic [34]. Other factors include geometry, confinement, interfacial condition of the ceramic [103] and backing material. It has therefore been

established through various studies that the understanding of failure mechanisms is critical for the design of armour ceramics for ballistic applications [3].

2.3.1 Cracking and Fragmentation

High-speed projectile impact generates compressive shock waves that travel through the thickness of the ceramic armour. Cracking is determined by the intrinsic properties of the ceramic, the impact velocity and the shape of the projectile. Cracking is also assisted by the rarefaction (reduced pressure) or tensile waves [9], which travel back from the ceramic/backing interface. The propagation velocity of the rarefaction wave is given in equation 2.8 [46]. It dependents on the acoustic impedance and the sonic velocities and is a function of the Young's modulus and the density. Also, the crack propagation, or crack velocity, is controlled by intrinsic properties of the ceramic [9, 34]. This is demonstrated in Figure 2.12a, where 2 wing-cracks emanate from the tips of a pre-existing flaw subjected to diverse stresses [104]. In addition, micro-defects are created during impact as illustrated in Figure 2.12b [105].

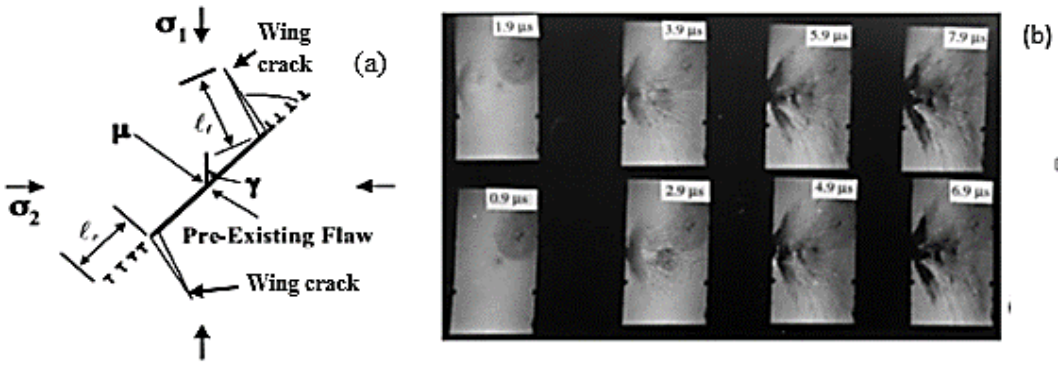

Figure 2.12: Influence of defects on ceramics under loading: (a) A schematic illustration of 2 wing-cracks emanating from the tips of a pre-existing flaw subjected to far-field stresses σ1 and σ2 [104]; (b) Cracking in SiC ceramic with time after impact

$$\mathbf{Co} = \sqrt{(\frac{\boldsymbol{E}}{\boldsymbol{\rho}})} \tag{2.8}$$

Where E is the Young's modulus; ρ is the density; and C_o is the propagation velocity of the rarefaction wave.

Fragmentation starts with the coalescence of micro-cracks, which is controlled by the density of defects [34]. Defect geometry, size and direction of the projectile are also contributing factors to fragmentation and its acceleration [106]. The fracture front ahead of the projectile propagates through the thickness of the ceramic, leading to the formation of a conical crack referred to as conoid [34, 36]. The formation of the conoid leads to the expansion of the ceramic by about 2-5% [34]. This contributes to impact energy absorption through the spreading of the impact load over a large surface area of the ceramic. Fragmentation leads to the loss of multi-hit capability [46].

2.4 Properties Improvement

The optimisation of strength and fracture toughness is crucial for improving the performance and multi-hit capability of armour ceramics. The goal of increased fracture toughness and strength is to delay crack propagation while enabling the armour to better dissipate the energy of the projectile [4, 107]. To achieve this goal, the armour design has undergone several evolutions/iterations. However, improving the fracture toughness and the multi-hit capability of armour ceramics without compromising other armour properties is a difficult undertaking, and has yet to be achieved. Nevertheless, it is broadly accepted by today's standards that such approaches should not only focus on flaw control, but also on toughening methods [80]. In line with the above, most researchers on armour ceramics are in agreement that current efforts should primarily focus on toughening methods through the use

of reinforcement or second phase inclusions [8, 108]. In fact, with the advent of nanotubes such as carbon nanotubes [CNT] and boron nitride nanotubes [BNNT], the field of ceramic reinforcement is currently regaining great interest [8, 108].

Well-dispersed CNT and BNNT nanotubes have proven potentially efficient in improving the fracture toughness and the strength of ceramics [108, 109]. They can also aid in the densification process by reducing the sintering temperature during the fabrication of the composite. Moreover, nanotubes can retard grain growth during fabrication and constitute as a grain refiner [110]. Finally, the nanotubes can retard crack propagation, thereby increasing the fracture toughness, the energy absorption capability and the multi-hit performance of ceramics against ballistic impact. The increase in energy absorption capability is achieved by crack bridging, crack deflection, pull-out and sword-in-sheath [110].

2.4.1 Carbon Nanotube

A comparison of CNT properties to other notable fibres is shown on Table 2.5. The superior properties and the low density of CNT demonstrate its great potential as a reinforcing phase. CNT can be obtained in many forms, including single-walled CNTs [SWCNT] composed of a roll of one graphene layer, often capped at each end, and multi-walled carbon nanotubes (MWCNT) composed of a concentration of multiple graphene. The production route of CNTs determines their yield, purity and state [108]. Although SWCNTs are of higher purity, they are more expensive to produce and break easier during processing [108]. Therefore, most studies have focused on MWCNTs for composite production.

As encouraging as the properties of CNTs as reinforcements are, three primary challenges confronting the production of the CNT-ceramic composites have been identified. These include: good dispersion of the CNTs in the ceramic matrix; maintaining the integrity

of CNTs during processing, especially during sintering at high temperature and prolonged time; and developing good interfacial bond between the CNTs and the ceramic matrix [109].

Poor dispersion usually leads to nanotube agglomeration into ropes or bundles. This is due to their relatively high surface area, high aspect ratio and typically poor interaction with solvents or matrix components [108].

Table 2.5: Properties of CNT and different engineering fibres [108].

Fibres	Density (g/cm^3)	Diameter (μm)	Young's modulus (GPa)	Tensile strength (GPa)
CNT	1.3-2.1	0.01-0.04	1300	20-63
SiC fibre	3	15-150	400	2.4
Boron fibre	2.6	2.3- 2.5	400	4
HM Carbon fibre	1.95	1.7-8	380	2 – 7
HS Carbon fibre	1.75	1.7-8	230	3.4
Glass fibre	2.56	11	76	2
Aramid fibre	1.4	12	70-180	3.6
Alumina fibre	3.9	3-20	300	2
Cellulose fibre	1	1-5	80	2

Where HM is high modulus and HS is high strength.

Toughening is enhanced only when individual CNTs are distributed uniformly throughout the ceramic matrix and are well separated from each other to avoid agglomeration. An example of good and uniform CNT dispersed in alumina is shown in Figure 2.13 [79]. Good dispersion ensures that each CNT is loaded individually, as shown in Figure 2.13b, of a fractured surface of a CNT-alumina composite [79]. This distributes the load over a maximum interfacial area, and therefore contributes directly to improving mechanical properties and adding to toughening [79]. In contrast, agglomerates act as defect sites leading to stress concentrations and premature failure [79, 108]. Furthermore, reported values of fracture

toughness are often questionable since, most often, the measurements are carried out using the direct crack measurement technique. This method has been heavily debated in the literature as to its validity. Studies have suggested that measuring the fracture toughness using indentation crack size may be misleading, as the crack may be affected by porosity [79]. In most cases, direct crack measurement methods tend to overestimate the fracture toughness.

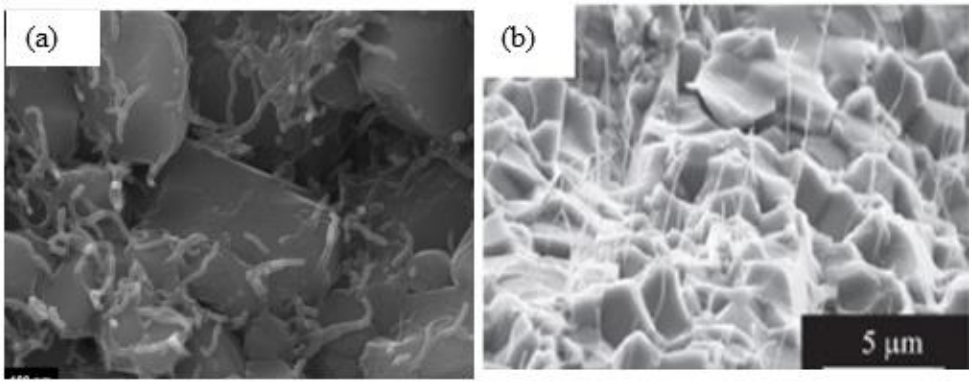

Figure 2.13: SEM images of (a) well distributed CNTs in Alumina matrix [79]; and (b) fractured surface showing how CNTs can be effective in toughening composites [110].

2.4.2 Boron Nitride Nanotube

Boron Nitride Nanotubes (BNNTs) are recently being considered as reinforcement in view of their structural and mechanical properties, and for their relatively better processability compared to CNTs. BNNTs have higher resistance to oxidation at higher temperature, are chemically more stable and have lower density than CNTs. Figure 2.14 illustrates some features of BNNT reinforcement in alumina matrix. However, the few publications available on BNNTs report challenges similar to those known for CNT reinforced composites. Nevertheless, addressing these challenges in BNNTs is considered to be more promising for better results [8]. Firstly, BNNTs stability at higher temperature will allow pressing by hot compaction, which will lead to better densification [8]. Secondly, due to the chemical stability of BNNTs, a homogeneous dispersion may be easier to achieve than with CNTs. It has been

established that the size of BNNTs influences their properties [111]. Usually, BNNTs production size ranges from 1 to 200 nm in diameter, with the length greater than 10 μm [111]. The surface properties of the reinforcement become increasingly dominant as the surface-to-volume ratio increases with decreasing particle size.

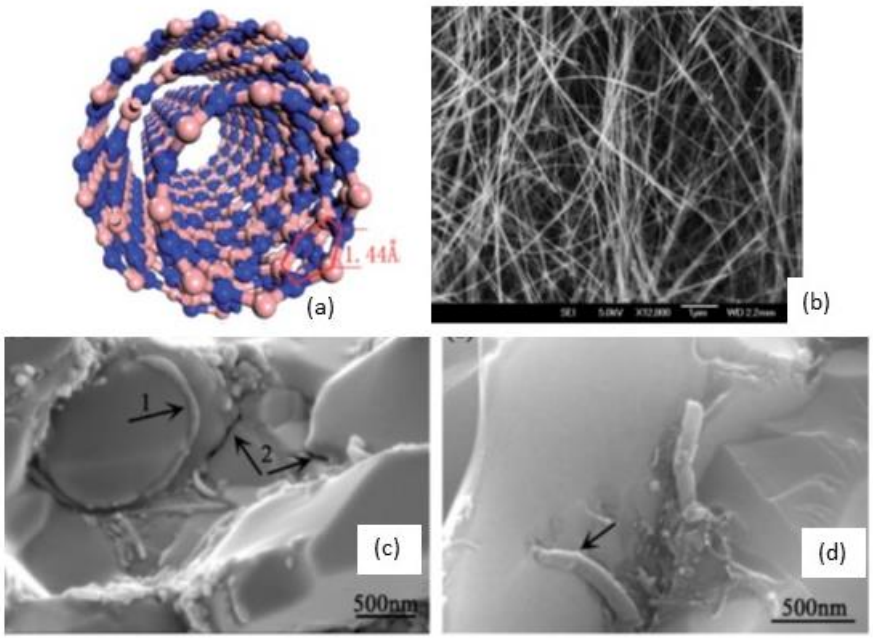

Figure 2.14: (a) Structural model of a multi-walled BNNT. The B–N bond length is 1.44 A [111]; (b) SEM image of highly pure BNNT synthesized by the BOCVD method [111]; (c) BNNT encompassing a Al_2O_3 grain; (d) BNNT located at grain boundaries [112]

Similar to CNTs, the volume fraction of BNNTs determines property improvements for alumina [112]. The highest fracture toughness value of 6.4 MPa√m was reported at 1.5% volume fraction of BNNTs, while the highest bend strength of 532 MPa was achieved at 2% volume fraction. Also, Vickers hardness values of 14.5 GPa and 19.4 GPa were reported at 2.5 % and 0.5% content, respectively [112]. Therefore, it can be concluded that no specific BNNT volume fraction provides best values for all properties desired for armour ceramic application. Rather, trade-offs for the desired properties are required for balancing properties

such as hardness, fracture toughness and strength. With only a few published literature sources, it is obvious that further studies are required in order to establish the most promising BNNT strengthening and toughening criteria for armour applications.

2.4.3 Characteristics of Nanotubes

High quality nanotubes are a pre-requisite for a considerable improvement of composite properties [111, 113]. The quality of nanotubes is determined by their morphology, level of defects and purities. The morphology includes the length, the diameters (internal and external), and the number of walls and the crystallinity of the nanotubes [114]. Impurities in nanotubes are inherent to the raw material (precursor), the synthesis method, the temperature and time of synthesis, the catalyst used for the synthesis and the ratio of the catalyst to the raw material [115]. Defects are known to lead to a structural deformation of the nanotubes, resulting in waved, coiled, regularly bent, branched and beaded shapes. Defects also change the tube diameter and alignment and distort the tube curvature [116, 117]. Moreover, impurities in the nanotubes act as failure initiation points during loading of the composites [79]. The need to study the level of defects and the degree of purities in nanotubes originates from their impact on the nanotubes properties, including diameter, chirality (the way the tubes are formed) and length, which are central to the toughening capability of the nanotubes in ceramic composites [118]. With respect to the morphology, aggregation and bundling can prevent good dispersion of the nanotubes in the ceramic matrix leading to poor properties in the composites [79, 108].

CNTs have been shown to start to gain weight between 400 and 500^{o}C, and BNNT to lose weight between 700 and 900^{o}C [111, 119, 120]. The weight gain or weight loss temperature is called oxidation temperature, and will increase with the purity and crystallinity

of the tube. The weight change is primarily caused by the oxidation of residues of the catalyst used for nanotube production for CNT and by the oxidation of metal nano-particles for BNNT [111]. The interactions of CNT and BNNT nanotubes with water are also well documented in the literature. While CNT is known to be highly hydrophobic, BNNT results have been either hydrophobic or hydrophilic depending on the method of measurement [121].

2.4.4 Dispersion of Nanotubes

Several approaches can be used to disperse nanotubes in ceramic matrices, such as the in-situ method involving ultra-sonication followed by ball milling. This method has, however, been reported to potentially lead to segregation during drying and to create a carbon film at grain boundaries [109]. Colloidal processing on the other side usually leads to shortening of single walled carbon nanotubes (SWCNT) and the use of solvents may compromise the purity. While solvents such as sol-gel can break up CNT agglomerates, they often fail to disperse the nanotubes [109]. The direct growth of nanotubes on ceramics, also referred to as CVD, does not usually create high quality coverage [118]. Furthermore, some studies have recommended the combination of colloidal processing and ball-milling [122]. Overall, ball-milling offers a great potential for good distribution of CNT in ceramics by (1) allowing the opening of the tip regime which improves the distribution of CNTs [122], (2) allowing CNT disentanglement without affecting the nanotube outer diameter and shortening of the aspect ratio [123], (3) increasing the specific surface area, thereby reducing agglomeration and particle size [122], and (4) helping to remove amorphous carbon and carbon particle impurities [122]. A negative aspect of ball-milling is that it is also known for its high energy input, which may destroy the nanotubes. This requires increased caution for appropriate milling parameters, including time of milling, type of mill, temperature of milling, milling speed, size of balls and medium of

milling [124]. Wet milling using ethanol as a milling agent was reported to produce a better dispersion of nanotubes in ceramics [8, 125]. Potential adverse effects on the purity were not investigated in the aforementioned study.

2.4.5 Toughening Mechanisms in Nanotubes Reinforced Alumina

Energy can be absorbed in nanotube-toughened ceramics by shear banding or pore collapsing, similar to mechanisms in ductile metals leading to multiaxial damage tolerance [126, 127]. Pore collapsing toughening has been found to lead to high toughness values. Toughening mechanisms produced using nanotubes as reinforcement in ceramics are strongly dependent upon the interaction between the ceramic matrix and the reinforcing phase, as well as their connectivity or interfacial bonds. This connectivity is known to control stress transfer during loading. Good interaction and connectivity depend on unifom dispersion of the NTs, as illustrated in Figure 2.15 [108].

The four major toughening mechanisms in both CNT- and BNNT- modified alumina composites are: crack bridging, crack deflection, pull-out, and sword-in-sheath [110]. Crack bridging is found perpendicular to the crack path, as shown in Figure 2.16a, whereby NTs remain intact in order to bridge the crack [112, 128]. Crack deflection is illustrated in Figure 2.16b, and it leads to a tortuous crack path, similar to the intergranular failure mode, usually accompanied by high energy dissipation at grain boundaries [129]. Two of the factors that favour crack deflection are large deflection angles brought about by the elongated grain sizes of the matrix and a ceramic matrix with small grains [128].

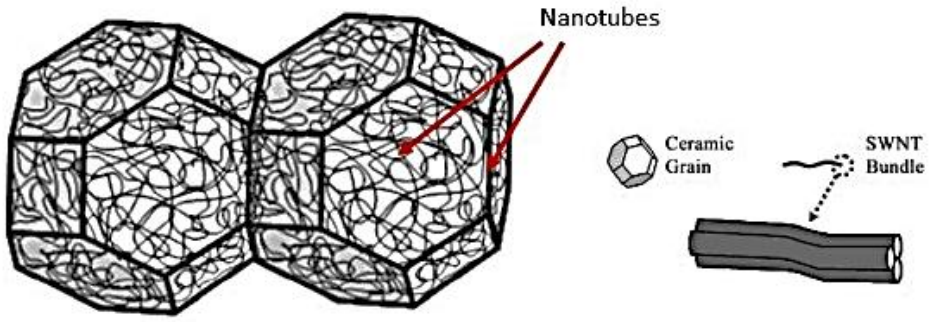

Figure 2.15: Alumina grain showing the distribution of nanotubes on its matrix and grain boundaries [108].

.

Nanotube pull-out (Fig 2.17c) involves the debonding of NTs at the crack surface, which is usually preluded with crack bridging, and thus requires a weak fibre/matrix interface [128]. During pull-out, nanotubes exert a closing force on propagating matrix cracks to constrain their growth. This means that greater work energy will be required to pull the nanotubes against residual sliding friction at the fibre/matrix interface and, in doing so, will improve fracture toughness significantly [128].

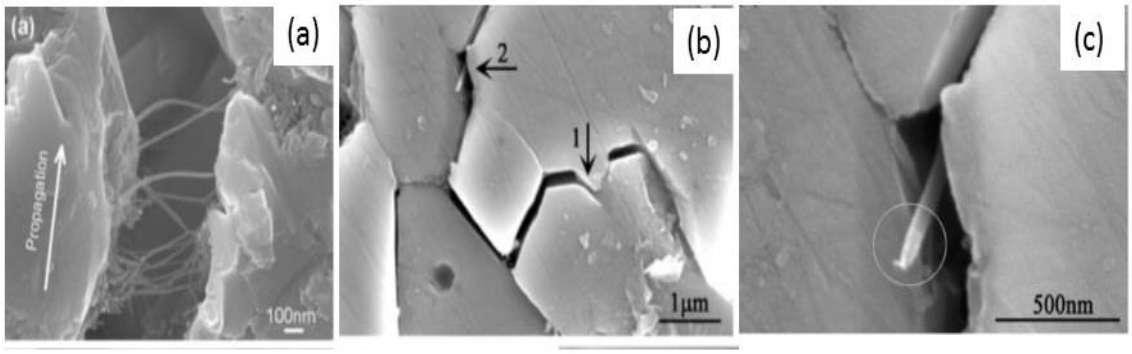

Figure 2.16: (a) Crack bridging in CNT-alumina [128]; (b) crack deflection in BNNT-alumina [112]; and (c) pull-out in BNNT-alumina [112].

The pull-out force is controlled by the original length of the nanotube (NT). Short nanotubes might pull-out from the matrix without contributing much to the toughening of the composite. The pull-out mechanism indicates whether or not NTs are being significantly

stressed as they share the load applied on the composite [128]. The relationship between the interfacial strength and the pull-out length can be described as in equation 2.9.

$$\boldsymbol{\tau = \frac{\sigma_u d}{4l}} \tag{2.9}$$

Where τ is the shear strength, σ_u is the tensile strength, and d and l are the radius and length of the CNT, respectively.

The sword-in-sheath mechanism occurs when there is preferential failure between the CNT inner and outer shells. The inner cores are pulled away, leaving only the fragments of the outer shells behind in the matrix, which can generate a strong load transfer [128] (Fig 2.17a). Other nanotube loading and deformation mechanisms include stretching, disentangling and collapsing, as shown in Figures 2.17 b and c.

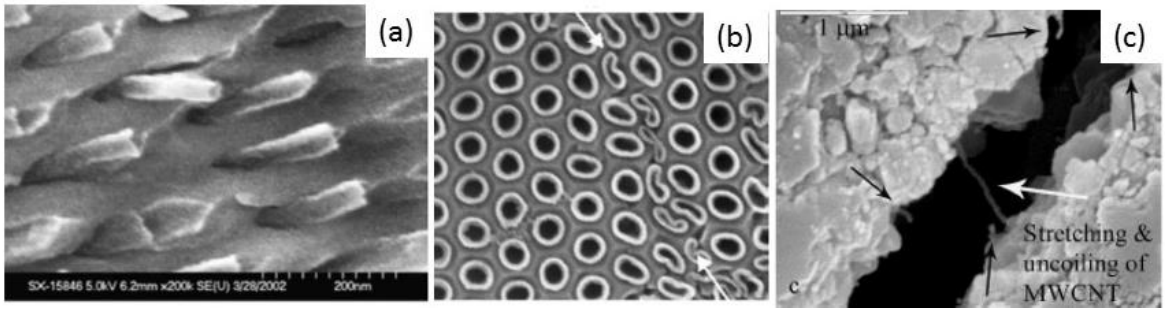

Figure 2.17: (a) Sword-in-sheath mechanism [128]; (b) CNT collapsing; (c) Stretching/disentangling [130].

CHAPTER 3

MATERIALS AND METHODS

3.1 Materials

The first set of investigated materials include commercially produced (100 x 100 x 7 mm) Zirconia Toughened Alumina (ZTA) tiles obtained from NP Aerospace Inc., a world leader in advanced high performance and composite armours, while silicon carbide tiles of the same dimensions were sourced from Morgan AM&T. Both ceramics were manufactured through the pressureless sintering route, the pictures are shown in Figure 3.1. However, the process parameters as well as the production details are proprietary in nature and were therefore not released.

The two ceramics are designed for use in lightweight armours for personal body protection systems, with the goal to defeat 7.62 mm armour projectiles with muzzle velocity and kinetic energy of about 820 m/s and 3463 J, respectively. The projectile parameters are in accordance with the NIJ standard for level IV threat [90].

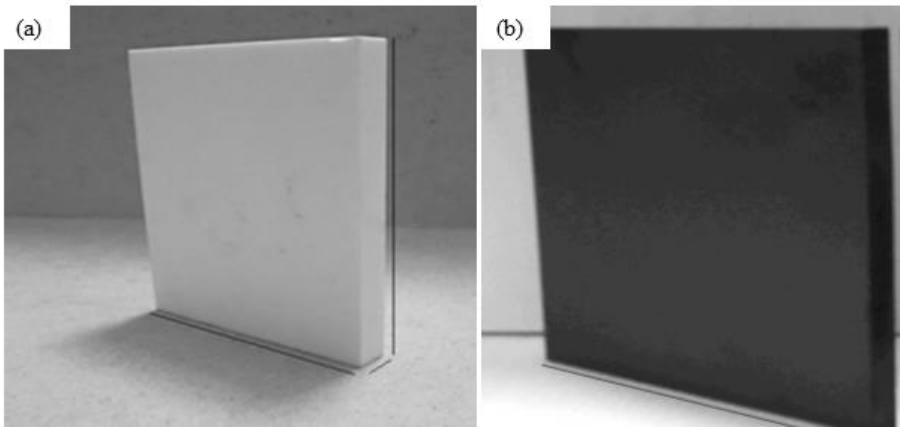

Figure 3.1: Commercial ceramic tiles: (a) ZTA; (b) SiC.

The second set of materials are nanotubes including carbon (CNT) and boron nitride (BNNT) nanotubes and granular alumina. Both nanotubes were multi-walled and were supplied by the National Research Council (NRC), Ottawa, Canada. BNNT nanotubes were produced at the NRC complex and CNT nanotubes were purchased from Nanocyl and NC 700 in Belgium. Figures 3.2a and b show pictures of the two nanotubes while Figure 3.2c shows an image of the alumina granules. The alumina powder, which has a purity of 99.7%, was produced by the Accumets Incorporation. Other process parameters and properties of the alumina powder (according to the manufacturer) include a density of 3.89-3.92 g/cm^3 and average granular sizes of 160-200 µm. The particle size of the alumina, however, was revealed to be about 500 nm when the granules were hand-pressed.

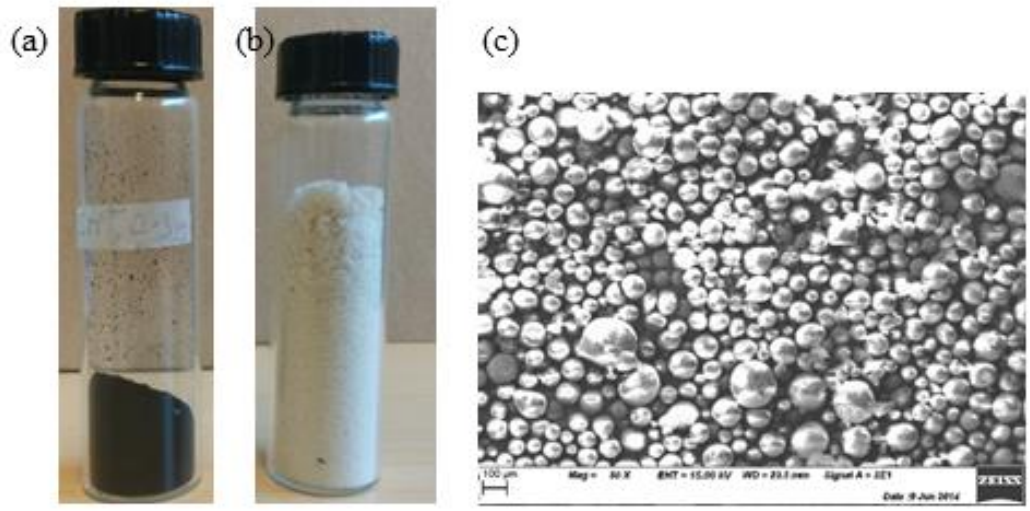

Figure 3.2: Materials of the study: (a) carbon nanotubes; (b) boron nitride nanotubes; (c) as-received alumina image showing its granular form.

The third set of materials are six armour ceramics tested for the depth of penetration. They were fabricated by National Resource Canada (NRCan), Hamilton, for DRDC, Valcartier. These include three monolithic ceramics Al_2O_3, SiC and B_4C as reference materials, and three reinforced armour ceramics Al_2O_3-BNNT, Al_2O_3-SWCNT and SiC-

BNNT. The tiles were rounded at the four corners (Fig. 3.3) to provide for anti-edge effect during the test.

Figure 3.3: Picture of a set of the ceramic tiles showing chamfer edges.

The ceramics were fabricated through hot-pressing into 100 x 100 square tiles of 5.80 ± 0.05 mm thickness. Other fabrication parameters were proprietary and are not given here. Additionally, the hardness, density, and fracture toughness values of the ceramics were supplied (see Table 3.1).

Table 3.1: Some mechanical properties given on the armour ceramics.

Armour ceramics	**Al_2O_3**	**Al_2O_3-BNNT**	**Al_2O_3-SWCNT**	**SiC**	**SiC-BNNT**	**B_4C**
Hardness (GPa)	18.97	16.83	15.87	27.89	24.84	30.49
Fracture toughness (MPa.√m)	3.85	3.96	3.98	3.01	3.14	3.74
Density g/cm^3	3.80	3.82	3.74	3.10	2.95	2.43

3.2 Experimental

3.2.1 Chemical and Microstructure Analysis

The monolithic ceramics specimens were prepared through the standard ceramography procedure. The samples were cut using a diamond saw on Struers secotom-10, hot mounted and polished on a Metcomet semi-automatic machine. Ultrafine polishing using Mastermet

colloidal silica suspension was done as the last preparation step. Specimens for etching were dis-encapsulated from the epoxy mounting using a mechanical bench vice. While ZTA specimens were etched in a convection muffle air furnace, SiC specimens were etched in a controlled atmosphere furnace in both vacuum and argon gas environments. Both materials were etched at 1300^{o}C with 30 minutes soaking time. As-received, polished and etched specimens were studied using both Scanning Electron Microscopy (SEM) and polarised Optical Microscopy (OM). The specimens for SEM study were coated with gold before imaging was performed at 20 KeV at a working distance of 15 mm. For the OM characterisation, a Nikon Eclipse L150 microscope and the clemex image analysis software were used.

The SEM Secondary Electron (SE) mode was used to study the grain structure. The grain size was measured by the intercept method according to the ASTM E112-10 standard [131]. Chemical composition determination was done using SEM-Energy Dispersive Spectrometry (EDS). The qualitative and quantitative analysis was carried out using a collection time of 30 seconds. Automatic image analysis according to the ASTM E1245 standard [132] was also used to measure the volume fraction of second-phases using an Electron Back-Scattered Detector (EBSD) in SEM. In addition to EBSD, a phase analysis was performed using X-ray diffraction technique. The X-ray diffractometer was equipped with a monochromator using Cu Kα radiation. The scans were performed from 10 to 90 degree at 2θ range, 50 steps per degree and 2 seconds acquisition time per step.

3.2.2 Porosity and Density Determination

The density was evaluated using three methods including the Archimedes' principle, the ultrasonic test, and microscopy. The Archimedes' method was applied on the two materials

according to ASTM B962-08 [133] using distilled water. Ultrasonic testing was adopted only for ZTA sample because of its high porosity. This test involved measuring the longitudinal sound velocity and path length by ultrasonic waves [134]. Considering the sample thickness and using appropriate equations 3.1 and 3.2 [135], the longitudinal (V_L) and transversal (V_T) sound velocities are calculated. Ultrasonic testing has been proven accurate within 1 to 2% [44] for pore size distribution evaluation in ceramic specimens.

$$\boldsymbol{V_L = V_{LO}\,(1-P)^m} \tag{3.1}$$

$$\boldsymbol{V_T = V_{TO}\,(1-P)^n} \tag{3.2}$$

Where V_{LO} and V_{TO} are the longitudinal and the transversal pore free velocities, respectively; and m and n have constant values of 1.17 and 1.03, respectively. The porosity (P) was analysed using SEM image of polished surfaces on image J software.

3.2.3 Hardness Measurements

Polished surfaces were indented using three indentation methods. The three methods were adopted because of the high porosity level in ZTA and the anisotropy in SiC. The methods include Vickers, Knoop and instrumented indentation otherwise called nano-indentation. Vickers hardness measurements using HV1, HV2, HV3, HV5, HV10, and HV20, which correspond to indentation loads of 1, 2, 3, 5, 10, and 20 kgf, respectively, were performed on SiC. In addition to the loads on SiC, HV30 and HV50 with loads of 30 and 50 kgf, respectively, were used on ZTA to allow better toughness measurement considering the higher crack resistance in this material. Knoop hardness measurements were performed using HK1, HK2, HK3, HK5 and HK10 with indentation loads of 1, 2, 3, 5, and 10 kgf, respectively. Instrumented hardness was measured using loads of 1, 2, 3, 5, 10, 15, 20 and 25 N on ZTA. In addition to these loads, 0.1 and 0.5 N were selected for SiC because of its higher propensity

to cracking and spalling. In the first two methods, the test was performed in accordance with the procedure in the ASTM Standards C1326-13 for Knoop and C1327-08 for Vickers. A Clark instrument model CV-800AT hardness tester was used with a dwell time of 10 seconds. Indented areas were carefully selected in the case of ZTA to avoid interaction with pores [136]. A minimum of ten measurements for each indentation load were performed on the specimens. Instrumented indentation tests were conducted using a fully calibrated Nano-indenter MTHX S/N 25-0013 and a Vickers indenter. Nine cycles were run for each indentation with a dwell time of 15 seconds each. The hardness was evaluated according to equation 3.3 [50]:

$$\boldsymbol{H_D = \frac{P_{max}}{A_c} = \frac{P_{max}}{26.43 h_c^2}} \tag{3.3}$$

Where h_c is the contact depth; P_{max} is the maximum load and A_c is the area of contact which is a function of the indenter. In the present case, the unitless constant for the Vickers indenter is 26.43.

3.2.4 Indentation Fracture Toughness Measurement

The fracture toughness (K_{IC}) was evaluated by indentation and direct crack measurement (DCM), a method also referred to as Vickers indentation fracture toughness technique. The same Vickers hardness test samples as documented in section 3.2.3 were used. While indentation cracks were measured on SiC specimens at loads of 10 kgf and below, ZTA cracks were measured at loads between 10 kgf and 50 kgf due to its higher toughness.

The length of the crack diagonals was measured immediately after indentation to reduce time dependent effects and potential errors. Optical microscopy at magnifications of 100 to 400 as well as SEM at higher magnifications were used for the measurements. Half the indent diagonal (a) and the crack length (c) measured from the centre of the indent were used for toughness calculation as shown in Figure 3.4 [137] for a single line crack emanating from the

corner. A minimum of 10 indents for each load forming crack were measured and used for the evaluation. Because the type of crack could initially not be determined, all available models were considered in the initial evaluation as summarized in Table 3.2.

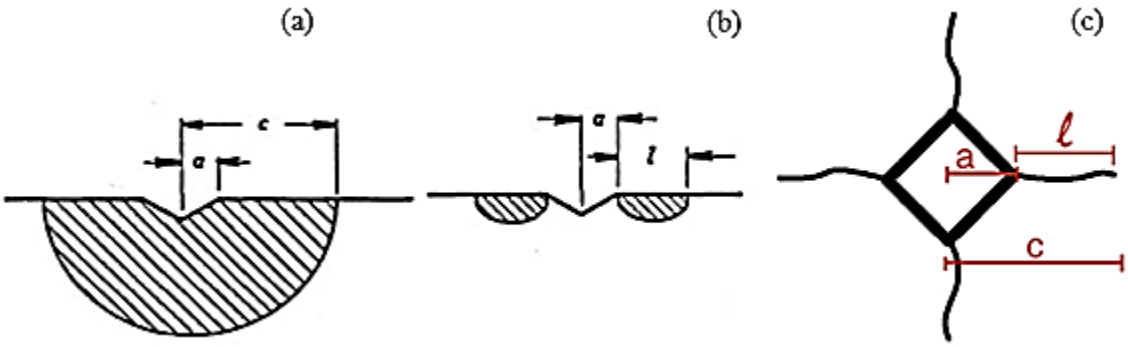

Figure 3.4: Image of crack regimes: (a) median crack; and (b) radial (Palmquivst) crack; and (c) schematic of a well-formed crack.

Table 3.2: Summary of various equations used to calculate the fracture toughness.

Author	Code	Equation K_{IC}	Crack regime	Literature
Anstis	P1	$0.016(\frac{E}{H})^{0.5}\ \frac{P}{c^{1.5}}$	P	[54]
Lawn & Fuller	P2	$0.0515\frac{P}{c^{1.5}}$	P	[55]
Nihara et al.	P3	$\{0.035\ Ha^{1/2}[\frac{E\emptyset}{H}]^{0.4}\ [\frac{l}{a}]^{-0.5}\}/\emptyset$	P	[54]
Shettey et al.	P5	$[\frac{HP}{4i}]^{0.5}[3\ (1-\nu^2)\ (2)^{0.5}\ (\pi \tan\psi)^{0.67}]$	P	[54]
Nihara et al.	M1	$\{0.129(\frac{c}{a})^{-1.5}\ H.a^{0.5}\ (\frac{E\emptyset}{H})^{0.4}\}/\Phi$	M	[54]
Lawn et al.	M2	$0.028Ha^{0.5}\ (\frac{E}{H})^{0.5}(\frac{c}{a})^{-1.5}$	M	[54]
Evans and Charles	M3	$0.16(\frac{c}{a})^{-1.5}Ha^{0.5}$	M	[138]
Lawn and Fuller	M4	$0.0726\ (\frac{P}{c^{1.5}})$	M	[55]

Tanaka	M5	$0.0725\ (\frac{\mathbf{P}}{\mathbf{c^{1.5}}})$	M	[55]
Nihara	M6	$0.203Ha^{0.5}(\frac{c}{a})^{-1.5}/\ \Phi$	M	[54]
Laugier	M7	$0.015(\frac{l}{a})^{-0.5}(\frac{E}{H})^{0.67}\ \frac{\mathbf{P}}{\mathbf{c^{1.5}}}$	M	[54]
Nihara	M9	$0.067(\frac{E}{H})^{0.4}H\alpha^{0.5}\ (\frac{c}{a\_})^{-1.5}$	M	[138]
Lawn	M10	$0.028(\frac{E}{H})^{0.5}Ha^{0.5}(\frac{c}{a\_})^{-1.5}$	M	[102]
Lawn et al.	M12	$0.014(\frac{E}{H})^{0.5}\ (\frac{P}{c^{1.5}})$	M	[55]
Japanese Standard	CF 1	$0.018(\frac{E}{H})^{0.5}\ (\frac{P}{c^{1.5}})$	CF	[55]
Lankford	CF 2	$0.142(\frac{H}{E\Phi})^{-0.4}\ \frac{Ha^{0.5}}{\Phi}\ (\frac{c}{a})^{-1.56}$	CF	[55]
Lawn and Swain	M13	$0.0177\ (\frac{\mathbf{HP}}{\mathbf{c}})^{1/2}$ specific for SiC	M	[55]
Lawn and Swain	M14	$0.0154\ (\frac{\mathbf{HP}}{\mathbf{c}})^{1/2}$ specific for Al_2O_3	M	[55]
Lank Ford	CF 3	$0.142\ (Ha^{\frac{1}{2}})\ (\frac{\mathbf{E\emptyset}}{\mathbf{H}})^{0.4}\ (\frac{\mathbf{c}}{\mathbf{a}})^{-1.56}/\emptyset$	CF	[138]

P is Palmqvist; M is median; CF is curve fitting; E = elastic modulus (GPA); H = Vickers hardness (GPa); $\mathbf{\Phi}$ = Constraint factor ($\approx \mathbf{3}$); ψ = half apex angle of Vickers indenter ($\approx \mathbf{68}$)[2]; P = applied load; ν = Poisson's ratio; a = half-length of indent diagonal; l = crack length measured from indent corner outwards; and c = l + a.

3.2.5 Flexural Strength Measurements

Two methods were used to characterise the fracture strength: equibiaxial using the ring-on-ring test and uniaxial using the four point flexural test.

3.2.5.1 Equibiaxial Ring-on-Ring Flexural Test

The equibiaxial ring-on-ring testing was performed according to ASTM C1499-09. The rings were made of 17-4PH stainless steel; the loading ring diameter was 25 mm, while the supporting ring diameter was 50 mm. Three ZTA samples and three SiC samples were

used based on availability. As required by the standard, the measuring equipment consisting of a Vernier calipers (Mitutoyo Model CD-6" CSX S/N 07441453) and a micrometer (Mitutoyo No 293-348) were validated for accuracy of measurement. The equipment validation report gave 0.9999 and 1 in the regression analysis for ZTA and SiC, respectively. The tests were performed at a displacement rate of 0.15 mm/minute under room conditions. An anti-friction tape was applied on the surface of the test pieces, while the sample edges were taped in the case of SiC to keep the broken pieces together after fracture. The test configuration is shown in Figure 3.5.

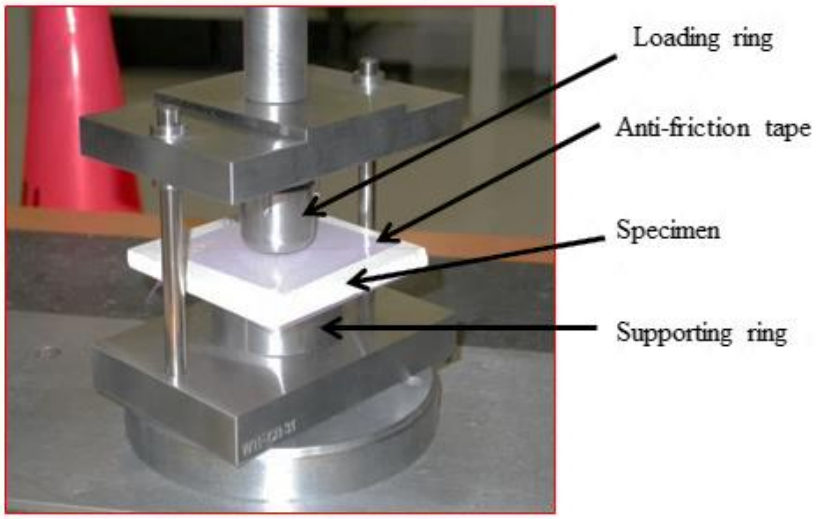

Figure 3.5: Experimental set-up of the ring-on-ring test.

3.2.5.2 Four Point Bend Test

Four rectangular test specimens of each ZTA and SiC were machined into 3 x 4 x 45 mm blocks using a Sectrom 10 cutting machine with a diamond blade. Sectrom 10 machine cutting fluid was used to reduce the effect of machining residual stresses on the specimens. However, cutting dimensions recorded some errors in the range of 5-10% which were accounted for in the calculations. The tests were carried out on a universal testing machine

using a cross-head speed of 0.5 mm/min according to ASTM standard C1161-02. A cylindrical bearing edge made of hardened steel with a 6 mm diameter was used for loading. The test fixture had a 40 mm span. The flexural strength was evaluated according to ASTM standard C 1161-02 using equation 3.4:

$$\sigma_f = \frac{3PL}{4bd^2} \quad (3.4)$$

Where σ_f is the bend or fracture strength; P is the fracture force; L is the support span; b is the specimen width; and d is the specimen thickness.

3.2.6 Low Velocity Impact Test

Two methods were used to characterise the low velocity impact behaviour; these include the charpy and the drop tower tests.

3.1.6.1 Charpy Test

The specimen size was limited by the material thickness which was 7 mm. Hence, two un-notched specimens with size 50 x 7 x 7 mm were prepared for each material. A TMI No 43-1 impact tester with a total energy range of 2 to 15 J was used at a speed of 3.46 m/sec. Pre-fracture and fracture energies were recorded for each test.

3.1.6.2 Drop Tower Test

The drop weight tests were performed on 50 x 50 x 7mm samples. The tests were performed using an Instron Dynatup tester 9200. The specimens were clamped to the fixture along the edges in a rectangular configuration according to ASTM D5628 10 [139] and supported at two base edges, as shown in Figure 3.6. A semi-hemisphere high-strength steel ball of 25 mm diameter was used as the striker; the total weight assembly was 5.02 kg. The mass assembly was made to impact the plate under gravity from heights varying from 20 to 60 mm using the Bruceton staircase method [139].

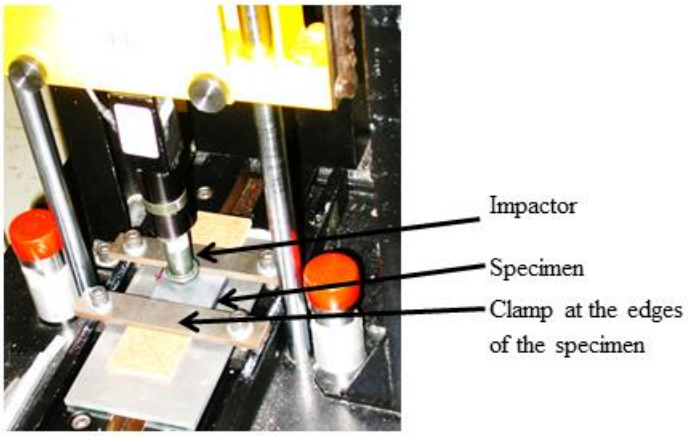

Figure 3.6: Drop tower test set-up.

3.2.7 Modulus of Elasticity Measurement

The modulus of elasticity was characterised using two approaches: (1) the porosity method using the porosity volume fraction, (equation 2.3) [44]; (2) the instrumented indentation method using load-depth of penetration unloading curves [64].

3.2.8 Determining CNT Loading

Table 3.3 summarises reported studies on the effects of carbon nanotube loading in alumina and the resulting mechanical properties including fracture toughness, hardness, and strength.

Table 3.3: Literature data on CNT loading in alumina and resulting properties.

CNT Type	Loading vol%/wt%	Process-ing	Sint-ering	Property Effect and Method of Testing				Liter-ature
				K_{IC} (MPa$\sqrt{m}$)/% ↑ or ↓:method of test	σ_f (MPa)/ % ↑ or ↓	HV (GPa)/ % ↑ or ↓	Relative Density%	
MW	1.1/NA 6.4/NA 10.4/NA	C + BM	SPS	4/ 25↑ : SE 5.5/ 72↑: SE 4.7/ 47↑: SE	375/ 7↑ 530/ 51↑ 480/ 37↑	19/ 11.8↑ 14/ 17.6↓ 11/ 35.3↓	98.1 95.1 92	[130]
MW	5.7/NA	C	SPS	6.03/ 53↑:VI	NA	19.18/ 30↑	~-100	[140]
MW	NA/1 NA/2 NA/3	GPS	PS	3.85/ 10↑ 3.75/ 9↑ :VI 3.63/ 3↑	NA	25/ 9↓ 20/ 27↓ 17.5/ 36↓	-99 -96 -95	[141]
MW	NA/1	C + Doped	HP	5 /40↑: VI	442/ 20↑	19.4/ 18↑	> 99	[142]
MW	1/NA	SG	PS	4.2/ 40↑	465/ 18↑	NA	98.8	[143]

	3/NA			4.7/ 57↑ :VI	363/ 6↓		96.4	
MW	0.9/NA	C	PS + A	5.8/ 45↑:SE	742/ 25↑	NA	99	[144]
MW	NA/1	C	SPS	5 /67↑: VI	NA	NA	NA	[145]
MW	3/1.4 NC 3.2/1.7CV 3.8/1.8CV 3.6/1.9NC	High energy sonicat-ion	SPS	4.2/ 19↓ : SE 3.8/ 22↓ : SE 4.1/ 30↓ : SE 5.2/ 4↓ : SE	468/ 13↑ 377/ 9↓ 456/ 10↑ 313/ 24↓	18.4/ 14↓ 19.8/ 7↓ 19/ 11↓ 17.8/ 16↓	NA	[146]
MW	2.5/1.3 5/2.6	C + BM	HP	5.5/ 45↑ 5.4/ 41↑:VI	NA	18/ 2↓ 15.75/ ↓	99.9 98	[147]
MW	NA/1 NA/2 NA/3	GPS	PS	4.05/ 9↑: VI 3.96/ 5↑ :VI 3.87/ 2↑ VI	NA	23/ 8↓ 15/ 40↓ 10/ 60↓	-98.5 96 94	[148]
MW	NA/2 NA/5 NA/10	C + S	SPS	3.84/ 19↑ :VI 4.14/ 27.8↑:VI N/A	NA	13.16/ 16↓ 7.05/ 55↓ 0.72/ 95↓	NA	[149]
DW	NA/2	Mixing	SPS	5.6/ 12↑ :VI	533/ 10↑	17.8/ 19↓	99	[150]
MW	0.15/NA 0.3/NA 0.6/NA 1.2/NA 2.4/NA	C	PS	5.1/ 31↑ : SE 5.2/ 33↑ : SE 4.4/13↑ : SE 4.1/ 5↑ : SE N/A	266/ 20↑ 249/ 12↑ 235/ 6↑ 115/ 48↓ N/A	18.2/32↑ 18.4/34↑ 15/9↑ 13/↓1.5 N/A	99.47 98.97 98.69 91.27 88.49	[151]
MW	0.15/NA 0.30/NA 0.6/NA 1.2/NA	C + MS	PS 1700	5.5/28↑&5.0/32↑ 5.6/30↑&5.2/37↑ 5.0/16↑&4.4/16↑ 4.7/9↑&4.2/11↑ :VI & SE	265/ 18↑ 252/ 12↑ 239/ 6↑ 120/ 47↓	19.8/11↑ 21/ 18↑ 20.4/15↑ 20/ 12↑	99.9 99.8 99.6 99.3	[152]
SW DW	5/NA 10/NA 5/NA	C	SPS	3 VI; SE-2.95 2.8/ 21.6↓/2.76 3.3	N/A	11/ 52↓ N/A 20.4	99.2 97.4 98.5	[153]
MW	0.9/NA 1.8/NA 3.6/NA	C	SPS	5.9/ 25↑ :VI 6.64/ 41↑ :SE 5.7/21↑ :SE 4.4/ ↓ :SE	689.6/ 27↑ 660/ 22↑ 450/ 14↓	16.8/ 3↓ 15.9/ 9↓ 13.1/ 24↓	99.2 98.9 97.7	[154]
SW	NA/0.5 NA/1 NA/2	C + BM	Ultraf ast	3.5/ 9↑ :VI 4.9/ 53↑ :VI 5.7/ 78↑ :VI	N/A	14.8/ 21↓ 14.5/ 24↓ 11.8/ 37↓	-99 98.5 96.4	[155]
MW	NA/0.5	SG	PS + HIP	6.5/ 55↑:VI	NA	21.1/ 7↑	99.52	[156]
SW	1.4/1	S + BM	SPS	NA	NA	18.5 or 1↓	97.78	[157]
MW	NA/1 NA/2 NA/4 NA/6	SX	PS	6.1/ 93↑ :SE 4.3/ 34↑ :SE 3.8/ 19↑:SE 3.5/ 9↑ :SE	210/ 2.4↓ 195/ 9↓ 165/ 23↓ 165/ 23↓	NA	97.8 N/A N/A 86.3	[158]
MW	NA/0.18 NA/1.07 NA/2.48	Sol Gel US + Spray pyrolysis	SPS	6/ 33↑ :VI 7/ 65↑ :VI 11/ 152↑:VI	NA	17.6/ 3↓ 17.3/ 5↓ 15.75/ 13↓	NA	[159]
MW	0.9/NA	SG	SPS	4.74/ 8.5↑ :N/A	543.8/ 8.3↑	17/ 1.7↓	99.7	[129]

MW	NA/5 NA/5	C + BM HC	HP	5.25/ 61↑ :SE 5.87/ 80↑ :SE	385/ 18↑ 409/ 25↑	NA	99.2 97.4	[160]
MW	4/NA 10/NA	C	HP	NA/94↑:SE NA/42↑:VI NA/66↑:SE NA/47↑: VI	NA/6↑ NA/21↓	NA/10↑ NA/7↓	99.5	[78]
MW	1/NA 3/NA 5/NA	C + BM	PS	4.1/ 24↑ :VI 3.5/ 6↑ :VI 3.6/ 9↑ :VI	543/ 35↑ 403/ 10↓ 286/ 29↓	22.3/ 4↓ 17.9/ 22↓ 12.6/ 46↓	> 99.9 96.5 91.7	[161]
MW	NA/2 NA/5	C	HP	6.8/ 94↑: SE 4.3/ 43↑: VI 5.8/ 66↑:SE 4.5/ 50↑: VI	380/ 7↑ 280/ 6↓	18/ 13↑ 15/ 6↓	99.1 96.2	[162]
MW	0.75/NA 1.50/NA 2.25/NA 3.0/NA	C	PS	3.51/ 6↑ :VI 3.94/ 19↑ :VI 4.50/ 36↑ :VI 4.68/ 41↑ :VI	347/ 31↑ 371/ 40↑ 306/ 15↑ 202/ 24↓	NA NA NA NA	-98 -96 -92 -90	[163]
NA	NA/3.19 NA /5 NA/7.39 NA/8.25	In-situ	SPS 1450	3.83/ 1↓ :VI 5.68/ 46↑ : VI 4.7/ 21↑ :VI 2.47/ 36↓ :VI	NA	3.07/ 67↓ 9.69/ 5↑ 9.98/ 8↑ 9.52/ 3↑	98.2 84.4 79.1 68.8	[164]
MW	NA/2 NA/2	S C	SPS	5.09/ 35↑ :SE 6.35/ 68↑:SE	330/ 9↑ 331/ 10↑	N/A	96.3 97.5	[165]
MW	7/3.9	BM		6.8/ 117↑ :SE	490/ 44↑	NA	NA	[5]
MW	NA/0.5	C		4.8/ 20↑ :SE	572/ 17↑	NA	NA	[5]
MW	3.5/NA	C+ BM	SPS	5.2/ 67↑ VI	NA	NA	99	[166]
MW	3/NA 6/NA	C + BM	HP	5.01/ 79↑ :SE 4.2/ 50↑:SE	410/ 13↑ 330/ 9↓	NA	-99	[167]
SW	NA/1	C	HP	6,4/ 103↑: SE	423/ 19↑	NA	NA	[168]
SW	10/NA	BM	SPS 1150	9.7/ 200↑: VI	NA	16.10	> 99	[76]
MW	NA/2			4.66/ 23↑ :SE	391/ 22↑	NA	NA	[5]
SW	NA/0.5 NA/1	C	HP	5.12/ 62↑ :SE 6.40/ 103↑:SE	402/ 13↑ 423/ 20↑	N/A	99.5 99.1	[169]
NA	/0.1	C	SPS	4.9/ 60↑ :VI	NA	NA	NA	[170]
MW	12/NA	C	HP	5.55/ 80↑ :SE	314/ 4↓	NA	NA	[127]
MW	1.5/N/A 3.3/N/A	SG	SPS	NA/10↑ :VI NA/ 5↑ :VI	NA	19.3/ 1.5↑ 19.5/ 6.6↑	-99.5 -99.5	[171]
MW	NA/1	C	HP	3.9/ 0↑ :VI	554 / 43↑	NA	98.9	[172]
SW	10/NA	BM	SPS	3.33/ 3↑ :SE	NA	NA		[5]
SW	NA/0.1	C	SPS	4,9 or 31↑;VI	NA	NA	NA	[173]
SW	5.7/NA 10/NA	BM	SPS	7.9/ 139↑ :VI 9.7/ 194↑ VI	NA NA	20/ 1.5↓ 16.1/ 20.↓	100 100	[174]

SX is shearing extrusion; U is ultra-sonication; BM is ball-milling; GPS is gas purging sonication; C is colloidal; SG is sol-gel; VI is Vickers indentation method; PS is pressureless

sintered; HP is hot pressed; SPS is spark plasma sintered; SE is SENB, single edge notch beam; HIP is hot isostatic pressed; ↑ or ↓are %increase or reduction, respectively; NA is data not available; SW is single-walled CNT; MW is multi-walled CNT, DW double-walled; NC is not covalent; CV is covalently functionalised; A is Annealing; HC is Hydrothermal crystallisation.

3.2.9 Characterisation on Nanotubes

3.2.9.1 Microstructure Characterisation

The characterisation of BNNT and CNT focused on determining their level of purity and relevant physical properties. Furthermore, the dispersion of the nanotubes in the alumina matrix, the thermal stability of the nanotubes in the composite during processing (especially during heating) and the development of the interfacial bonds in the composite were investigated

Scanning electron microscopy (SEM) and optical microscopy (OM) were used to characterise the as-received nanotubes. The characterisation gives direct observation of their size, shape and structure.

The X-Ray Diffraction (XRD) was used to study the level of impurities using Cu Kα radiation, generated from X'PERT PRO (Phillips) at 45 KV, 40mA, and the results were analysed using the MD I Jade 7 software.

Raman analysis was performed using an excitation wavelength of 514 nm on Renishaw in Via Reflex Raman microscope (Fig. 3.7). The samples were prepared by sonicating approximately 0.5-1 mg of nanotubes in 1 ml of reagent grade acetone for a period of 20 min, after which several drops of the suspension were transferred to glass microscope slides.

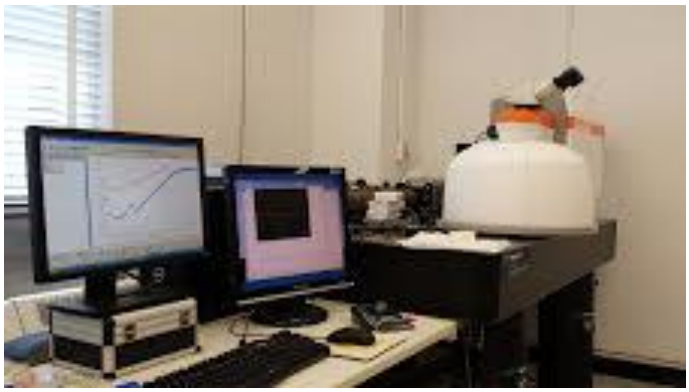

Figure 3.7: Set-up of the Raman equipment.

3.2.9.2 Measurement of the Thermal Stability of Nanotubes

Crucibles for the direct heating testing were made from a carbon electrode to serve as substrate. The crucibles were machined to 12 mm diameter and 12 mm thickness with a centrally drilled hole of 1 mm diameter and 1 mm in depth. Specimens of the BNNT and CNT were filled into the crucibles and heated to a range of temperatures in air, vacuum and argon environments with different dwell times. The specimens were observed before and after heating under OM and SEM.

Thermo-gravimetric analysis using TGA, Netzsch TG 209 F1 Irish, was employed to further analyze the thermal stability of the samples. For the TGA measurements, approximately 10 mg of sample was oxidized in flowing air at 50 sccm (standard cubic centimetre per minute) using a temperature ramp of 10 °C/min from room temperature to 950 °C.

3.2.9.3 Wettability

The wettability test was carried out on the nanotubes in order to determine contact angles and their degree of hydrophobicity, which gives a measure of the interfacial bond they can develop with a matrix. Water was used as the solvent because it has high flow rate enabling

it to be dispensed in the form of drops of 2 µl through a micro-syringe. Figure 3.8 below shows the test set-up.

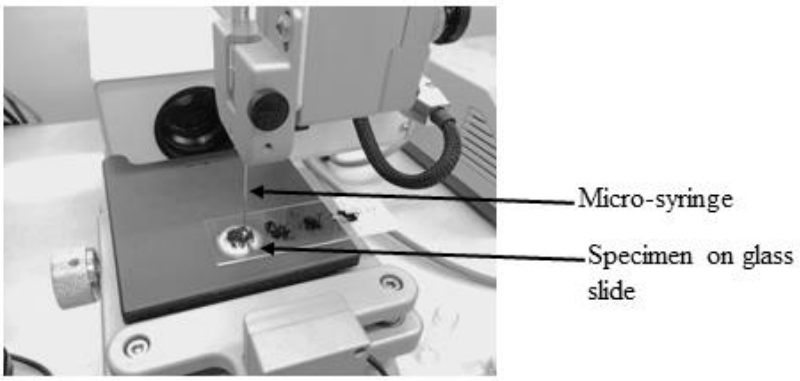

Figure 3.8: Set-up of the contact angle goniometer equipment (Rame Hart model 100) used for the wettability test.

3.2.9.4 Dispersion of Nanotubes

The conventional powder metallurgy route was used for the dispersion of the nanotubes in alumina powder. Dry ball milling tests were performed using a Pulverisette Planetary Mill and a rotation speed of 250 rpm. The nanotube content was kept constant at 1vol% (0.45 g) in total powder loads of 8 g. Stainless steel balls of 10 mm diameter each weighing 4 g and a powder-to-ball weight ratio of 1:7 were used. Nanotube and alumina powders were pre-hand-mixed (0 hour) and specimens were taken after 1, 2, 4, 8, 16, and 24 hours milling time. All the specimens were then analysed in SEM.

3.2.10 Failed Ceramics from DOP Test

3.2.10.1 Microstructure Investigation

After ballistic testing, shattered ceramic fragments still attached to the bonding agent were investigated under OM and SEM. Also, microstructural investigations were carried out on the specimens cut from the failed ceramic areas away from the penetration point. These specimens were mounted and polished using standard ceramography procedures. Some of the

polished specimens were etched in air or argon environments (as was applicable) at 1300 ^{o}C for one hour. Furthermore, SEM was used to characterise the degree of dispersion and/or agglomeration of nanotubes as well as potential inclusions in the ceramics. For some of the materials, fragments and etched specimens were used to measure the grain size and the porosity using SEM and the image J software.

Polycarbonate was used as backing material. It is similar to fibre materials such as Kevlar and aramid often used in personnel armour. The thickness and the diameter of the backing were 300 mm and 150 mm, respectively. The used tile dimension of 100 x 100 mm is above the specified minimum dimension of 70 x 70 mm recommended by Hazel and the thickness of about 5.85 mm is greater than the lower limit of 5 mm recommended for the AP 7.62 projectile [99]. In addition, the tiles were chamfer at the edges in order to eliminate or reduce edge effects during the test. The used 7.62 mm x 51 mm NATO steel core ammunition generated projectile velocities between 870 and 890 m/s which corresponds to level IV threat. The projectiles had a sonic velocity of 4.94 km/s [9]; a hardness of 600 HV and dimensions of 35 mm in length and 7.61 mm in diameter. The depth of penetration tests were carried out by the Canadian Forces armour development programme. The evaluation of the ballistic performance was performed using both performance index and property correlation to the depth of penetration.

CHAPTER 4

RESULTS

4.1 Commercial Ceramics

This section presents the results of the characterisation on ZTA and SiC.

4.1.1 Microstructure

4.1.1.1 As-received Ceramic plates

Unpolished surfaces of the materials are presented in Figures 4.1 and 4.2. The striking face of ZTA (Figures 4.1a and b) contained features made up of voids of about 30 µm in diameter. No such features are observed on the back surface as presented in Figure 4.1c. No distinct features are observed on either face of SiC plates as seen in Figure 4.2, except black particles suspected to be residues of sintering additives.

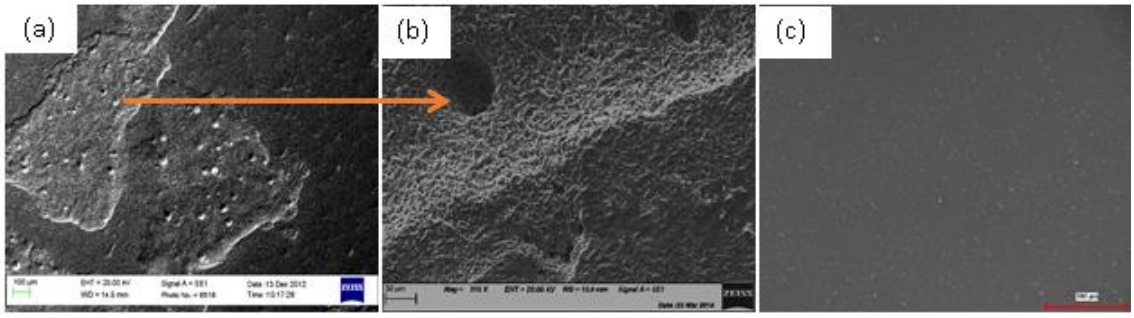

Figure 4.1: SEM images of as-received samples of ZTA: (a) ZTA strike surface revealing some structural features; (b) higher magnification on (a) revealing voids; (c) OM image of the back surface of ZTA.

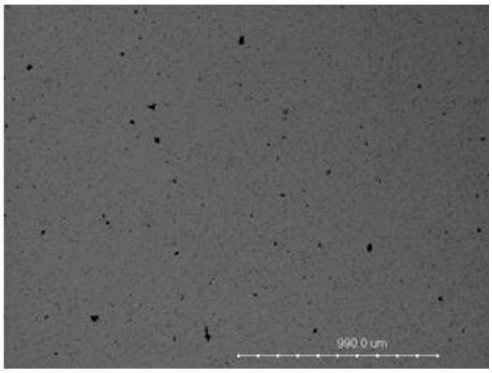

Figure 4.2: SEM image of the unpolished surface of a SiC plate revealing black particles suspected to be residues of sintering additives.

4.1.1.2 Elemental Composition and Secondary Phases

SEM-EDS analyses of the materials are presented in Figures 4.3 to 4.4. ZTA is made of 85.6% α-Al_2O_3, 12.9% ZrO_2 and 1.5% sintering additives, which include Niobium with 0.37% volume fraction. The XRD analysis (Fig. 4.5) confirmed the presence of zirconia in ZTA. The ZrO_2 particles are of various size and shape and are homogeneously dispersed in the alumina matrix (Fig. 4.3b). These particles were found sitting most often at grain boundaries adopting the shape of the triple point junctions. There are also a few particles with a spherical shape and 1 µm diameter embedded in the alumina matrix.

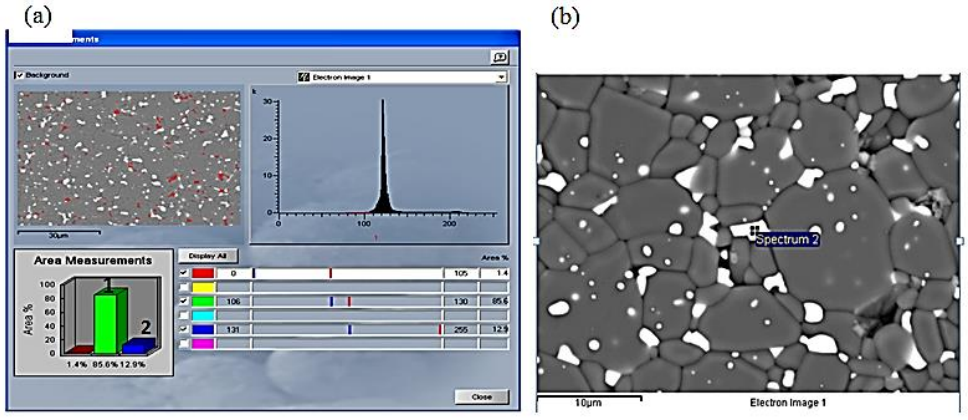

Figure 4.3: EDS analysis on ZTA: (a) mapping to identify the composition of the material in (b). Insert in (a) shows (1) alumina; and (2) ZrO_2, which are white particles in (b).

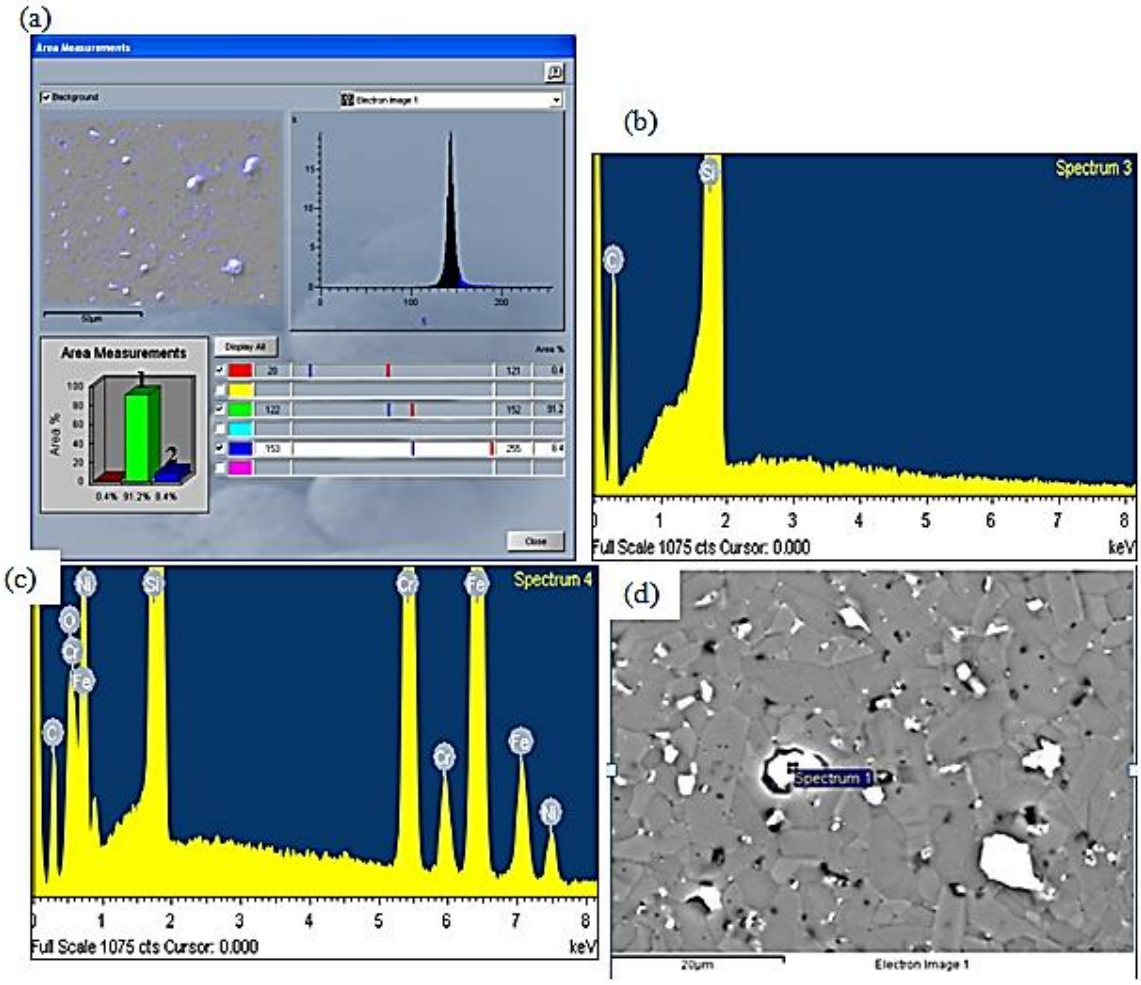

Figure 4.4: EDS analysis of SiC: (a) and (b) SEM-EDS analysis on the material revealing 91.2% SiC phase, 8.4% second phase and 0.4% third phase which essentially was sintering additives as revealed by (c); (d) SEM image showing the main matrix as SiC, deuterides phase inclusions as white spots and residues of sintering additives as dark spot.

In contrast, SiC is made up of 44.56% C, 54.30% Si, 0.8% Sn and 0.78% I with X-ray diffraction showing 91.2% α-SiC, 7.28% sintering aids and 1.52% trace elements. Further analysis revealed that SiC contains compounds of Cr, Si, Fe, Ni and C. XRD analysis of SiC (Fig. 4.6) exhibited a heterogeneous matrix comprising α-SiC, Ce_2-$Pd_{2.06}$-$Sn_{0.94}$ and ($T_{i0.33}V_{0.6}$ $Mn_{0.07}$) $D_{1.28}$ (deuterides) with weight fractions of 91.2%, 5% and 2.28%, respectively. Further confirmation of the deuterides phase is shown in Figure 4.7, which revealed blistering on vacuum etched sample.

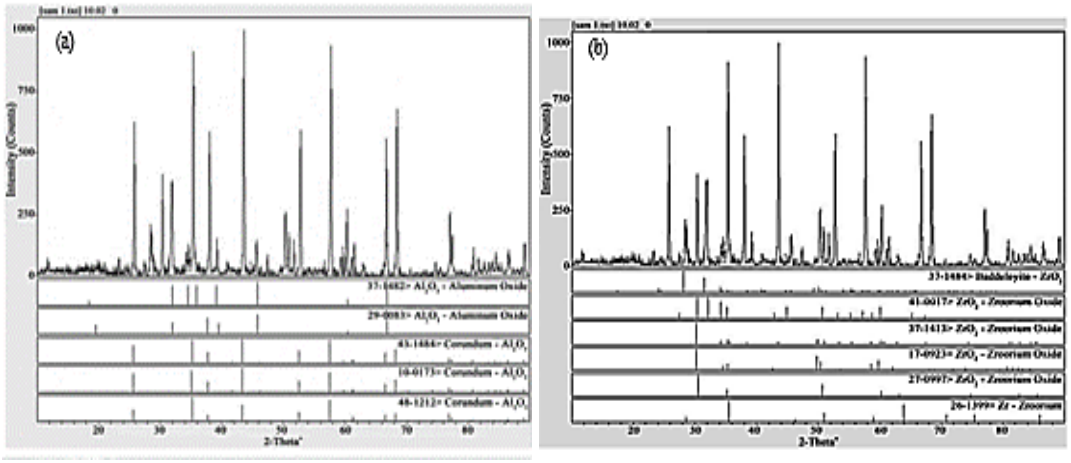

Figure 4.5: X-ray diffraction spectra for ZTA containing two major phases: ZrO_2 and Al_2O_3.

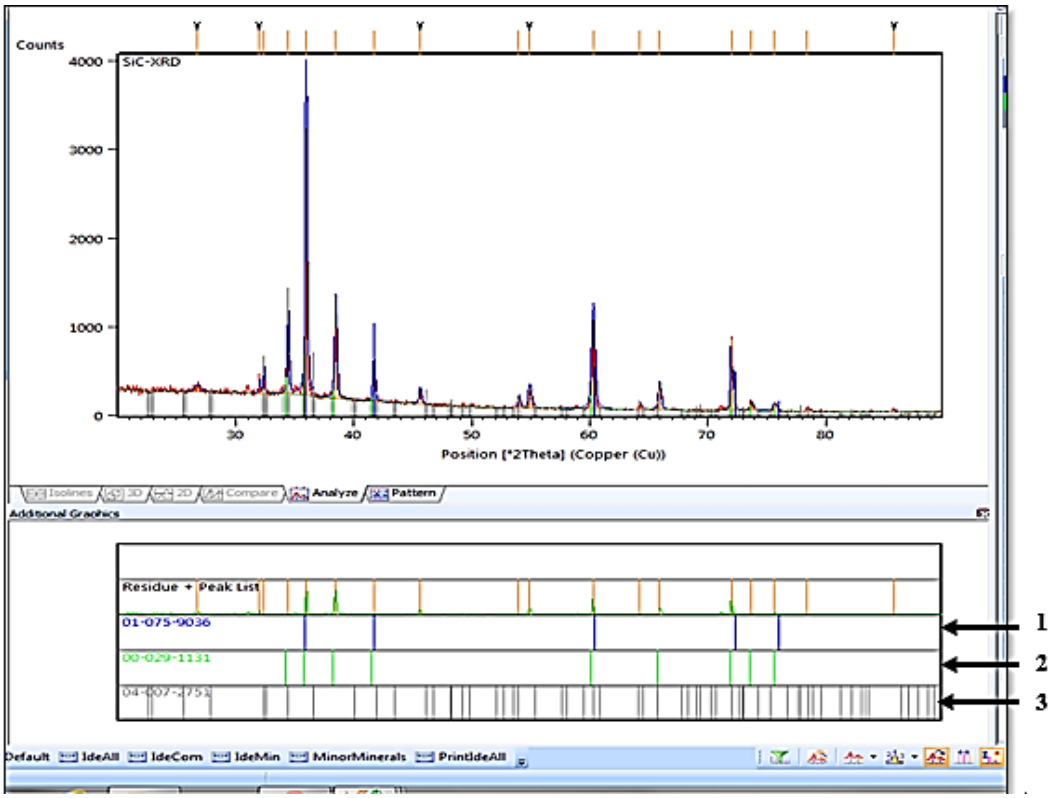

Figure 4.6: XRD line spectra for SiC specimen. Numbers 1, 2 and 3 point to the line spectra of (Ti0.33V0.6 Mn0.07) D1.28, α-SiC and Ce2-Pd2.06-Sn0.94 phases, respectively.

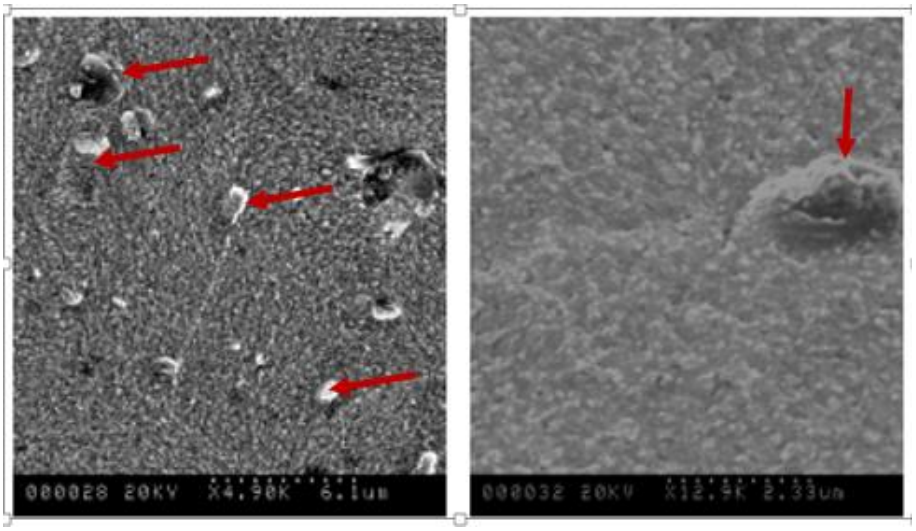

Figure 4.7: SEM micrograph of SiC after thermal etching under vacuum environment showing a blistered surface.

4.1.1.3 Grain Size

The matrix grain structure for ZTA and SiC was bimodal with varying grain size and both equiaxed and elongated grains as shown in Figures 4.8a. For both materials, the grain size varied between 1 and 10 μm with SiC showing the higher grain aspect ratio. ZrO_2 particles in ZTA were mostly smaller than 1 μm with few larger particles being about 5 μm diameter.

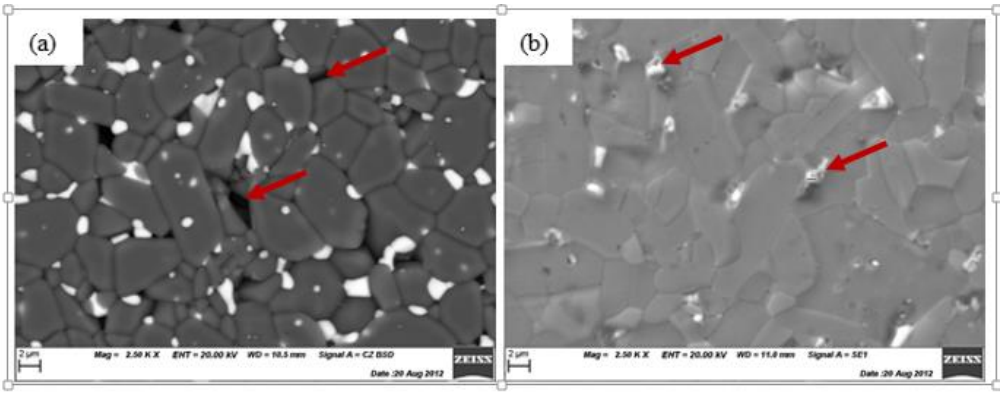

Figure 4.8: SEM images revealing grain size and shape: (a) ZTA; (b) SiC.

4.1.1.4 Defects and Heterogeneities

Defects in ZTA and SiC include porosity, inclusions, density gradients, additive residues and non-uniform additive distribution as revealed in Figures 4.3, 4.4, 4.7 and 4.8. Ultrasonic test results on ZTA are presented on Figure 4.9. They revealed a non-uniform distribution of pores, leading to a marked density gradient. The non-uniform distribution of pores is revealed by the large range of longitudinal velocities (between 9000 – 13000 m/s) resulting in different effective path lengths of the ultrasonic waves. Figure 4.9 was used to evaluate the porosity concentration according to equation 4.1 as presented in Table 4.1.

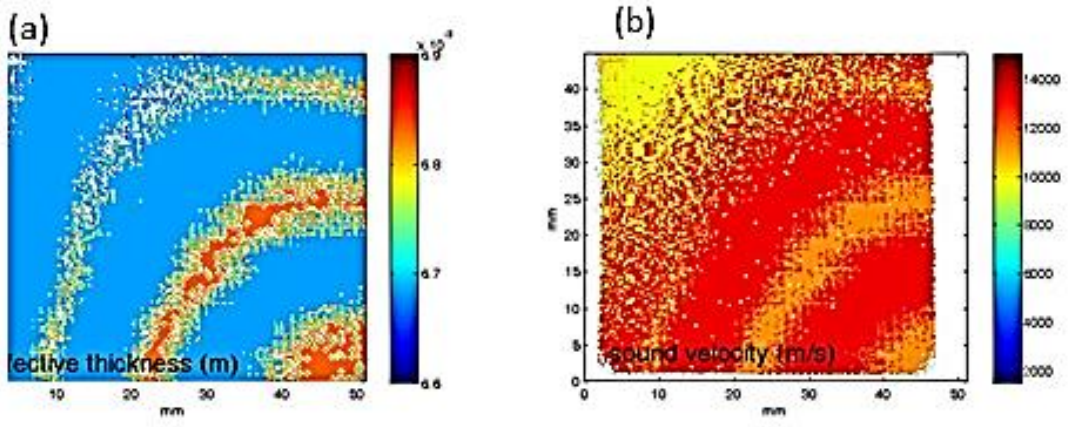

Figure 4.9: (a) Effective thickness and (b) sound velocity in ZTA revealing a non-uniform porosity distribution [134].

Table 4.1: Ultrasonic test results on ZTA: VL was measured while VT and porosity were calculated using relevant equations 3.1 and 3.2 given in chapter 3 and equation 4.1.

Parameter	Longitudinal sound velocity V_L (m/s) Measured	Transverse sound velocity V_T (m/s) Calculated	Porosity (%) Calculated
Minimum sound velocity	9000	5562	26.5
Maximum sound velocity	13000	7618	0
Range	9000-13000	5562-7618	0-26.5
Relative sound velocity	11500	6877	9.7

$$V_T = \alpha V_L - \beta V_L^2 \quad (4.1)$$

Where V_{LO} and V_L are the pore-free and pore-containing longitudinal sound velocities, respectively; V_{TO} and V_T are the pore-free and pore-containing transverse sound velocities, respectively; m = 1.17, n = 1.03, $\alpha = 0.69$ and $\beta = 8 \text{ X } 10^{-6}$.

Higher sound velocity means low pore volume fraction as is the case for the darker (red) areas in Figure 4.9a. In contrast, lower sound velocity means high pore volume fraction indicated by the brighter (blue) areas in the same Figure. The high porosity in this material was also evident in the SEM micrographs as illustrated in Figure 4.10.

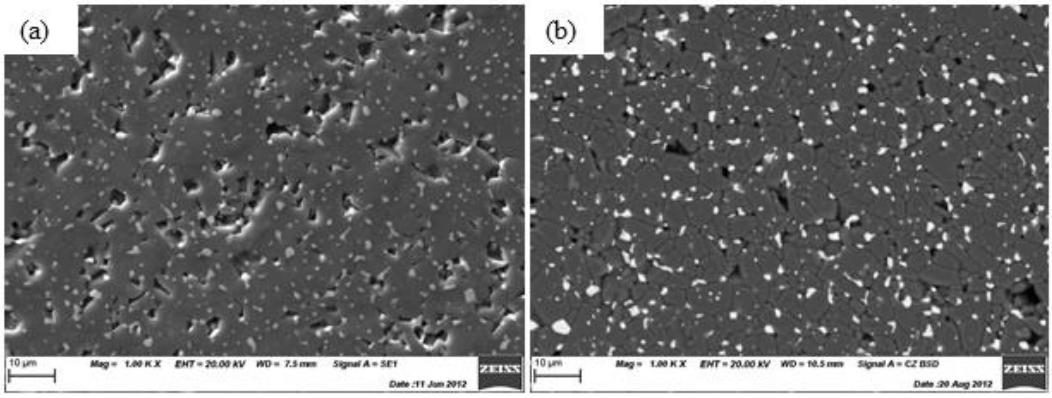

Figure 4.10: SEM images of ZTA: (a) porosity in a polished and unetched sample; (b) porosity and microstructure in an etched sample.

Pores were widely distributed within the plate volume, but were preferably located at grain boundaries. They were various in sizes with the larger pores having sizes of up to 5 μm in diameter as evident in Figures 4.10. The high porosity level of ZTA makes it semi-transparent to light. Pores in SiC seem to be embedded in inclusions or sinter residues (see boxes in Figure 4.11). Pores in SiC are less than 1 μm in size as measured in SEM.

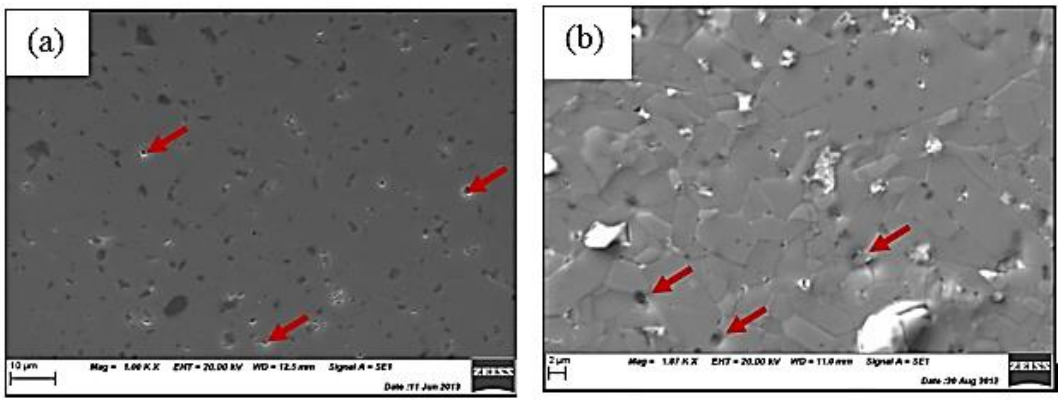

Figure 4.11: SEM images in SiC showing the relatively low porosity in arrows: (a) unetched specimen; (b) etched specimen.

4.1.2 Density

From the ultrasonic test results of the porosity evaluation on ZTA Figure 4.9, the density was evaluated using equation 2.1 [44]. It was assumed that the maximum longitudinal sound velocity V_L is achieved at 0% porosity or 100% density (ρ_o). The theoretical density of ZTA was estimated using the rule of mixture from the theoretical densities of ZrO_2 and Al_2O_3, which are 6.1 and 3.98 g/cm^3, respectively. Considering their volume percentages of 85.4% and 12.9%, respectively, as measured using SEM/EDS, the theoretical density of ZTA was calculated to be 4.15 g/cm^3.

Furthermore, image J software was used to evaluate the porosity of the materials and the results gave 10% and 2.4% on ZTA and SiC, respectively. This porosity value of ZTA was comparable to that estimated using ultrasonic test. Using the porosities and equation 2.1, the density of the materials was estimated to be 3.75 g/cm^3 and 3.12 g/cm^3 for ZTA and SiC, respectively. In view of the sensitivity of the density measurement, the Archimedes principle was also used to evaluate the density of both materials. The comparative results are presented in Table 4.2.

Table 4.2: Density evaluated through Archimedes' principle and comparison with the porosity method.

Sample	Sample weight W_{sa} (g)	Bouyancy (A)	Density (g/cm^3)	
			Archimedes method	Porosity method
ZTA	17.96024	4.75139	3.78	3.75
SiC	13.03701	4.23279	3.08	3.12

4.1.3 Hardness

4.1.3.1 Vickers Hardness

The variation of material hardness with applied load is shown in Figure 4.12. The average of at least 10 measurements was used for each data point. From this figure, the ZTA showed a hardness of 1700 HV at 1 kgf that drops to 1509 HV at higher test loads (2 kgf to 50 kgf). SiC also showed load dependent hardness with a value of 2596 HV at 1 kgf which is higher than the plateau value of 2413 HV measured at higher loads of 2 kgf to 10 kgf. This is an indication of indentation size effect (ISE), which is primarily caused by incomplete and reversible deformation at low loads as shown in Figure 4.13. The load independent values 1509 HV and 2413 HV were taken as the hardness of ZTA and SiC, respectively.

SiC displayed excessive cracking and spalling at loads beyond 3 kgf as shown in Figures 4.14, which adds to measurement uncertainties. Hence, its test result was limited to 10 kgf load. On the other hand, measurements on ZTA are compromised by high porosity that made indentation diagonals partly invisible especially at low loads, as shown in Figure 4.15.

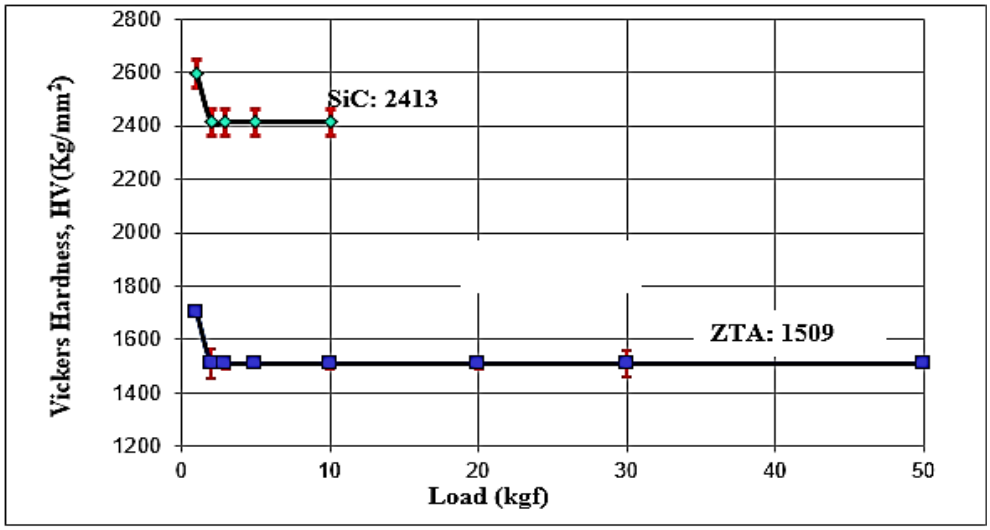

Figure 4.12: Vickers hardness dependence on indentation load

.

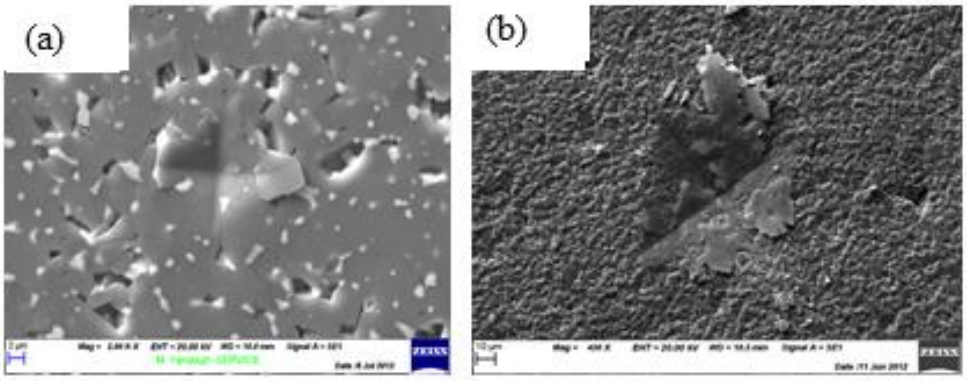

Figure 4.13: SEM images demonstrating incomplete deformation on ZTA at low loads of 1 kg which led to indentation size effect (ISE): (a) polished surface; (b) unpolished surface.

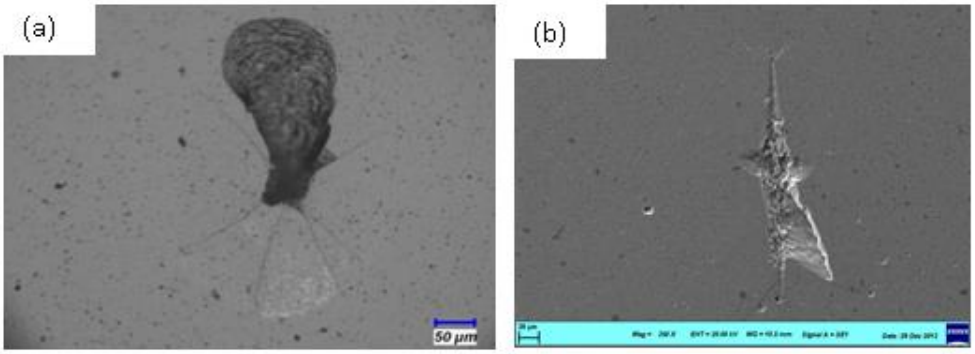

Figure 4.14: (a) OM image of SiC demonstrating spalling and chipping during indentation, rendering Vickers indent measurement difficult; and (b) SEM image showing the much better visibility of Knoop indent corners despite the spalling.

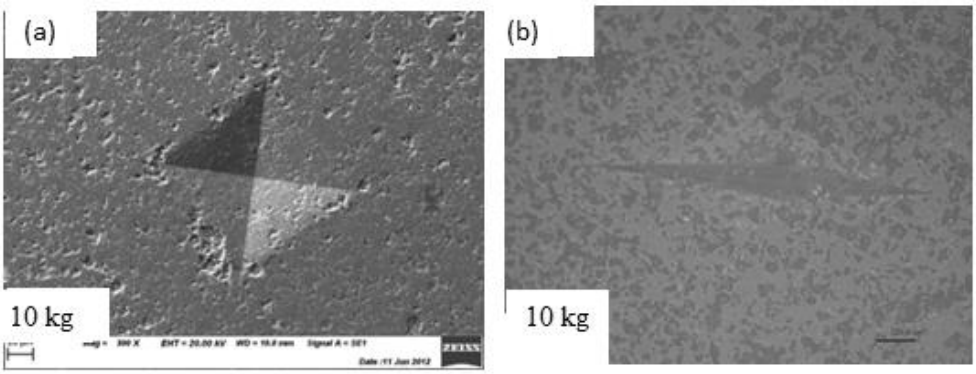

Figure 4.15: (a) SEM image of ZTA demonstrating porosity interaction with a Vickers indent; and (b) OM image showing the much better visibility of Knoop indent corners despite the porosity.

4.1.3.2 Knoop Hardness

The materials behaviour to Knoop indentation is presented in Figure 4.16. The provided hardness values are an average of at least 8 measurable indents. Similar to Vickers hardness, both materials displayed a stronger load-hardness dependency, which illustrates an accentuated ISE phenomenon. Evaluated hardness values were 1345 and 2029 HK on ZTA and SiC, respectively, which are averages calculated above 2 kg loads. Crack formed at loads beyond 5 kg and rendered measurement inappropriate.

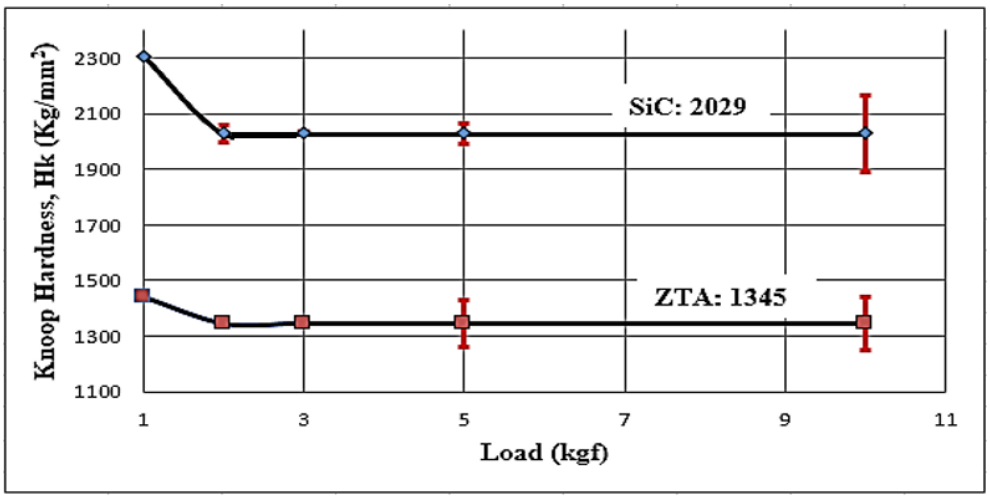

Figure 4.16: Knoop hardness dependence on load for SiC and ZTA.

4.1.3.3 Instrumented Indentation Hardness

Figure 4.17 presents the results of instrumented indentation hardness tests as mean values of nine measurements. No substantial load dependence can be established for ZTA as the hardness continues to fluctuate even beyond 5 N. However, a strong indentation size effect (ISE) can be seen below 2 N for SiC. The recorded average plateau values are 1163 and 2641 HV for ZTA and SiC with a coefficient of variance of 28.12% and 10.64%, respectively.

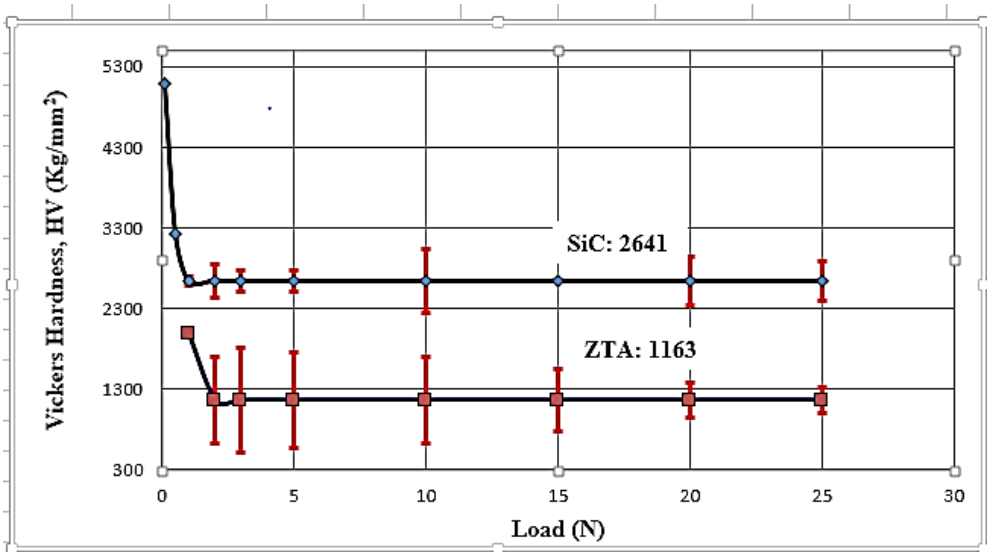

Figure 4.17: Instrumented indentation hardness-load plot for SiC and ZTA.

4.1.4 Indentation Fracture Toughness

Indents with clearly defined radial cracks, as shown in Figure 4.18, were measured for indentation fracture toughness evaluation. The crack size increased with the indentation load. The cracks were visible on ZTA at loads beyond 10 kgf and continued to be visible and measurable till 50 kgf. In contrast, radial crack formation in SiC started even from the lowest load of 0.2 kgf and the load had to be limited at 10 kgf because of excessive cracking and spalling at higher loads that impeded crack measurement.

The crack length c is the length from the midpoint of the indent to the tip of the radial crack and was measured as the average of a minimum of 10 indentations. Crack size and correspondingly calculated K_{IC} are presented in Tables 4.3 and 4.4 for ZTA and SiC, respectively.

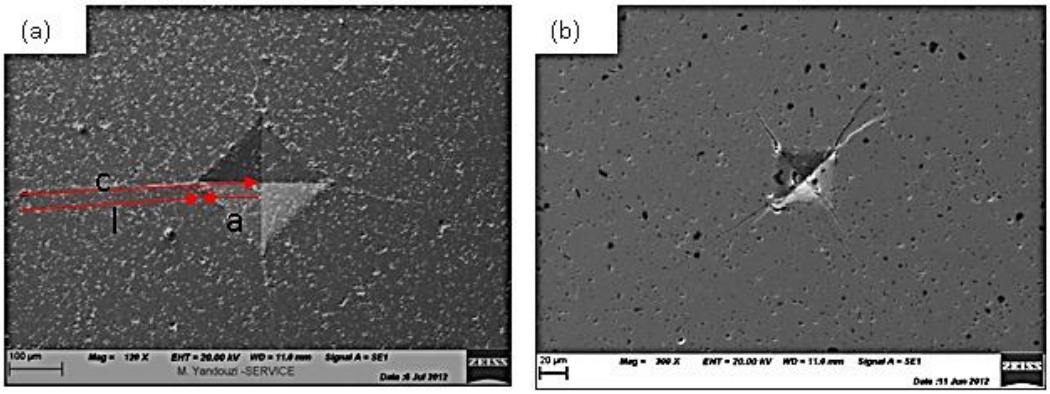

Figure 4.18: SEM images showing Vickers indents and radial cracks: (a) ZTA with crack size parameters: half indent diagonal (a), length of crack measured from the end of an indent diagonal (l), and crack length measured from the centre of an indent to the end of the crack, respectively; and (b) SiC specimen revealing strong cracking.

Also presented in these Tables are c/a ratios that govern the crack regime according to literature. A transition from the radial to the median crack regime is expected at a c/a ratio of 2.5. As the calculated c/a ratios in Table 4.3 were all above 2.5, it can be concluded that the cracks were all in the median crack regime. Hence, this study focuses more on the use of median crack equations presented as M1-M7. For the sake of completeness however, some radial (Palmqvist) crack equations are considered in Table 4.3 as well.

The c/a ratio for ZTA was calculated to be between 2.50 and 2.71. Therefore, equation 4.2 (M2) [54] was adopted, and the result gives a fracture toughness 4.90 MPa√m.

$$K_{IC} = 0.028 H_a^{0.5} \left(\frac{E}{H}\right)^{0.5} \left(\frac{c}{a}\right)^{-1.5} \quad (4.2)$$

Table 4.3: Measured crack size on ZTA and evaluated KIC using different equations.

Load (kgf)		10	20	30	50
Crack parameter	a	56.3	77.6	97.5	124.5
	c	148.2	210.4	243.3	327.3
	c/a	2.63	2.71	2.50	2.63
Equation and K_{ic} values	(M2) Lawn et al.	3.41	3.84	4.82	5.12
	(M3) Evans & Charles	4.13	4.88	5.95	6.25
	(M4) Lawn & Fuller	5.96	6.70	8.40	8.95
	(M5) Tanaka	4.39	5.18	6.34	6.62
	(M6) Lawn & Swain	6.79	6.94	8.75	9.30
	(M7) Lawn, Evans & Marshall	4.79	5.68	6.41	7.25
	(P5) Shetty	3.75	4.39	5.31	5.61
	(P1) Anstis	5.64	6.26	8.06	8.21

Table 4.4: Measured crack size on SiC and evaluated KIC using different equations.

	Loads (kgf)	0.2	0.3	0.5	1	2	3	5	10
Crack parameter	a	5.5	6.9	9.25	13.4	19.6	23.4	30.6	44.2
	c	16	21	28	45.3	70.7	92.3	126.33	210.77
	c/a	2.90	3.04	2.95	3.38	3.61	3.94	4.13	4.77
Equations and resulting K_{IC} values	(M1) Nihara et al.	2.23	2.24	2.50	3.45	3.67	3.55	3.72	3.54
	(M3) Evans & Charles	2.30	2.30	2.49	2.44	2.46	2.51	2.61	2.40
	(M4) Lawn & Fuller	2.22	2.22	2.40	2.36	2.38	2.42	2.52	2.32
	(M5) Tanaka	2.22	2.21	2.40	2.35	2.38	2.42	2.51	2.32
	(M6) Lawn & Swain	3.10	3.20	3.45	3.77	4.16	4.52	4.91	5.28
	(M7) Lawn, Evans & Marshall	1.71	1.70	1.85	1.81	1.83	1.86	1.93	1.78
	(M8) Anstis et al.	1.96	1.95	2.11	2.07	2.09	2.13	2.21	2.04
	(P5) Shetty	2.22	2.27	2.33	2.60	2.84	3.04	3.29	3.45
	(P1) Anstis	1.48	1.48	1.60	1.57	1.59	1.61	1.68	1.55

In Tables 4.3 and 4.4, the modulus of elasticity E was taken from literature as 330 GPa and 410 GPa for ZTA and SiC, respectively. Equation 4.3 developed by Nihara et al. was used to evaluate the fracture toughness of SiC in agreement with literature [54] and a fracture toughness value of 2.98 MPa√m was obtained.

$$K_{IC} = \frac{\left\{0.129\left(\frac{c}{a}\right)^{-1.5} \text{X } H_a{}^{0.5} \text{X} \left(\frac{E\Phi}{H}\right)^{0.4}\right\}}{\Phi} \quad (4.3)$$

Where Φ is a constant taken as 3.0 [54].

4.1.5 Fracture strength

4.1.5.1 Ring-on-Ring Bend Strength

Results of equibiaxial ring-on-ring tests are presented in Figures 4.19, 4.20 and Tables 4.5 and 4.6. From Figure 4.19, it can be seen that the maximum displacements before fracture were 0.4825 mm and 0.4750 mm for ZTA and SiC, respectively. All fractures occurred instantaneously, though some intermittent cracking sounds were heard before fracture of each of the samples. Maximum loads of 22711 N and 21223 N were attained at failure for ZTA and SiC, respectively. Figure 4.20 shows pictures of fractured samples showing both the compressive (left) and tensile surfaces (right). From these pictures, it is evident that the fracture originated in the maximum stress region within the loading ring, which confirms the test validity according to standard ASTM C-1499. It can also be seen that SiC has a higher crack density than ZTA. The crack patterns in ZTA were similar in all samples and essentially resulted into 5 to 7 fragments. Fewer fragments are indicative of higher fracture toughness, higher proportion of energy absorption by deformation and lower proportion of energy absorption by fracture surface formation.

SiC samples were more brittle and their fracture depended on the confinement state of the specimen during test. Edge-taping or surface-taping, as shown in Figures 4.20 e to h, do not affect the fracture strength as evident in Table 4.5, but do affect the fracture patterns. While unconfined samples were pulverised with primary and secondary fractures (Figures 4.20 c and d), the confined samples exhibited only primary fracture patterns similar to ZTA specimens (Figures 4.20 e to h). The high density of cracks in SiC samples indicates increased amount of elastic energy that is released during fracture. In contrast, ZTA has a lower crack density, which is characteristic of a lower amount of elastic energy under load.

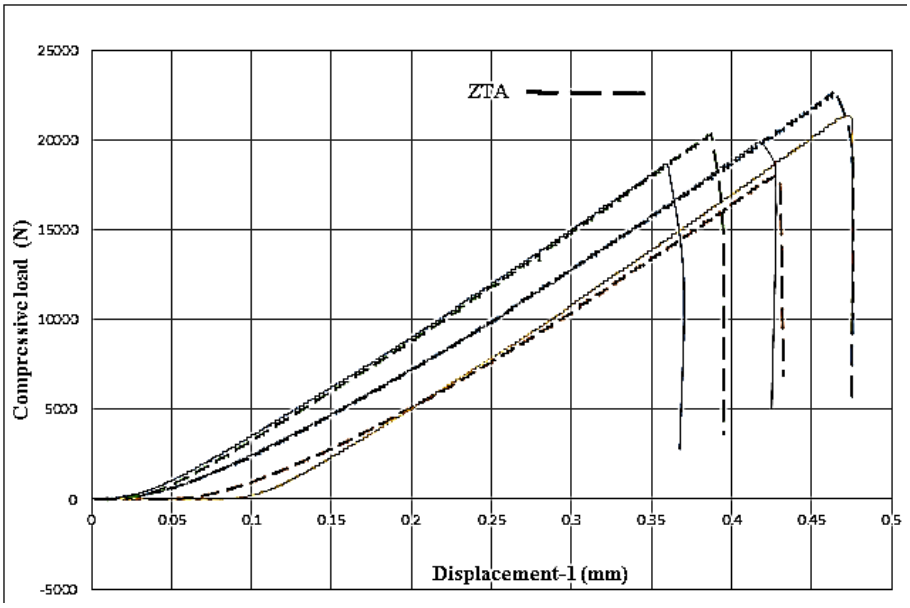

Figure 4.19: Load-displacement curves of ZTA and SiC during ring-on-ring tests. ZTA: dotted lines; SiC: continuous lines.

Calculated strength values ($\boldsymbol{\sigma_f}$) using the ASTM standard equation 4.4 [59] are presented in Table 4.5. The recorded average strength values were 184.4 MPa and 182.5 MPa for ZTA and SiC, respectively. Equation 4.5 was used to calculate the equivalent sample diameter (D). Presented in Table 4.6 are key test ring-on-ring parameters including time to fracture, stress rate, and displacement at fracture according to literature [59].

$$\sigma_f = \frac{3F}{2\pi h^2}\left[(1-\upsilon)\frac{\left(Ds^2 - {D_L}^2\right)}{2D^2} + (1+\upsilon)\ln\frac{Ds}{D_L}\right] \quad (4.4)$$

$$D = \frac{D_L}{0.90961 + 0.12652\frac{h}{Ds} + 0.000168}\ln\frac{l - Ds}{h} \quad (4.5)$$

Where D_s, is the supporting ring diameter 50 mm, D_L is the loading ring diameter 25 mm, ν the Poisson ratios are 0.21 and 0.14 for ZTA and SiC, respectively. The moduli of elasticity are taken to be 330 MPa and 410 MPa for ZTA and SiC, respectively.

Table 4.5: Test data, material parameters and strength as determined using ring-on-ring tests.

Specimen	Max. Load (N)	(h_{aveg}) (mm)	l_{aveg} (mm)	D (mm)	σ_f (MPa)	σ_f mean (MPa)	Std deviation	% Coeff. Var.
ZTA -1	22711	6.871	101.27	109.20	206.9	184.4	21.9	11.9
ZTA -2	17877	6.863	101.25	109.20	163.2			
ZTA -3	19949	6.905	101.36	109.25	179.9			
SiC -1 (untaped)	21223	6.741	101.23	109.20	191.2	182.5	10.1	5.5
SiC -2 (edge-taped)	18684	6.682	101.18	109.16	171.4			
iC -3 (surface-taped)	20325	6.707	101.23	109.21	185.0			

From Table 4.6, it is evident that the stress rates were very low on both materials ranging from 0.92 to 1.06 $\boldsymbol{\sigma/s}$ for ZTA, and 0.64 to 1.15$\boldsymbol{\sigma/s}$ for SiC.

Table 4.6: Key parameters generated and calculated from the ring on ring test.

Specimen	Time to fracture t_f (seconds)	Stress rates ($\frac{\sigma f}{tf}$) MPa/s	Total displacement (mm)
ZTA-1	194.7	1.06	0.4825
ZTA-2	177.8	0.92	0.4425
ZTA-3	175.6	1.02	0.4325
SiC-1	192.3	0.99	0.4750
SiC-2	153.5	1.12	0.3800
SiC-3	160.6	1.15	0.4000
SiC-4	284.8	0.64	0.5300

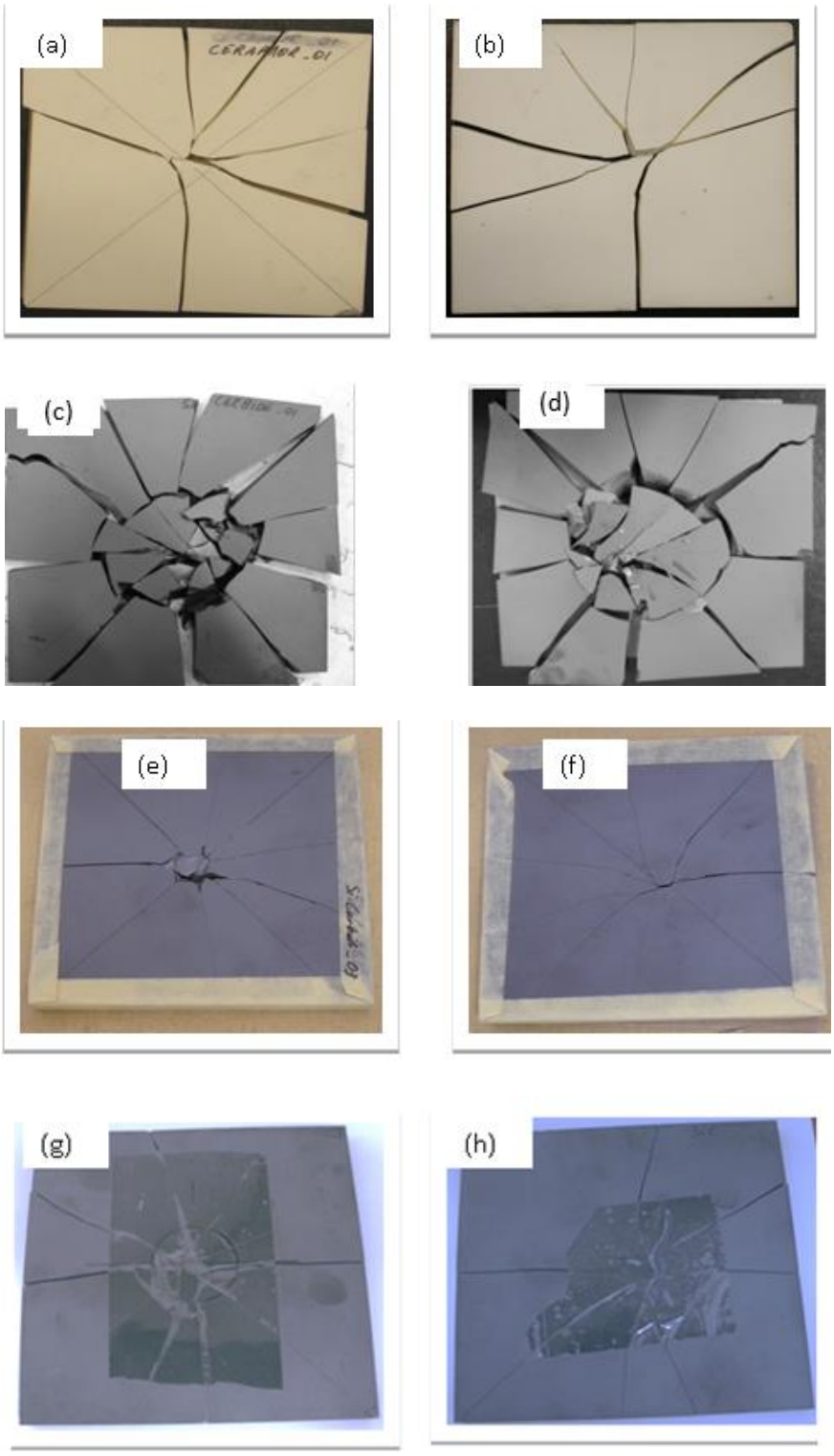

Figures 4.20: Fracture surfaces of front (left) and back (right) sides of the tested specimens: a and b are ZTA; c and d are SiC with untaped edge; e and f are SiC with edge-tape; and g and h are back SiC surface-taped.

4.1.5.2 Four-Point Flexural Bend Strength

Results of the four-point bend tests are summarized in Table 4.7. The flexural strength was evaluated according to ASTM standard C 1161-13.

Table 4.7: Four-point bend test results on ZTA and SiC.

Material	Load at fracture (N)	Flexural strength (MPa)	σ_{mean} (MPa)	Std deviation	% Coeff. var.
ZTA-1	295.43	270.16	292	22.56	7.72
ZTA-2	266.89	318.27			
ZTA-3	415.79	326.29			
ZTA-4	440.61	272.79			
ZTA-5	396.79	293.48			
ZTA-6	459.23	273.62			
ZTA-7	485.49	290.31			
SiC-1	182.10	203.67	242	42.83	17.67
SiC-2	375.31	293.20			
SiC-3	278.48	268.33			
SiC-4	231.02	-			
SiC-5	440.40	253.84			
SiC-6	251.01	192.85			

4.1.6 Modulus of Elasticity

Using the porosity values of 10% and 2.4% for ZTA and SiC, respectively, the modulus of elasticity was estimated using the semi-empirical equation 2.3 [66] to yield values of 272 GPa and 389 GPa for ZTA and SiC, respectively. For this calculation, the pore free moduli of elasticity values were taken to be 330 and 410 GPa for ZTA and SiC as provided by the rule of mixture and [74], respectively.

An alternative method used to estimate the modulus of elasticity is the instrumented indentation hardness test. The modulus was determined using the slope of the load-penetration depth curves below 3N, in the elastic region, according to the Oliver-Pharr method [64]. The results are summarized in Table 4.8. Average values of 306 GPa and 374 GPa were calculated for ZTA and SiC, respectively.

Table 4.8: Young's modulus data generated from the instrumented indentation hardness test.

	Load (N)	**0.1**	**0.5**	**1**	**2**	**3**	**5**	**10**	**15**	**20**	**25**	**Ave. (E) GPa**
E (GPa)	ZTA	-	-	334	279	304	270	232	191	180	235	306
	SiC	616	356	308	296	296	272	240	262	255	200	374

4.1.7 Low Velocity Impact Toughness

4.1.7.1 Drop Tower Fracture Toughness

Results of drop weight tests are presented in Table 4.9 and Figures 4.21 and 4.22. Figure 4.21 shows the test machine generated load-time graphs for the samples during the test. SiC curves exhibit two load peaks at a 60 mm drop height, while ZTA curves exhibited higher load.

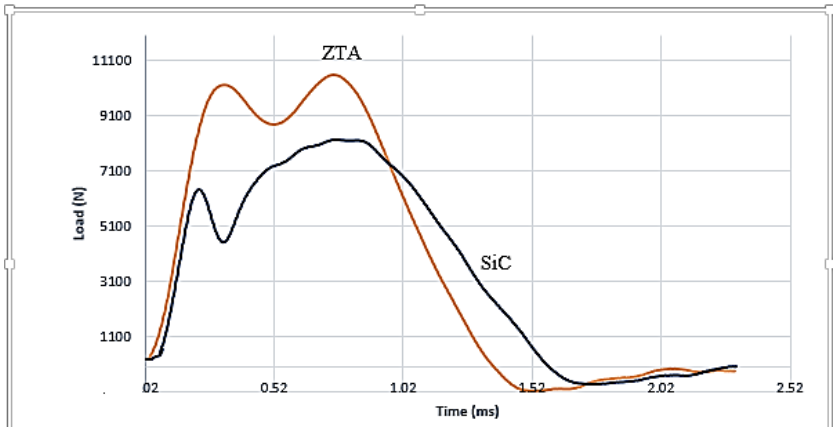

Figure 4.21: Representative Load-time curves for SiC and ZTA during drop weight tests.

Table 4.9 summarizes the results of the drop tower tests. From this table, the transition from non-fractured to fractured samples occurred at a drop height between 22 mm and 30 mm for SiC and between 40 mm and 50 mm for ZTA. However, other important parameters such as impact energy, impact velocity and total energy do not follow this pattern, especially on 60 mm height tests. This may be due to frictions from the machine and/or residual stresses during specimen preparation. A drop height of 50 mm caused a crack to form at the front surface of the ZTA, designated as the strike surface, but did not propagate to the back surface. Test values could not be measured for SiC at a 30 mm drop height due to technical difficulties and the lack of additional specimen to repeat this test.

Table 4.9: Drop weight test result.

Material	**Drop height (mm)**	**Load (N)**	**Impact energy (J)**	**Impact velocity (m/s)**	**Total energy (J)**	**Fracture**
ZTA-1	60	9039.6	2.0165	0.8955	0.8263	Yes
ZTA-2 (P)	50	9759.2	2.5703	1.0110	1.9695	Yes
ZTA-3 (B)	50	10567.5	2.5864	1.0142	0.9966	No
ZTA-4 (S)	50	9325.8	2.5896	1.0148	1.7043	Yes
ZTA-5 (B)	50	10425.7	2.5985	1.0165	0.9663	No
ZTA-6	40	6523.3	2.9932	1.0910	1.4220	No
SiC-1	61	9969.5	3.1486	1.1190	3.1659	Yes
SiC-2	40	8229.3	2.0901	0.9117	0.9176	Yes
SiC-3	40	7223.3	2.1105	0.9161	2.0846	Yes
SiC-4	30	7016.1	-	-	-	Yes
SiC-5	22	6188.6	2.5357	1.0042	2.5361	No

P is the patterned face (strike face); B is the back surface; the drop weight for each test was 5.0292 kg.

Figure 4.22 shows fractured samples. The much higher crack density in SiC compared to ZTA can clearly be seen. At a drop height of 30 mm, SiC broke into seven pieces, as shown in Figure 4.22a, while ZTA broke into four fragments at a drop height of 60 mm, shown in Figure 4.22b.

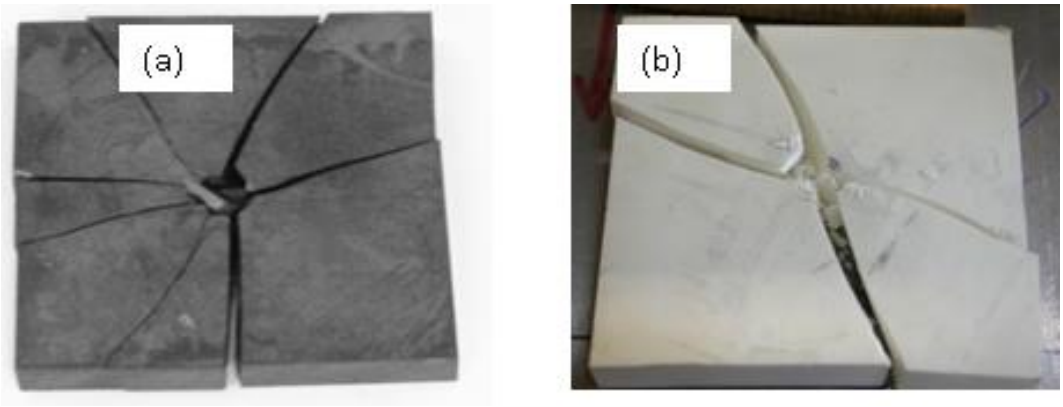

Figure 4.22: Photograph showing the failed front surfaces of the samples: (a) SiC, (b) ZTA.

4.1.7.2 Charpy Impact

The energy absorbed by un-notched specimens with dimensions of 55 X 7 X 7 mm was 0.34 J for ZTA and 0.21 J for SiC. The values provided are averages of two tests on each material. A relative comparison shows that SiC absorbs close to 40% less energy than ZTA.

4.1.8 Fractography

The failure surfaces were examined and analysed for fracture mode. These examinations used the ring-on-ring failed specimens and cracks in Vickers indentation test samples at high loads. Figure 4.23 revealed that the facture surfaces of both ZTA and SiC were crystalline with sharp edges at the point of fracture origin. These features indicate that the materials lack considerable plasticity and fail in a brittle manner. Presented in Figures 4.24 and 4.25 are SEM images of examined failed and fractured specimens of ZTA and SiC, respectively.

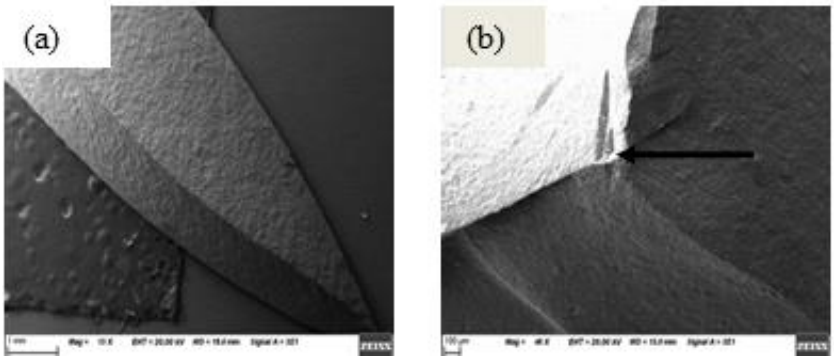

Figure 4.23: (a) SEM images of a crystalline surface of a ring-on-ring failed sample of ZTA indicating brittle failure; (b) Crystalline surface of a failed SiC sample with the arrow pointing to the suspected crack origin.

The fracture mode in ZTA is presented in Figure 4.26. Both images revealed evidence of predominantly intergranular failure accompanied by sections of transgranular failure as shown by arrows on the micrograph. In SiC, the mode of fracture was predominantly transgranular as shown in Figure 4.27.

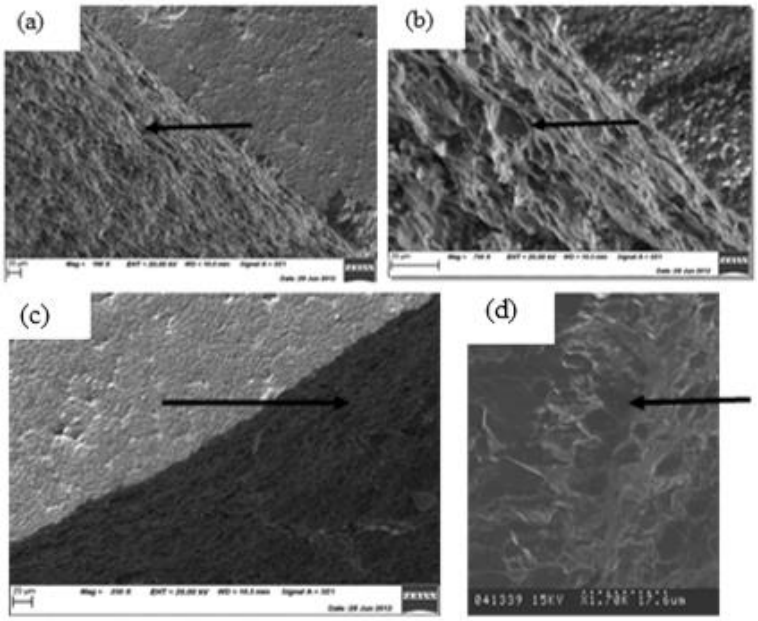

Figure 4.24: SEM images of a fracture surface of ZTA showing: (a) ring-on-ring failed sample in which ridges are connecting pores along the crack propagation path; (b) ring-on-ring failed sample with hackles; (c) Ridges on the crack propagation route; and (d) crack propagating path along grain boundaries indicating that a pore was at the origin of the crack.

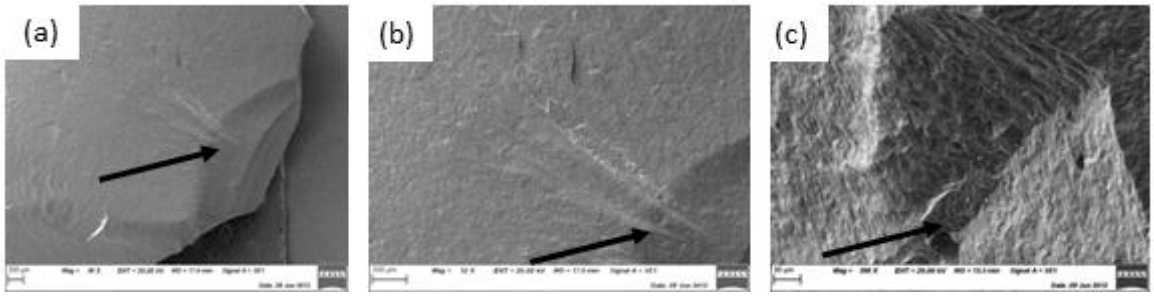

Figure 4.25: SEM images of a ring-on-ring failed sample of SiC: (a) fracture marking hackles emanating from the crack origin; (b) path of crack propagation and crack origin at inclusion; and (c) fracture mirror surface depicting the crack origin.

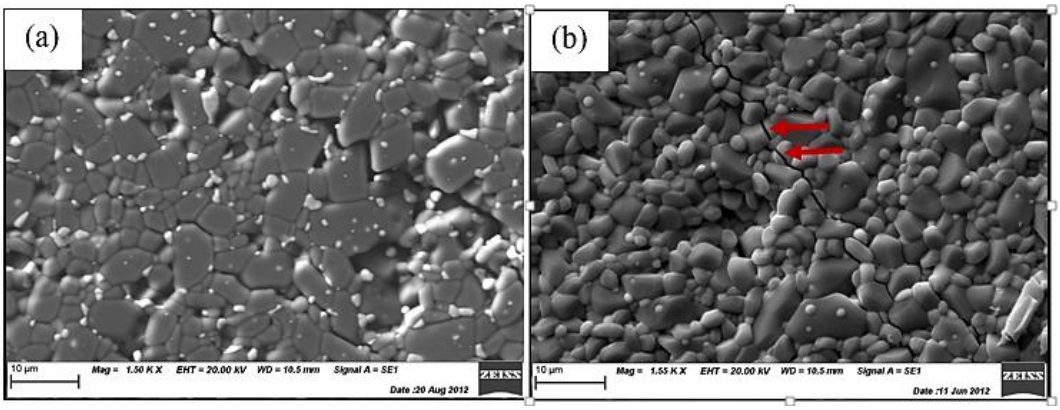

Figure 4.26: SEM images of crack propagation in ZTA: (a) polished and etched specimen showing essentially intergranular; and (b) unpolished and showing a bit of trangranular arrowed.

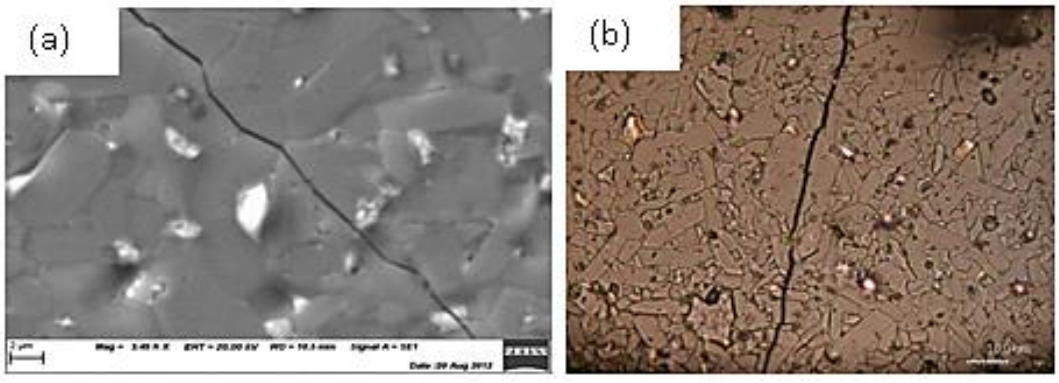

Figure 4.27: (a) SEM image of etched SiC with crack propagating through the grains; and (b) OM image of the material with transgranular crack propagation.

4.2 Nanotubes

This section presents the results on pristine nanotubes characterisation as well as the preliminary dispersion in alumina matrix.

4.2.1 Carbon Nanotube Loading

Figures 4.28, 4.29 and 4.30 revealed the dependency of fracture toughness (K_{IC}), hardness and strength, respectively, on CNT loading. Despite the strong scatters, the general trends suggest that K_{IC} increases while hardness and strength decrease with increasing nanotube volume fraction.

It is noted that beside the nanotube volume fraction, the type of nanotube, nanotube properties and level of purity, functionalisation of nanotube, nanotube dispersion and densification method affect the properties of nanotube reinforced composites.

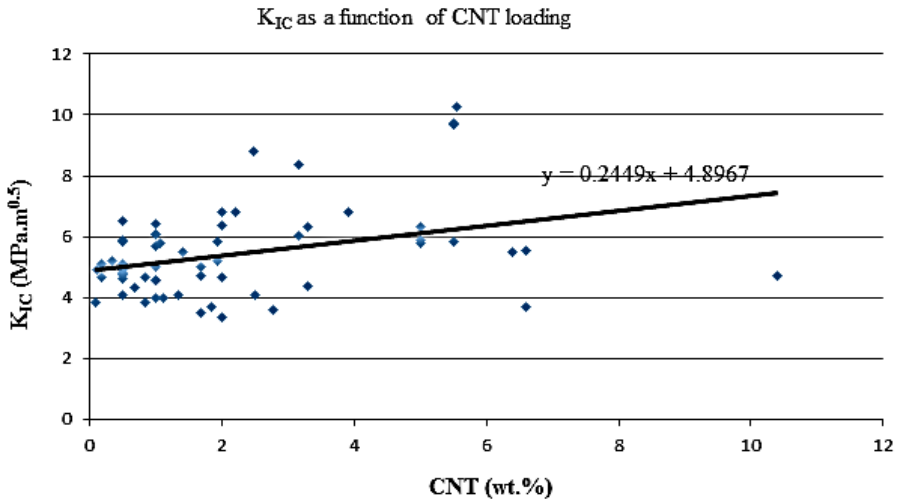

Figure 4.28: Fracture toughness of alumina based composites as a function of CNT loading.

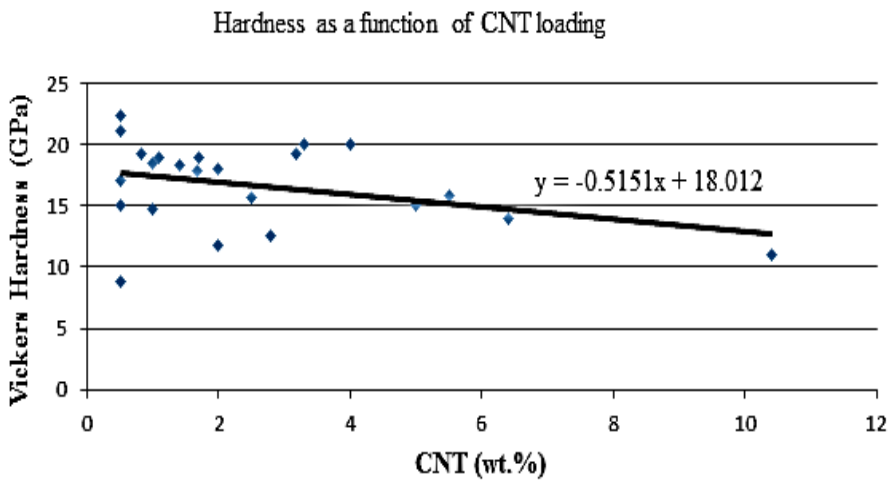

Figure 4.29: Hardness of alumina based composites as a function of CNT loading.

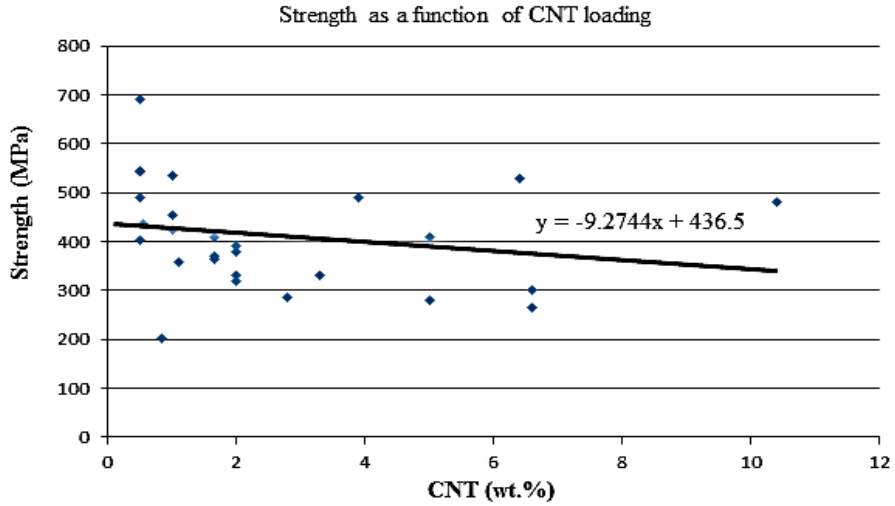

Figure 4.30: Strength of alumina based composites as a function of CNT loading.

4.2.2 Microstructure

Presented in Figures 4.31 and 4.32 are SEM images of as-received BNNT and CNT, respectively, revealing the morphology of the nanotubes. The entanglement of the nanotubes can be observed, which imposes serious limitations to their capacity to homogeneously disperse in the ceramics. The BNNT at lower magnification shown in Figure 4.31a revealed a

flake-like structure, while higher magnifications shown in Figure 4.31b, revealed strong entanglement.

For CNT, Figure 4.43a shows the globular form of the nanotube bundles at lower magnification while at higher magnification (Figure 4.43b), different shapes of cylindrical shells of rolling graphene sheets into seamless (bent, kink and branched) cylinders are revealed. The different shapes of rolling sheets are an indication of defects. At much higher magnification (Figures 4.43c and d) CNT's entanglement can be seen similar to BNNT. Thus, for the two nanotubes, greater work will be required during dispersion to free the nanotube strands from the entanglement.

The XRD patterns of the nanotubes are presented in Figures 4.33 and 4.34 for BNNT and CNT, respectively. The main features on the BNNT pattern is the major peak around 2θ of 26˚, which can be indexed as h-BN (002) plane with a *d* spacing of 3.3 Å, and other smaller peaks, which includes impurities like Fe_3C, carbon contaminating the BNNT, free carbon, and other particles that were not clearly identified. On the CNT pattern, the highest peak is observed around 2θ of 26˚, which corresponds to the carbon (CNT) (002) plane with a *d* spacing of 3.4 Å. Smaller peaks like graphite were observed, an indication of the crystallinity of the CNT. Other smaller peaks, which essentially are impurities or reactions of iron metal, carbon and nitrogen include: Fe_2C, Fe_2N and Fe_3C. There are other smaller peaks suspected to be metal catalysts and possibly amorphous carbon. The pattern further gave the density of the CNT as 2.16 g/cm^3, estimated by the MD I Jade 7 software program.

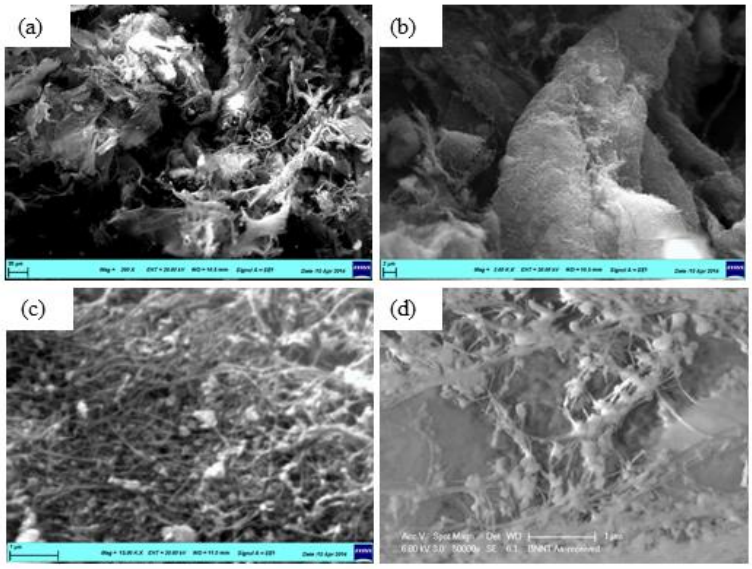

Figure 4.31: SEM images of the BNNT at different magnifications: (a) at lower magnification revealing flake-like and amorphous structure; (b) higher magnification in Figure (a) showing curled nanotube in bundle; (c) at much higher magnification in Figure (b) showing each strand of BNNT accompanied with great entanglement and nanoparticles; and (d) at much higher magnification showing strand of nanotubes.

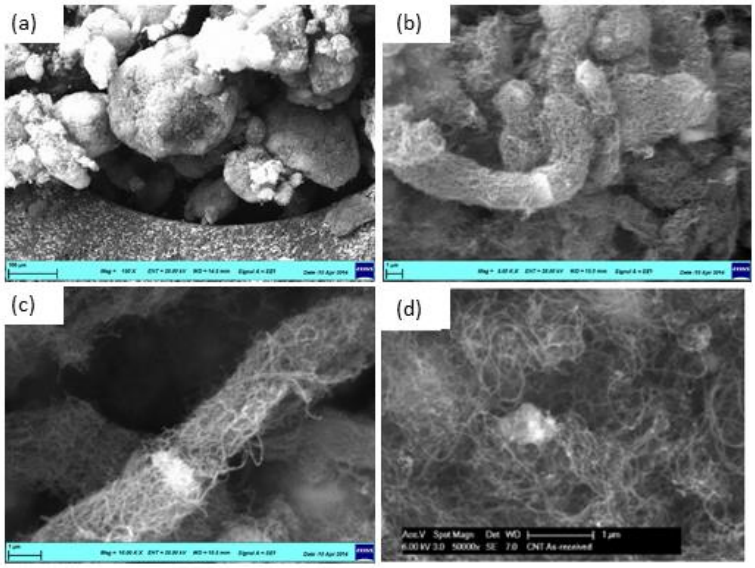

Figure 4.32: SEM images of CNT at different magnifications: (a) at lower magnification revealing a globular form of the nanotubes; (b) higher magnification showing different shapes of rolled graphene sheets; (c) at higher magnification revealing a tubular entanglement with various diameter in bundle; and (d) at much higher magnification showing great entanglement.

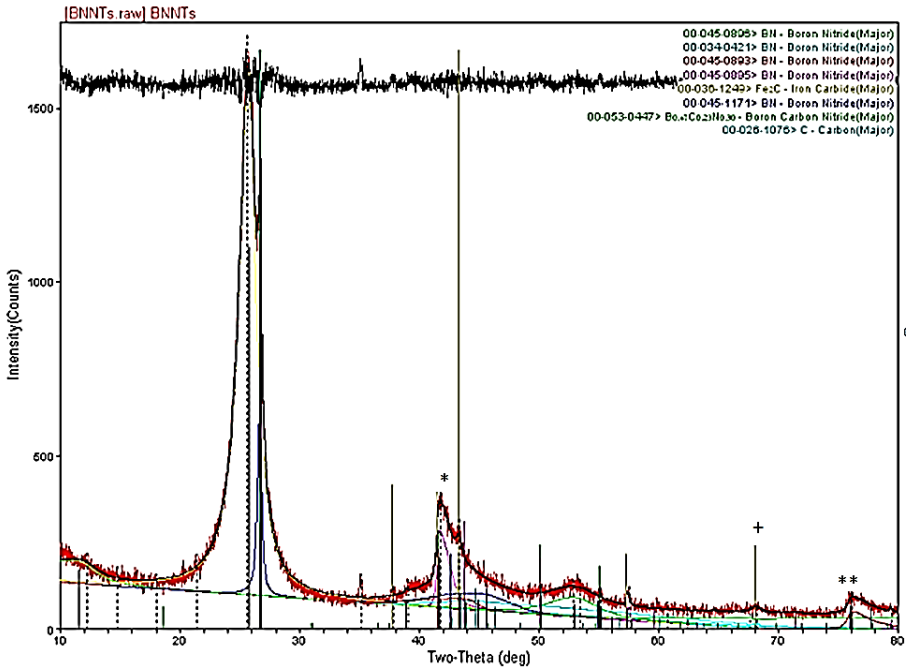

*Figure 4.33: XRD pattern of BNNT showing major peaks as BN and smaller peaks of impurities including * BN contaminated with carbon, + Fe_3C and ** carbon.*

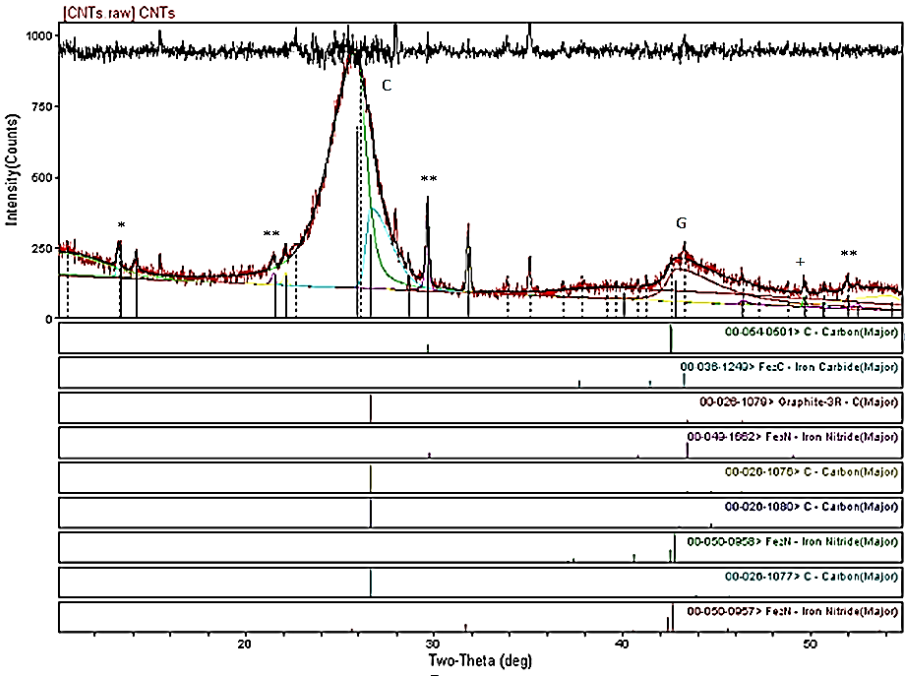

*Figure 4.34: XRD pattern of pristine CNT indicating C as the Carbon (CNT); G as the graphite; and *, **, and + as Fe_2C, Fe_3N and Fe_2N, respectively.*

Figures 4.35 and 4.36 are Raman spectra on BNNT and CNT, respectively. The Raman spectra were obtained using a wavelength of 514 nm (Renishaw inVia Reflex Raman microscope). The dominant feature on the BNNT spectra is the main peak at 1369 cm^{-1}, which is known to correspond to a E_{2g} vibration mode of the sp^2-hybridized BN network. The full width half maximum (FWHM) of the dominant peak is small, indicating that the as-received BNNT sample possesses high-crystallinity.

The CNT spectra in Figure 4.36 shows that the strong Raman active mode called the disordered induced phonon mode (D-band) is at 1350 cm^{-1} and the tangential mode (G-band) is at 1582 cm^{-1}. The ratio of G-band intensity (I_G) over D-band intensity (I_D) is widely used to compare the structural quality of the different CNT materials; a lower I_D/I_G ratio implies a higher degree of crystallization of a sample and a lower amorphous carbon content. Accordingly, the I_D/I_G ratio of 1.12, determined in this study, is lower than literature values in the range of 0.78 to 1.23 [175] indication the presence of structural defects in the investigated CNTs Furthermore, the D-band, which is the highest peak, is the disordered residual ill-organised graphite, and suggests the presence of amorphous or defective carbon impurities. The D' band is an overtone of disorder and is found at 2696 cm^{-1}. The T+D, D^+ and D+G bands are found at 2943, 1462 $cm^{-1}$and 2943 cm^{-1}, respectively.

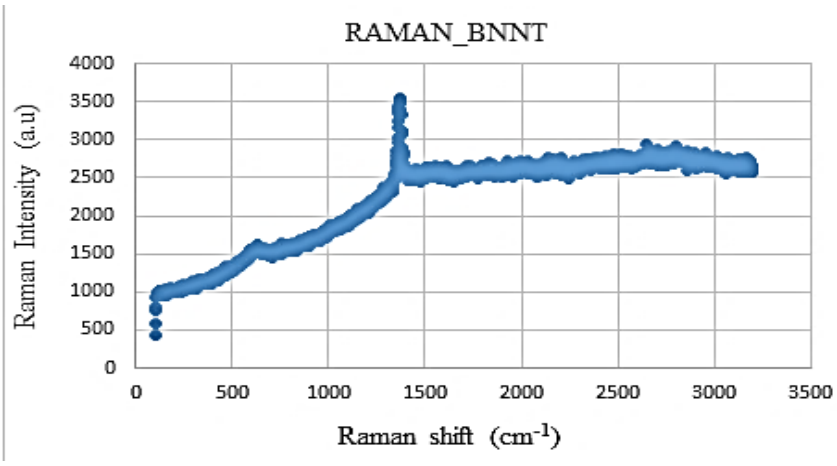

Figure 4.35: Raman spectra on pristine BNNT.

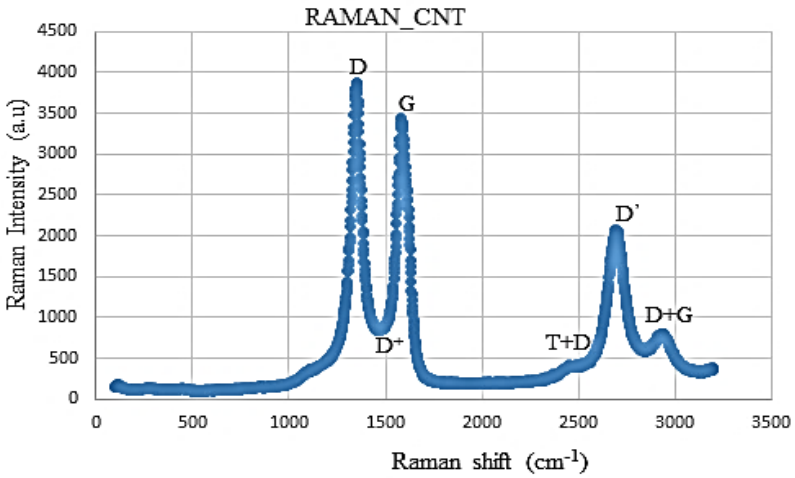

Figure 4.36: Raman spectra on pristine CNT.

4.2.3 Thermal Stability

The effect of direct heating on the morphology of the nanotubes in air and argon environment is shown in Figures 4.37 to 4.40. BNNT was thermally stable (Fig. 4.37) and maintained its structure up to 1400^{o}C in argon and up to 1100^{o}C in air, which was the test limitation due to the oxidation of the used crucible. In contrast, CNT was stable only up to 400^{o}C in air as revealed in Figures 4.38 a. Loss of structural integrity of CNT started at 450^{o}C (Fig. 4.38b) and was completed at 500^{o}C (Fig. 4.38c). The loss of the integrity was

accompanied by a loss in mass as shown in Figures 4.39. CNT also recorded a similar loss of structural integrity in argon where it was transformed into a bulk solid at a temperature of 1400^{o}C after 4 hours as revealed in Figure 4.40.

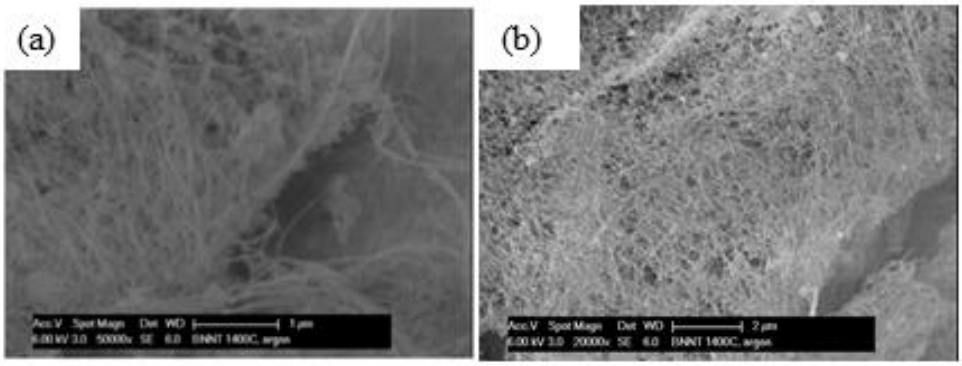

Figure 4.37: SEM image of BNNT at (a) 1100^{o}C in air and (b) at 1400 ^{o}C in argon illustrating its thermal stability.

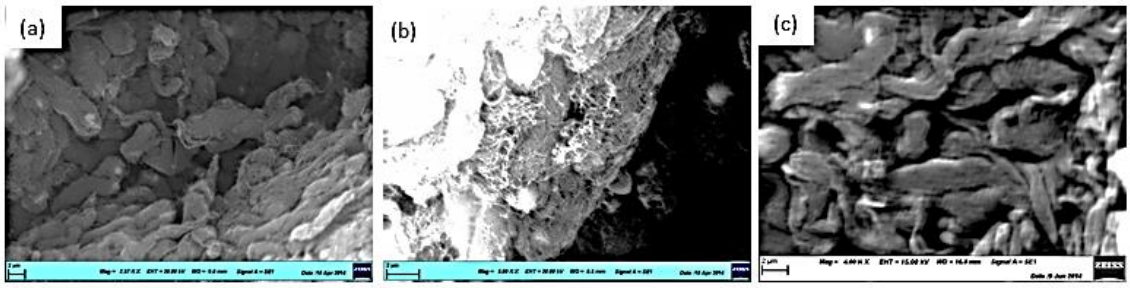

Figure 4.38: SEM image of CNT after heating in air: (a) at 400 ^{o}C ;(b) at 450^{o}C; and (c) at 500^{o}C.

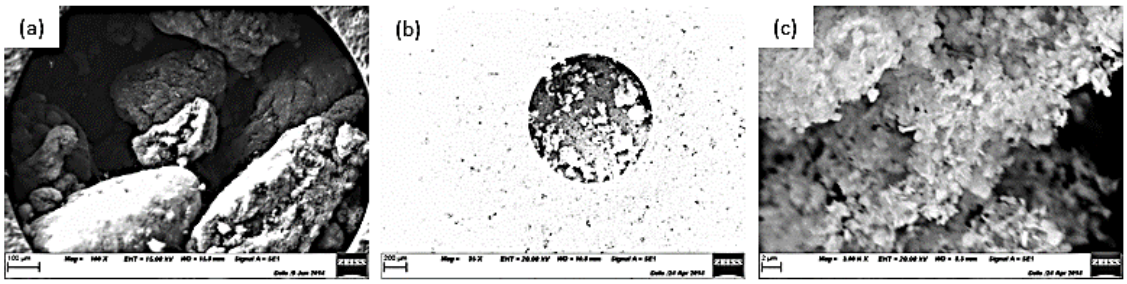

Figure 4.39: SEM images showing CNT in a crucible after heating in air:(a) mass subject to heating; (b) CNT after 500^{o}C heating with loss of mass as compared to (a); and (c) complete loss of original CNT structure at 500^{o}C.

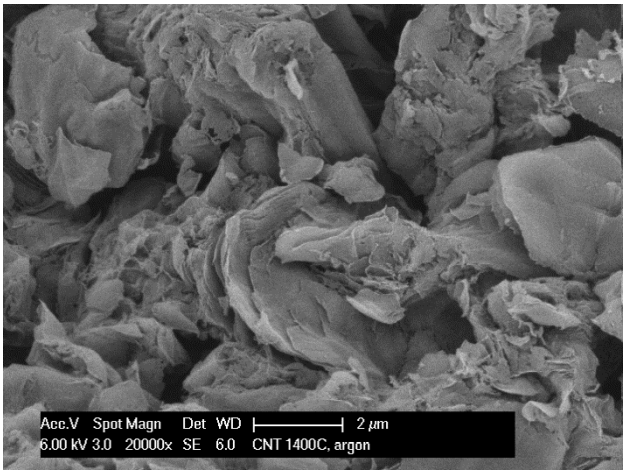

Figure 4.40: SEM image of CNT after 4 hours in argon environment at 1400^{o}C.

The results of the thermogravimetric analysis (TGA) curve showing the samples' weight changes as a function of heating temperature in air are shown in Figure 4.41. This Figure revealed that the mass of BNNT is stable up to 700^{o}C, but increases thereafter to reach a 2.02% mass gain at 950^{o}C. This is due to oxidation of impurities such as residual boron or to oxidation of small-diameter BNNTs which have higher reactivity compared to bulk h-BN. In contrast, CNT started to lose mass at 450^{o}C, which corroborated the direct heating results (Fig. 4.39). The mass loss of CNT continued with increasing temperature to reach 89% at 650^{o}C due to oxidation. The residual mass of around 11% is mainly made of the metal catalysts. Thus, BNNTs exhibits higher thermal stability than CNT.

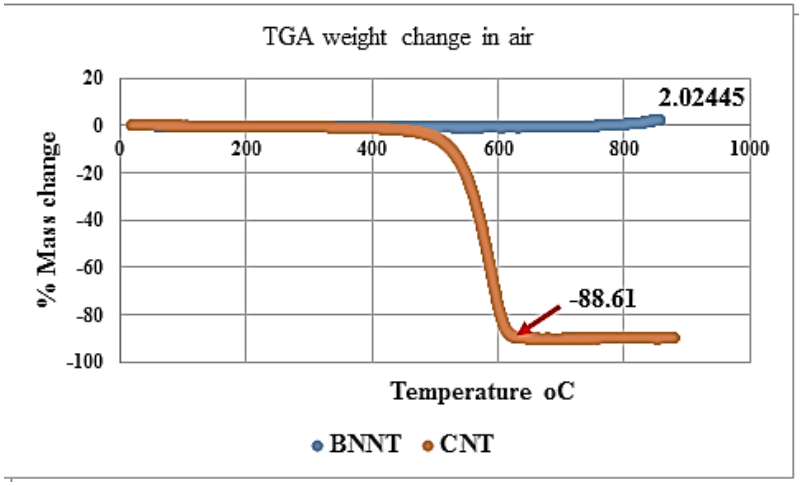

Figure 4.41: TGA results on the nanotubes showing superior stability of BNNT relative to CNT.

4.2.4 Wettability

The water contact angle (CA) measured on prepared BNNT and CNT forest varied from 77 to 84^{o} and 114 to 122^{o}, respectively. Average angles were 80^{o} and 118^{o}, respectively. The optical images of one of the water droplets in advancing mode are shown in Figures 4.42 a and b, on BNNT and CNT, respectively. These angles indicate that the BNNT is weakly hydrophilic, while the CNT is hydrophobic.

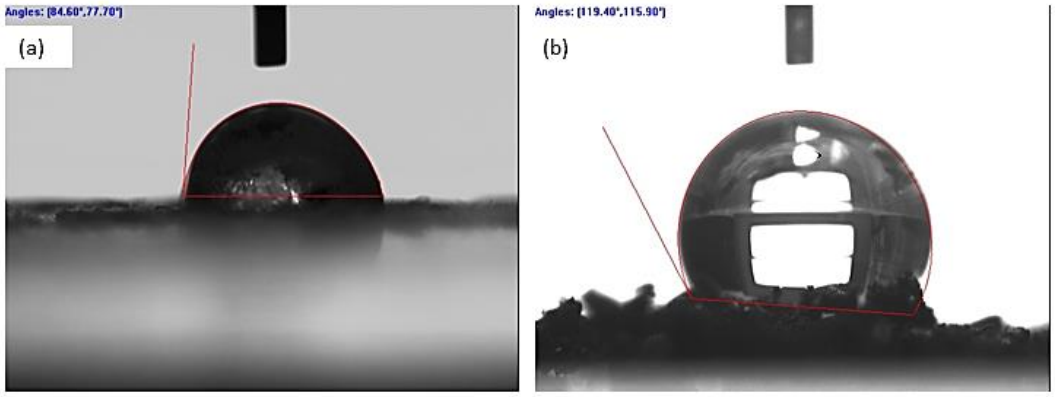

Figure 4.42: Typical photographs showing water droplets on (a) BNNT and (b) CNT.

4.2.5 Dispersion of the Nanotubes

As received alumina powder is presented in Figure 4.43a. It shows a granule size ranging from 160 to 200 μm with individual alumina particle size mostly in the range of 400 to 500 nm. Few particles had a size of about 800 nm (Fig. 4.43b). Figure 4.44a to d shows hand mixed BNNT and alumina powder prior to milling (a) 0 hour, and after ball milling for (b) 1, (c) 4 and (d) 24 hours. It is evidence that on all these specimens, the globular form of the alumina and the BNNT strands have disappeared. Instead, the BNNT strands seem to have been wrapped into about 10 nm spherical bundles that adhere on the surface of alumina particles. The CNT survives ball milling up to 4 hours as illustrated by arrows pointing to CNT strands in Figures 4.45 b and c. However, no CNT strands were found after milling for 24 hours (Fig. 4.45d). Instead, similar to BNNT, only small particles with sizes around 10 nm were found sticking on alumina particles. Figure 4.46 shows the variation in alumina particle size as a function of milling duration. The particle size gradually decreases during the first 6 hours of milling and remain nearly constant at a plateau value of about 300 nm.

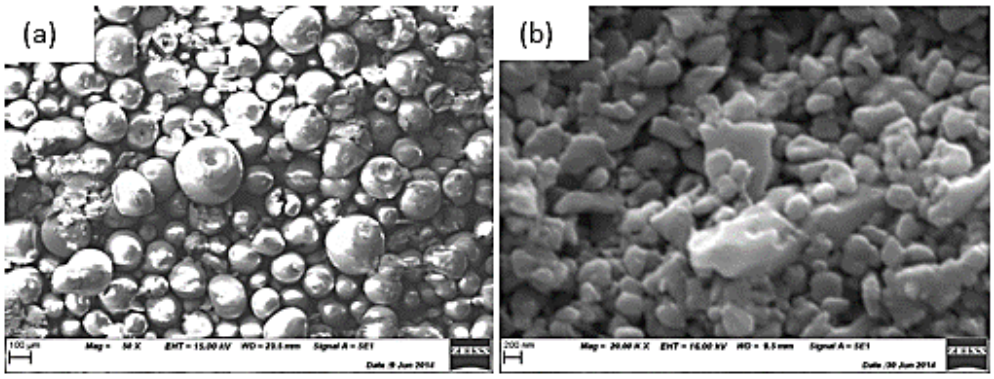

Figure 4.43: SEM images showing alumina powder: (a) alumina in granules form; and (b)expose particles of alumina particles in the granule.

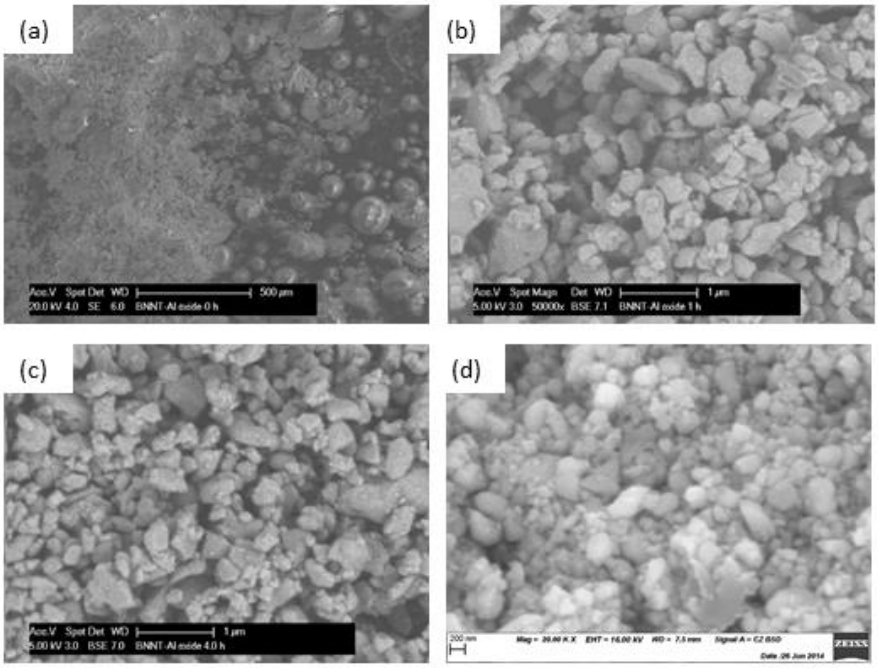

Figure 4.44: SEM images of the BNNT-alumina composite powder. Specimens taken at different milling time: (a) as hand mixed (0 hour); (b) 1hour milling; (c) 4 hours; and (d) 24 hours.

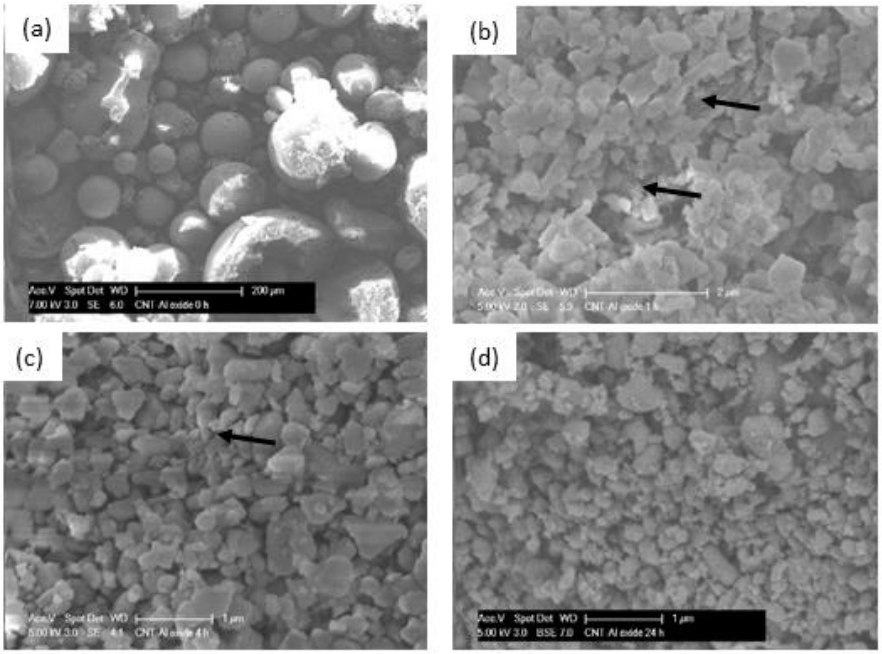

Figure 4.45: SEM images of the CNT-alumina composite powder. Specimens taken at different milling times: (a) as hand mixed (0 hour); (b) 1hour milling with arrows showing CNT strands; (c) 4 hours milling similar to (b); and (d) 24 hours.

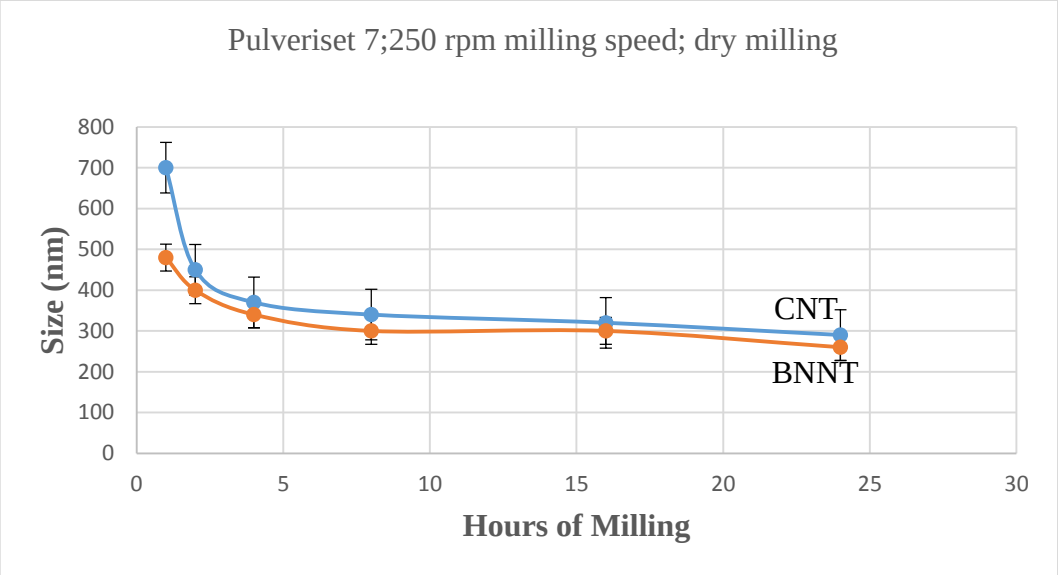

Figure 4.46: Alumina particle size versus milling duration.

.

4.3 DOP

This section presents the results of the ballistic assessment on both monolithic and nanotube reinforced ceramics.

4.3.1 Failure Pattern

The failure pattern of failed ceramics are presented in Figures 4.47 and 4.48. All tested ceramics revealed similar failure patterns consisting of radial and circular or pine cone shape cracks [176]. However, the number and size of ceramics' fragments differed between the ceramics. Overall, the fragment size was larger in alumina, but finer and sharper in SiC and B_4C. At the centre of the shattered ceramics was fine powder (comminuted area) at the front impact size with the back side of the perforated area (hole) about four times as large as the entry point.

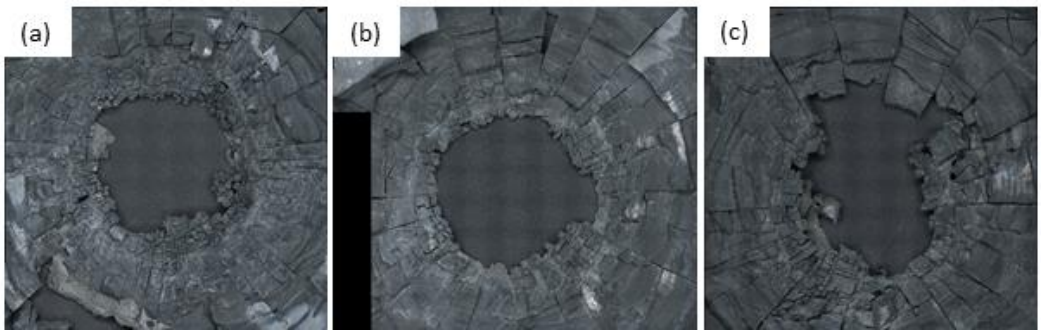

Figure 4.47: Optical micrographs of failed ceramics still attached to the adhesive foil showing the failure pattern: (a) Al_2O_3; (b) Al_2O_3-BNNT; and (c) Al_2O_3-CNT.

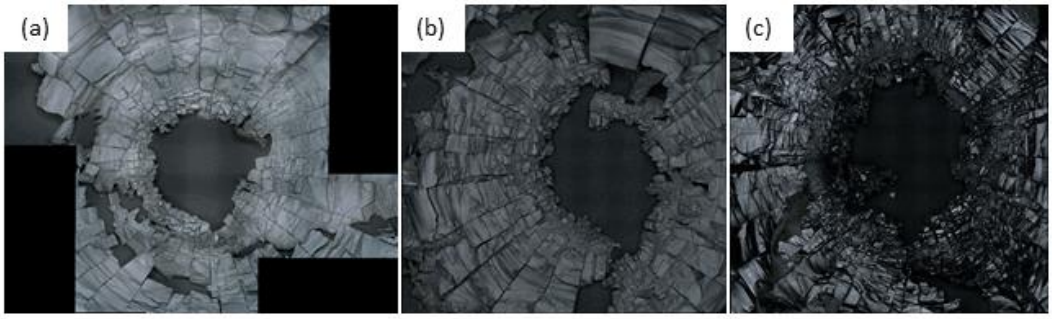

Figure 4.48: Optical micrographs of failed ceramics still attached to the adhesive foil showing the failure pattern: (a) SiC; (b) SiC-BNNT; and (c) B_4C.

Presented on Table 4.10 are the results of the depth of penetration (DOP). The results revealed that the reinforced ceramics SiC-BNNT, Al_2O_3-BNNT and Al_2O_3-CNT showed greater variability in DOP than the monolithic ceramics.

Table 4.10: Summary of depth of penetration test results.

Materials	Average DOP (mm). In bracket is the number of tests	Standard deviation (mm)	Range of DOP value
Al_2O_3	53.67 (3)	1.15	53-55
Al_2O_3+BNNT	59.17 (6)	9.22	48-68
Al_2O_3+SWCNT	56.67 (6)	9.11	46-70
SiC	52.33 (3)	5.86	50-59
SiC + BNNT	93.50 (6)	20.20	82-120
B_4C	61.33 (3)	5.13	57-67

4.3.2 Microstructure

Polished surfaces of the failed ceramics are presented in Figures 4.49 showing the porosity in Al_2O_3, Al_2O_3-BNNT, and Al_2O_3-CNT. It can be observed that both reinforced alumina composites have higher porosity than monolithic alumina. The pore volume fractions are 3.3, 6.8, and 6.3%, for Al_2O_3, Al_2O_3-BNNT, and Al_2O_3-CNT, respectively. Similarly, Figures 4.50 show the structures of SiC and SiC-BNNT, illustrating the over 6.5 times higher porosity of SiC-BNNT compared to monolithic SiC, with both materials containing 0.9 and 6.5% average porosity, respectively.

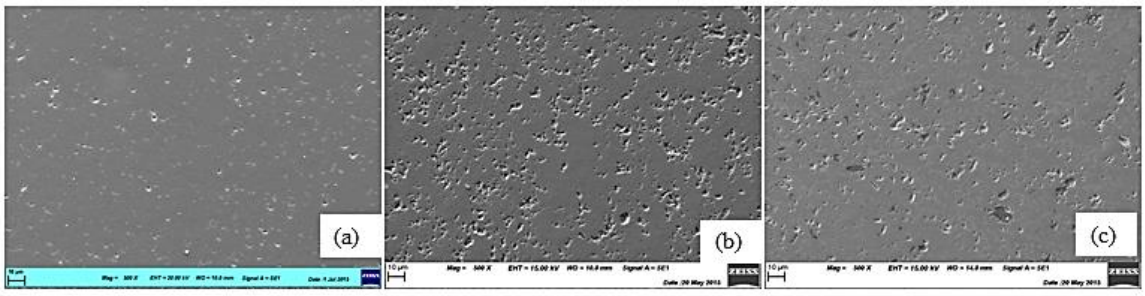

Figure 4.49: SEM images of the alumina ceramics group showing relative porosity levels in the monolithic and the reinforced alumina: (a) Al_2O_3; (b) Al_2O_3-BNNT; and (c) Al_2O_3-CNT.

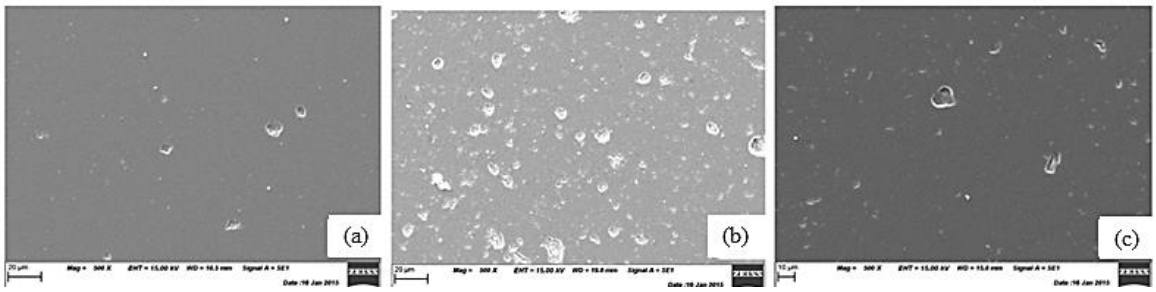

Figure 4.50: SEM images of the polished surfaces: (a) SiC; (b) SiC-BNNT; and (c) B_4C, showing relative pore distribution in the three ceramics.

Figures 4.51 shows nanotube agglomerates as preferred pore locations with sizes as large as 44 µm. Overall, nanotubes increase both the pore size and the pore volume fraction. Figure 4.52 shows that the average pore sizes of all the armour ceramics are within 4 to 6 µm

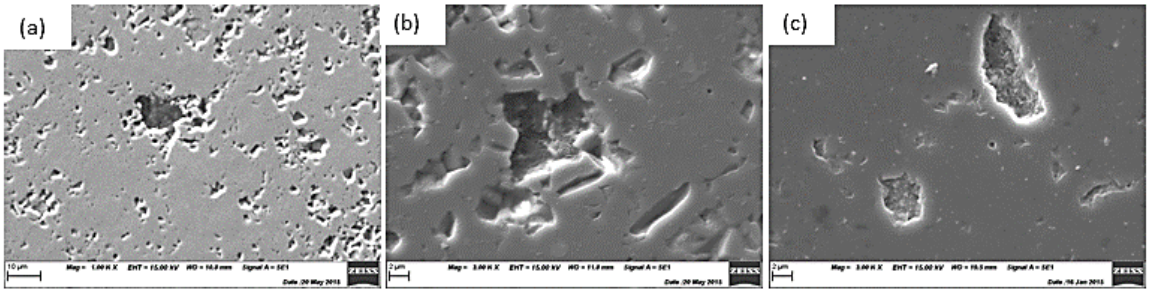

Figure 4.51: SEM images of polished specimens showing pores at nanotubes agglomerated: (a) Al_2O_3-BNNT; (b) Al_2O_3-CNT; and (c) SiC-BNNT.

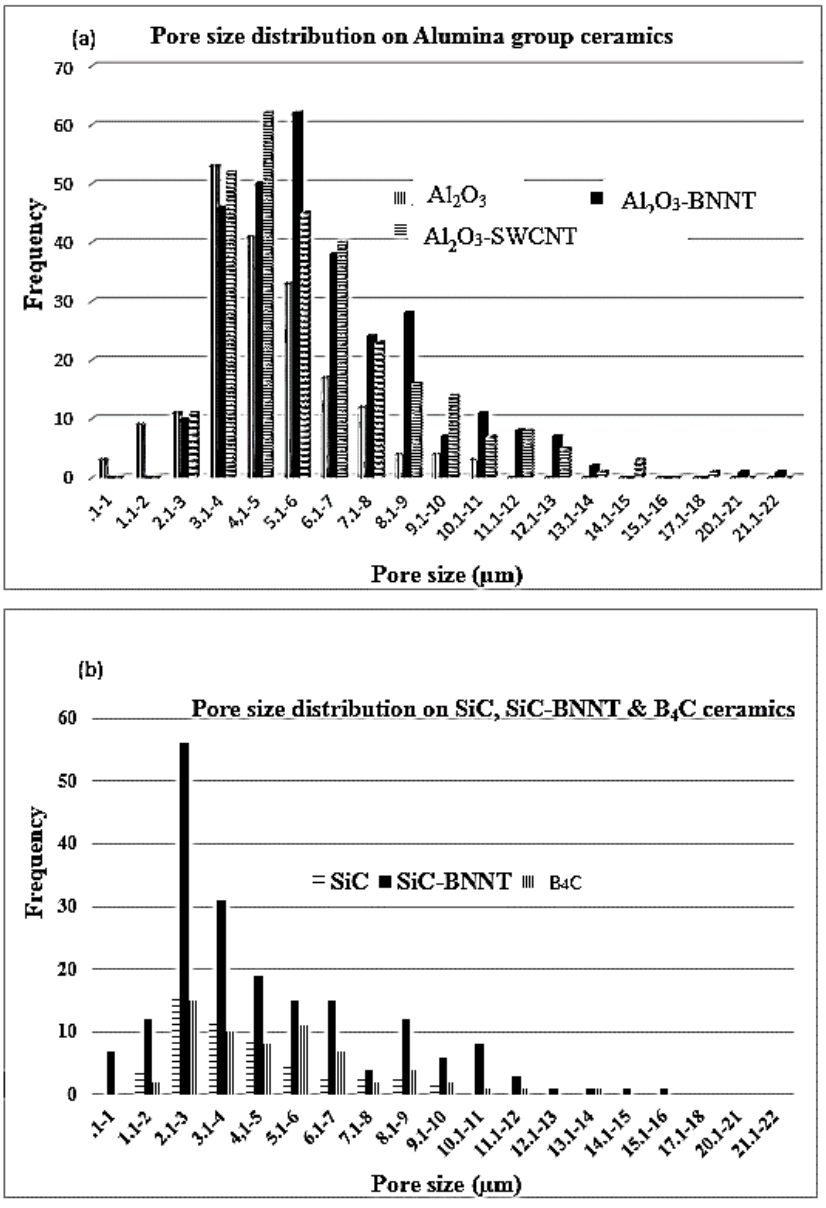

Figure 4.52: Porosity analysis on the materials: (a) alumina ceramics group; and (b) SiC, SiC-BNNT, B_4C.

4.3.3 Fractography of Materials after Ballistic Impact

4.3.3.1 Grain Size

The grain sizes of all materials tested for ballistic penetration fall within 1 and 6 µm, with average grain sizes in the range of 2 to 3 µm as can be seen in Figures 4.53 and 4.54

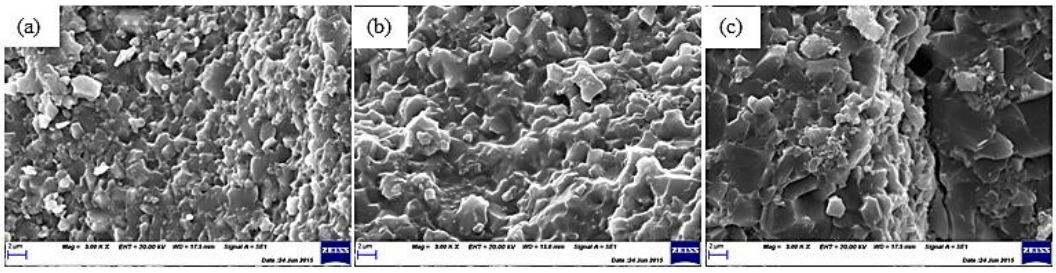

Figure 4.53: SEM images of fractured surface showing the grain structures used for grain sizes analysis: (a) Al_2O_3; (b) Al_2O_3-BNNT; and (c) Al_2O_3-CNT.

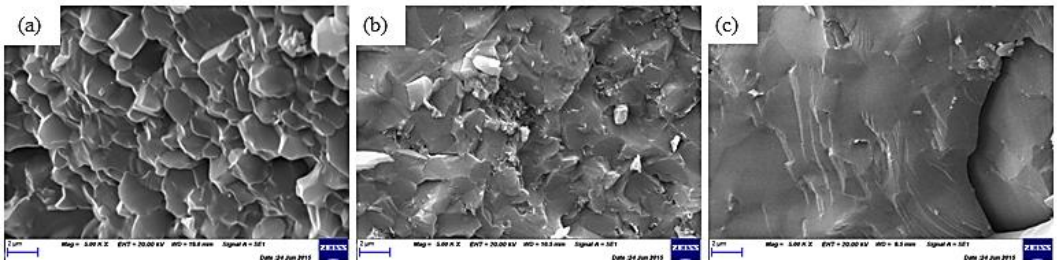

Figure 4.54: SEM images of fractured ceramics surfaces showing the grain structures: (a) SiC; (b) SiC-BNNT and ; (c) B_4C

.

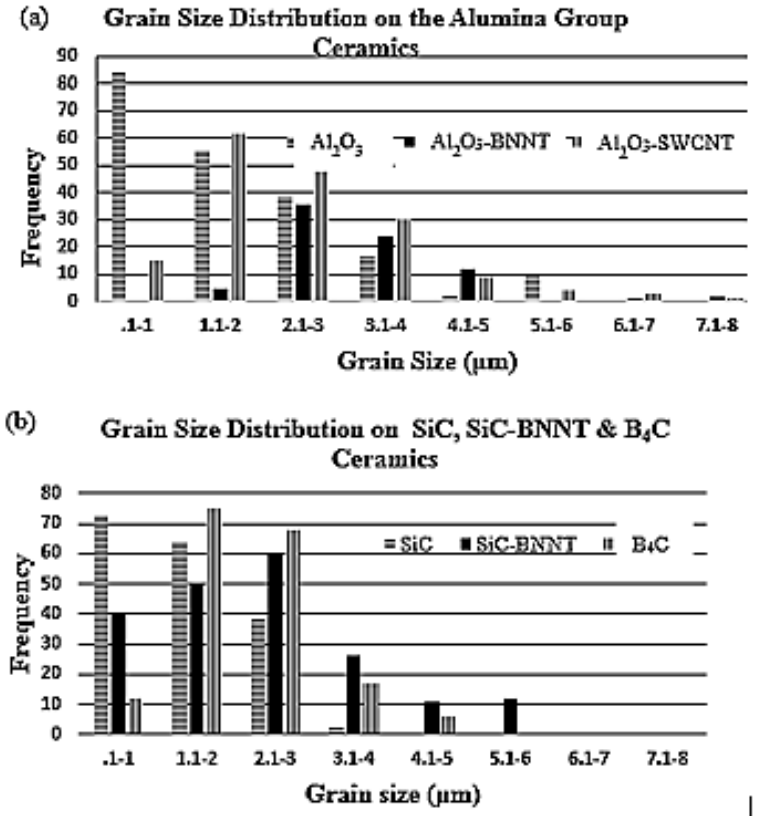

Figure 4.55: Grain size analysis on the materials: (a) alumina ceramics group; and (b) SiC, SiC-BNNT and B_4C.

4.3.3.2 Second Phase Agglomeration

Figure 4.56 shows the monolithic materials revealing a fairly homogeneous microstructure. In contrast, Figures 4.57 to 4.59 show areas of good dispersions as well as regions with nanotube agglomerations, primarily in the SiC-BNNT composite. The agglomerations contributed to the variability of the observed DOP results [41].

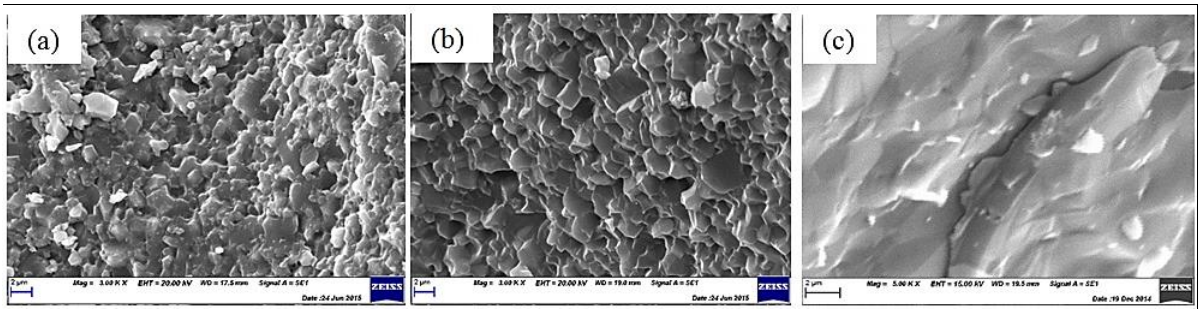

Figure 4.56: SEM images of fractured surfaces of the monolithic materials: (a) Al_2O_3; (b) SiC; and (c) B_4C.

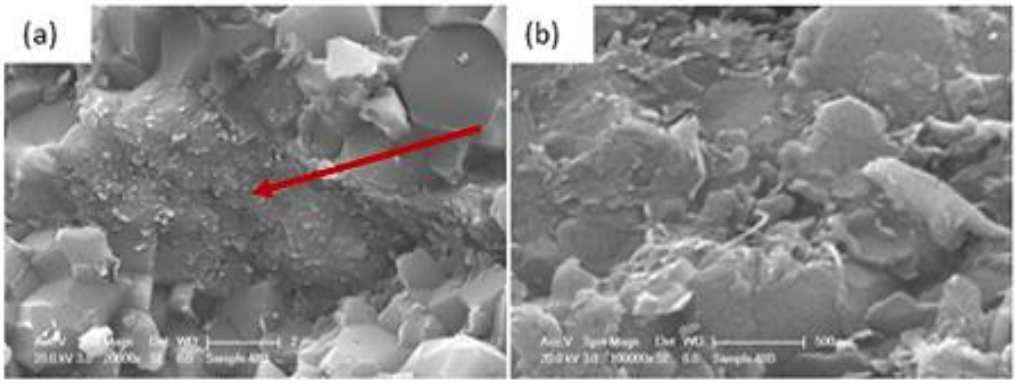

Figure 4.57: SEM images of fractured surfaces of the Al_2O_3-BNNT: (a) agglomerated nanotubes mainly in the form of flakes (arrow); (b) well-dispersed nanotubes.

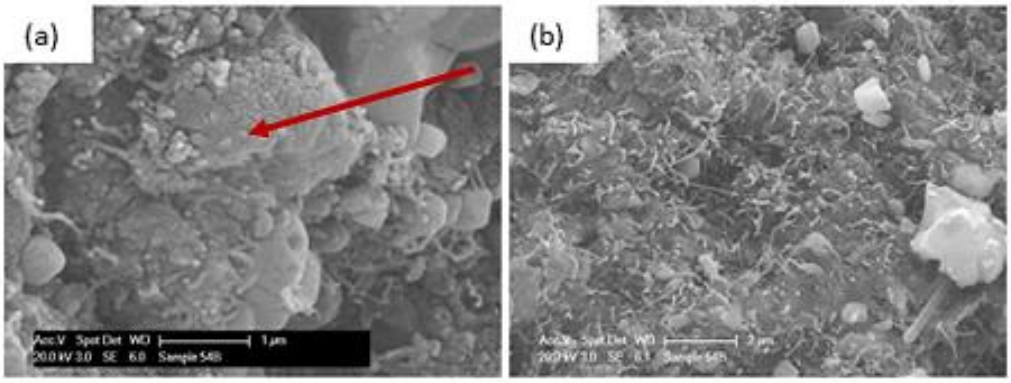

Figure 4.58: SEM images of fractured surfaces of the Al_2O_3-SWCNT: (a) agglomerated nanotubes (arrow); (b) well-dispersed nanotubes.

Figure 4.59: SEM images of fractured surfaces of the SiC-BNNT: (a) agglomerated nanotubes accompanied with flashes of short-length nanotubes (arrows) at grain boundaries; (b) agglomerated nanotubes in the form of destroyed and unbounded BNNT; and (c) high magnification of agglomerated nanotubes at grain boundaries of the SiC matrix shown by the arrow.

4.3.3.3 Failure Mode

Presented in Figures 4.60 and 4.61 are SEM images of failed specimens revealing the mode of failure as presented in Table 4.11.

Table 4.11: Fracture mode of the ceramics.

Material	**Al_2O_3**	**Al_2O_3-BNNT**	**Al_2O_3-CNT**	**SiC**	**SiC-BNNT**	**B_4C**
Fracture mode	Mostly IG	IG + TG	IG + TG	IG + TG	Mostly TG	Mostly TG

IG – Intergranular, TG – Transgranular

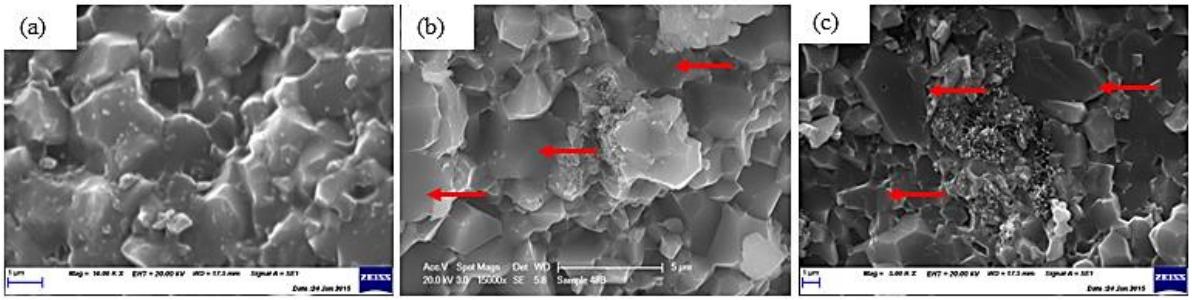

Figure 4.60: SEM images of fractured specimens revealing the mode of failure showing predominantly transgranular failure as illustrated by arrows: (a) Al_2O_3; (b) Al_2O_3-BNNT; and (c) Al_2O_3-SWCNT.

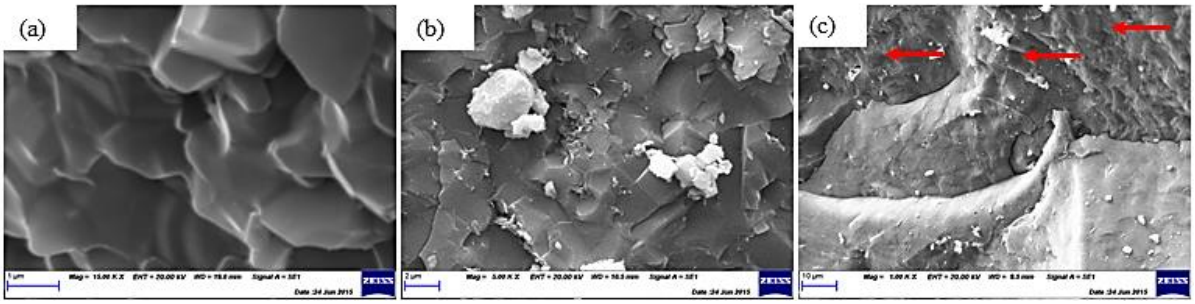

Figure 4.61: SEM images of fractured specimens revealing the mode of failure showing predominantly transgranular failure as illustrated by arrows: (a) SiC; (b) SiC-BNNT; and (c) B_4C.

CHAPTER 5

DISCUSSION

5.1 Microstructural Features

This section discusses the microstructural attributes of the commercial ceramics, ZTA and SiC. The voids at the front impact face of ZTA can be assumed to be designed to enhance the interface defeat capacity in this material [95], and to improve its ballistic performance through projectile deflection. The voids also contribute to the control of the fragment size of the failed material during the penetration stage of the projectile, which assists in improving the fragment erosion [18, 106]. Also in ZTA, the ZrO_2 second phase particles are known to improve the fracture toughness [177, 178]. In addition to the alumina matrix and ZrO_2 particles, there is a balance of 1.5% compounds containing, among others, the element Niobium (Nb). Nb is often used to partially stabilize ZrO_2 [179], and helps ZrO_2 to retain its tetragonal (t) phase at room temperature. This stabilizing concept is the key to achieving the desired toughening effect. Traces of Pt and Ag were also detected during SEM - EDS analysis. These traces may be impurities in the starting powder (or residues of process additives).

The microstructure of SiC is typical for solid-state pressureless sintered ceramic. It consists primarily of 3 phases: hexagonal α-SiC matrix, Ce-Pd-Sn $(Ti_{0.33}V_{0.6}Mn_{0.07})D_{1.28}$ and deuterides precipitates. The Ce-Pd-Sn phase accounts for about 5% volume and is uncommon in SiC ceramic. However, there are literature indications that it can be used as an additive to tailor the grain size, and improve densification and toughness [74]. It is well known that using a combination of additives can be effective for optimizing the microstructure and, consequently, the mechanical properties of the materials [68, 180]. The Ce-Pd-Sn system can also be used to control the level of free carbon that can be detrimental to SiC [181].

The Ti-V-Mn deuteride phase, with 2.28% volume fraction, is most likely either impurities in the raw material (similar to other elements such as Sn and I) or a reaction product due to the sintering environment, which can be hydrogen rich. Some remaining un-reacted carbon was also detected, which usually gives the black colouration to the material [182].

The grain size, shape and distributions are dependent on the selection of additives and are reported to control mechanical properties [183]. The grain size of the initial powder determines the final material grain size. In ZTA, the grain size is bimodal. The use of zirconia as a secondary phase prevents grain growth [96], but may also impede densification during processing as reflected by the high porosity level. In SiC, an elongated grain shape is prominent, which may be due to the use of Ce additives, since rare metals such as Ce promote grain elongation. High grain aspect ratios of approximately 3 to 5 can enhance material properties [74]. Similar to ZTA, grain growth or recrystallization in SiC appears impeded by additives used to pin grain boundaries. Grain boundary pinning was observed in SEM images, showing discontinuous phases located at grain boundaries.

Defects in both ceramics include: porosity, inclusions, density gradients, additive residues, non-uniform additive distribution and large grain regions. In ZTA, inclusions account for less than 1.5% volume fraction. Through ultrasonic testing, a non-uniform distribution of pores was revealed, leading to what appears to be marked density gradients. The porosity is the greatest challenge in ZTA, resulting in only 90.3% relative density. This suggests poor sintering ability of this material [96]. The high porosity level of ZTA is demonstrated by its transparency to light. In SiC, the pressureless sintering method and elongated grain morphology are the major factors for the remaining porosity. The inclusion percentage is approximately 1.4 vol %, and the porosity is 2.4 vol %, leading to a relative

density of approximately 98%. Residues of sintering additives also promote porosity in SiC [182]. The pores are less than 1 μm in size as measured using SEM. The observed sintering additive residues are in conformity with a previous study [184]. SEM-EDS investigation also showed the presence of Fe, Si, C, O and Ni. The presence of oxygen as an impurity suggests that sintering additives are primarily oxides, while Fe is most likely a residue of the Fe/Cr/Ni/O compound, which is a common SiC processing aid and impurity. Other uncommon defects in SiC are reaction products of sintering additives, raw material impurities and sintering atmosphere including titanium, manganese and vanadium which create deuterides.

5.2 Armour Related Properties

Armour related properties on commercial ceramics, ZTA and SiC, are discussed under this section. The properties include hardness, fracture toughness, strength (static and dynamic), Young's modulus, porosity (density) and fracture mode.

5.2.1 Hardness

Both ZTA and SiC exhibit indentation size effects (ISE) up to an indentation load of 2 kgf. The origin of ISE in ZTA is traceable to three factors: elastic recovery after bulk material indentation (Fig. 4.13), indenter/specimen friction coupled with the elastic/plastic deformation response of the material, and the high concentration of voids [96]. In SiC, the origin of ISE is traceable to frictional forces, a load dependent material response to deformation, which includes dislocation activity and cracking [10], as seen in Figure 4.14. Overall, it can be concluded that the indent interaction with pores/flaws can considerably change the expected hardness results at low loads.

The theoretical hardness expected for ZTA, according to the rule of mixture of Al_2O_3 and ZrO_2, is 16-17 GPa, whereas the measured true hardness is 14.89 GPa. This translates into

approximately a 10% drop from the theoretical value. Potential causes of this drop are: (1) the average grain size of 5 μm, which is larger than reported in literature [24], and (2) the porosity in agreement with literature [96]. In summary, the wide distribution of hardness values can be attributed to the variation in porosity, grain structure and ZrO_2 particle structure.

The evaluated hardness of 23.9 GPa (2413Hv) for SiC is on the lower range of literature hardness values of monolithic SiC processed using the same method [69], which is between 2100-2800 HV (20.72-27.63 GPa). This relatively low hardness of SiC can be explained by: (1) the non-homogeneity primarily caused by sintering additive residues; (2) the substantial amount of inclusions accounting for about 1.5 wt.%; and (3) a relatively large grain size of 5 μm. For example, the highest hardness of 27GPa was recorded with a 0.5 to 1.20 μm mean grain size and various grain aspect ratios [68].

5.2.2 Fracture Toughness

SiC started forming cracks at a lower load of 3 N, which is in agreement with the study of Yang [185], whereas visible cracks started at 10 kg load on ZTA. The plots of c, a, and c/a versus load are presented in Figures 5.1 and 5.2 for ZTA and SiC, respectively.

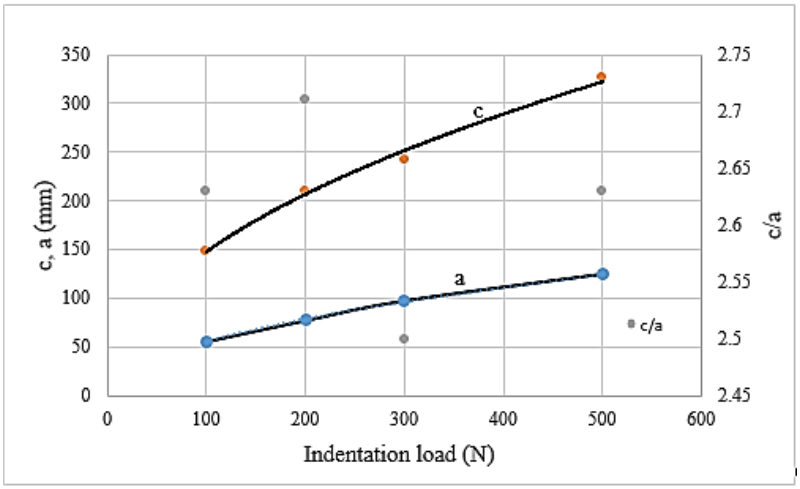

Figure 5.1: Indentation and crack dimensions in ZTA ceramics at different indentation loads.

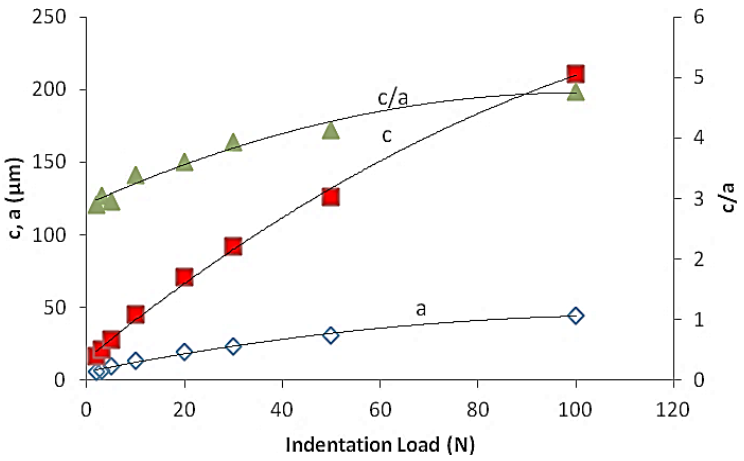

Figure 5.2: Indentation and crack dimensions in SiC at different indentation loads.

The values of c/a ratio obtained on both materials are within the median crack regime. The c/a ratio of 2.90 determined for SiC in this study is in agreement with the study by Lee [74]. The c/a ratio lies between 2.50 and 2.71 for ZTA, which is also in the median crack regime just above the transition. As expected, the two semi-empirical fracture toughness equations by Lawn et al. and Nihara et al. for ZTA and SiC, respectively, yield toughness values in agreement with literature [54, 74].

The $c^{3/2}$ versus indentation load plots are presented in Figure 5.3 and indicate a good linear dependence in agreement with previous work [74], which validates the testing results.

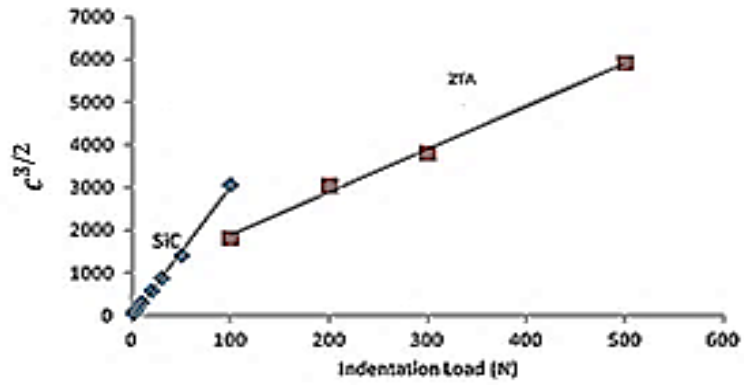

Figure 5.3: Relationship between crack length c and indentation load for SiC and ZTA.

The measured fracture toughness of SiC is 2.98 MPa√m. Comparing with literature values that range between 2.6 and 2.8 MPa√m [105], this represents an improvement of 6.4 to 14.6% for this material. The results also corroborate the recommendation test load of 3 N by Yang [185].

The experimental K_{IC} value of 4.90 MPa√m found for ZTA is in agreement with the study of Ganesh [75] where 0-20 vol. % ZrO_2 was used in the alumina matrix. Comparing this value to monolithic alumina with a toughness of about 2.69 MPa√m [186], this material showed an increase by 82.2% in fracture toughness.

The appearance of cracks during indentation is known to be a function of anisotropy, particle size, environment and residual stress, which can affect the results of the K_{IC} measurement. Residual stresses may also be created during indentation, which can accelerate crack growth, leading to an under-estimation of the materials toughness [69]. However, the radial crack length $c^{3/2}$ remains a linear function of applied load in this study.

Visible cracks were formed on both materials, which is confirmed by the fact that the values for c are greater than 2a [185]. In addition, SiC showed heavy chipping, primarily caused by the anisotrophy and the presence of second phases. Chipping is an indication of lateral pores intersecting the surface of the indent and obstructing the crack path [187].

The toughening mechanism by ZrO_2 is predominantly governed by its particle size. In this study, three toughening mechanisms are found to account for the K_{IC} increase. Firstly, the stress-induced tetragonal-to-monoclinic phase transformation when the size of ZrO_2 particles is predominantly below 1 μm [188], which leads to a volume increase of around 4%. This volume increase has the tendency to close growing cracks, leading to an increase in K_{IC}. Secondly, the grain size of the alumina (5-10 μm) contributes to intergranular crack

propagation, leading to longer crack paths and consequently higher energy absorption. And thirdly, the loading leads to pore collapse and densification, which can absorb a substantial amount of energy and retard crack initiation and growth.

In SiC, second phases are absent at grain boundaries, although some phases were identified apart from α-SiC. The presence of cerium is designed to influence fracture toughness [182]. The key contributing factor to the K_{IC} increase in SiC is the large grain aspect ratio close to 3 [74]. This relatively large grain aspect ratio favours crack deflection.

5.2.3 Static Strength

Research so far has primarily focused on the use of uniaxial testing methods (3 or 4 point bend tests) rather than on biaxial testing, which can provide more information on the state of stress, comparable to the real ballistic event. In this study, the strength measurement using equi-biaxial Ring-on-Ring (RoR) test gave 184.4 and 182.9 MPa, and those of the uniaxial 4 point bend test were 292 and 242 MPa for ZTA and SiC, respectively. This corresponds to 58.4% and 32.3% higher strength in the 4 point bend tests, for ZTA and SiC, respectively, compared to RoR tests. This is in agreement with literature [59, 189] and reflects the higher material volume involved in RoR tests. For instance, 40-80% higher strength values were measured for Si_3N_4 using uniaxial tests compared to equi-biaxial tests [60]. The large discrepancy can be expected because of intrinsic flaws including non-uniform distribution of pores in ZTA and inclusions in SiC [68, 96]. The RoR strength values for the two materials, however, may also have been under-estimated because of sub-critical crack growth.

Comparing the results on ZTA with literature strength values equal to or higher than 350 MPa on alumina [190], a 16.6% drop in uniaxial strength is observed in this study. For SiC with a 326 MPa strength value [68], a drop of 25.2% in uniaxial strength is observed. The

strength of ceramic materials is known to be primarily governed by flaws [61]. Therefore, the Griffith mechanics theory of fracture given by equation 2.2 can be used to quantify the strength. In this equation, the key independent factor is the critical size of flaws, which is referred to as failure-causing crack (FC). This study attempted to adopt the equation to simulate the FC. The simulation yielded FC lengths of 173 μm and 92 μm for ZTA and SiC, respectively, which are associated with a flaw geometry of 1. These sizes seem reasonable considering the coalescence of cracks before failure.

Microstructural heterogeneities in SiC arise from sintering additive residues and may affect its strength. The two inclusion phases in this material are homogeneously distributed within the SiC matrix, still, they are likely to also lower strength due to their lower hardness. In fact, the deuteride phase is most likely to be detrimental to material property, as illustrated in Figure 4.7, where blistering can be seen after vacuum etching.

In ZTA, ZrO_2 poses a serious challenge with respect to sinterability [96], leading to the relatively high porosity of 9.7 volume%. Understandably, the higher critical crack size of 173 μm is achieved by coalescence of initial pores that were measured to have sizes as high as 20 μm. The high porosity seems to be balanced by the presence of zirconia particles at grain boundaries, that leads to a strength increase [191] and to crack deviation resulting in higher energy absorption and toughness.

5.2.4 Dynamic Strength

In this study, Charpy testing gave impact toughness values of 0.34 J and 0.21 J for ZTA and SiC, respectively, which translates into SiC having only 61.8% of the toughness of ZTA. This ratio is in agreement with the indentation fracture toughness values of these materials, which are 2.98 $MPam^{1/2}$ and 4.90 $MPam^{1/2}$ for SiC and ZTA, respectively. Drop

tower tests (DTT) were also successful in assessing the damage behaviour of SiC and ZTA, and for determining the fracture energy, the crack density, the fracture mode and the crack velocity [57]. DTT confirmed that SiC shows lower toughness compared to ZTA, which is in agreement with indentation fracture toughness and RoR tests as seen in Table 4.5. The total rate of energy release is found to be higher for SiC than ZTA. This agrees with the crack behaviour observed on SiC that showed heavily fragmented failed samples and advanced pulverisation. In contrast, the strike surface of ZTA samples exhibited higher rate of energy release than the back surface, yielding less crack propagation on the back surface than on the strike surface. This implies better ballistic protection. Also, SiC failed at a drop height of 30 mm, while ZTA did not fail until heights greater than 40 mm. This is reflected by strong crack branching (Fig. 4.20c) with the rate of surface energy being much higher than in the case of a single crack.

5.2.5 Young's Modulus

For ZTA, the main microstructure features are the zirconia particles and porosity. Therefore, the Young modulus is evaluated using these two factors. First, the rule of mixture is used to obtain 330 GPa as the pore-free Young modulus. Equation 2.1 is then applied to consider porosity, and then using equation 2.3, which gives a Young,s modulus of 272 GPa. This translates into 82.4% relative Young's modulus for this material.

The semi-empirical equation 5.1 proposed by Spriggs [192] and adopted by Deng [73] is also used to simulate the compactness in ZTA by solving for the parameter b.

$$\mathbf{E} = \boldsymbol{E_O}\mathbf{exp}(-\mathbf{bp}) \tag{5.1}$$

Where E_o is the modulus of the fully dense ZTA, p is the pore volume fraction and b is a characteristic constant which is related to the particle stacking and pore shape, and usually has

values that range between 1 and 4.35 [73]; b was evaluated to be 2 based on equation 5.1. This value is an indication that the pores are not spherical or compact, which is confirmed by Figure 4.10b, showing that the pores often take the shape of the grain boundaries. Young's modulus values of SiC determined by the semi-empirical equation using the porosity [44] and by instrumented indentation data analysis were found to be comparable, and are 389 GPa and 374 GPa, respectively. However, considering that additional factors other than porosity also control microstructural and mechanical properties, a Young's modulus of 374 GPa from instrumented indentation tests was adopted in this study. This value amounts to 91.9% of the theoretical value of 410 GPa [74].

It can therefore be concluded that the level of densification or porosity is the main reason for the drop in ZTA's Young modulus, whereas impurities in raw materials, including sinter additives residues, primarily explain the drop in SiC's Young's modulus.

5.2.6 Porosity

The Archimedes and the porosity methods gave density values of 3.78 g/cm^3 and 3.75 g/cm^3 for ZTA, respectively. The difference is small despite the questionable assumption of the theoretical density for the porosity method. Comparing the estimated density of about 3.78 g/cm^3 to the ZTA theoretical density of 4.15 g/cm^3 as evaluated through the rule of mixture translates into a 8.9% drop in density. Thus, besides the chemical composition, the porosity is one of the basic controlling factors for the density of ZTA [44]. The relatively high porosity in ZTA is a product of the pressureless sintering method and the interaction between grain size and shape of both Al_2O_3 and ZrO_2. In fact, the grain size of alumina is non-homogeneous and ranges between 1 and 10 μm, while ZrO_2 grains are mostly smaller than 1 μm, with occasional particle sizes of about 5 μm diameter. The mismatch between the initial grains of the two

constituents leads to porosity at their interfaces that seems to persist even after sintering into the final product [75].

The Archimedes measurement method yields a density of 3.08 g/cm^3 for SiC, which translate into about 96.14% relative density, using the theoretical density of 3.21 g/cm^3 [74]. This means that the porosity of 2.4% measured in this material is not the only factor that influences its density. Rather, deuterides and Ce-V-Mn inclusion phases also contribute to the lower relative density.

5.2.7 Fracture Mode

Crack propagation in ZTA is predominantly intergranular with the crack path deflection related to the curvature of the grains. Besides the zirconia toughening, the anisotropic microstructure of ZTA is a main factor in the substantial increase of fracture toughness by crack deviation leading to a longer crack path and higher energy absorption at fracture. This result is in agreement with literature findings on ZTA [188]. As the crack propagates in ZTA, stresses around the crack initiate zirconia phase transformation causing tensile stresses in zirconia grains and compressive stresses in the alumina matrix. These two types of stresses are tangent to the particle matrix interface, hindering crack propagation and leading to increased fracture resistance [188]. Additionally, the intergranular mode of failure favours dislocation pile-ups at grain boundaries, thus greater energy is required for crack propagation resulting in higher toughness. In SiC, the crack path through the grains is an indication that the grain strength is lower than the grain boundary strength. This leads to “straight” crack propagation with little to no crack deviation and lower energy absorption at fracture.

5.3 Microstructure Relationship to Ballistic Performance

Microstructural features of ZTA and SiC and the relationship to ballistic performance are considered in this section. It has been proven that ceramics with well-distributed small-sized pores (as observed in ZTA) can exhibit good ballistic performance [23]. The pores are beneficial to the residual strength [35], which is known to enhance ballistic performance and multi-hit capability [25]. Other properties that enhance armour ceramics performance include hardness, Young's modulus, sonic velocity, density and grain size, all of which are in appropriate ranges in ZTA [34].

In the case of SiC, the main microstructure defect is residual sintering additives, which are found to be non-uniformly distributed in the matrix (Fig. 4.4d). This Figure also shows the presence of other impurities. Impurities and inclusions in ceramics have been shown to lead to variability in ballistic performance [19, 22], as they can act as crack initiation points and preferential paths for crack propagation [22]. Moreover, the non-uniform distribution of the residual sintering additives causes variability in hardness and strength as shown in Figure 4.4d [20].

5.4 Armour Property Relationship to Ballistic Performance

The relationship between armour related properties of ZTA and SiC and ballistic performance is considered in this section. According to Swab [24], the simple rule of selecting ceramics for armour applications is that it should be harder than the projectile it intends to defeat. Projectiles are commonly made of steel and Tungsten Carbide (WC) cores, which have hardness values in the range of 600 to 920 HV and 1250 to 1550 HV, respectively [46]. Given the hardness values determined on the investigated ceramics, it can be inferred that SiC is

more than adequate for ballistic performance, while ZTA is strongly adequate for steel cores but just barely adequate for WC projectiles.

While there is no literature benchmark value of K_{IC} for armour ceramic, it is widely accepted that monolithic alumina and SiC ceramics are of appropriate hardness and fracture toughness for armour systems. Literature K_{IC} values for monolithic SiC and alumina-sintered products are in the range of 2.6 – 2.8 and 2.69 – 4.0 $MPam^{1/2}$, respectively. These values are deemed adequate for a one shot assault, assuming all other required properties for armour performance are attained.

It is widely accepted that the ballistic performance of armour ceramic can be improved to meet multi-hit challenges if the fracture toughness is increased considerably. Studies have shown that not only the toughness, but also the strength of the ceramic significantly affects the fragmentation process [4, 96]. ZTA has an average strength value of 292 MPa and a relatively high fracture toughness compared to monolithic alumina or SiC and is considered satisfactory for multi-hit performance [30]. The multi-hit capabilities of ZTA and alumina as a function of improved fracture toughness have been studied through depth of penetration test [30]. The fracture strength of the two materials was measured to be 274 and 272 MPa, respectively. The study concluded that ZTA outperformed alumina because of its greater fracture toughness. Additionally, a numerical study on AD 95 alumina and 10% ZTA showed that the ballistic resistance of ZTA is better than that of AD 95 alumina due to increased K_{IC} [31, 96].

The strength of ZTA may be considered ideal for ballistic performance given its resistance to cracking in both RoR and drop weight tests. The adequacy of this material's strength for ballistic performance, despite its high porosity concentration, is also reported in literature [96]. Moreover, the time to fracture is higher for ZTA when compared to SiC (Table

4.6), which is a further indication of its higher strength. Also, the ability of this material to sustain higher loads during Vickers indentation confirmed its deformation resistance, and thus better ballistic performance is expected. Furthermore, ZTA exhibits essentially a primary crack pattern accompanied by an intergranular mode of failure. In contrast, SiC shows both primary and secondary crack patterns leading to practically crushed specimens. In addition, SiC shows fast crack growth associated with a transgranular failure propagation mode. The fracture mode presented in SEM (Fig. 4.26) revealed evidence of predominantly intergranular failure of ZTA. Previous studies have shown that the intergranular failure mode of low porosity materials such as ZTA has greater potential for energy absorption [26].

The study by Horsfall was used as template to correlate the Young modulus to ballistic performance [25]. Horsfall evaluated the Young's modulus on both a manufactured intact tile and the shattered pieces of ZTA after ballistic testing using a tungsten carbide projectile. The results gave 333 GPa and 129 GPa, respectively. This translates into a drop of 204 GPa or 61.3% during ballistic impact. The implication is that ceramics for ballistic performance should have values well above 204 GPa. This is in agreement with the results of this study.

Furthermore, in the work of Krell, it was suggested that high values of elastic modulus are beneficial for ballistic performance and the Young's modulus plays a big role in projectile damage during the ballistic dwell [19]. Therefore, SiC with a modulus of 407 GPa is much better than ZTA in this regard. Krell, however, also highlights that the effect of elastic modulus can be substantially altered by other factors such as interfacial design. Voids and other surface features on the striking face of ZTA plates are examples of such interface designs. The elastic modulus of ZTA was found to be in the range of biomorphic resin based SiC (RBSC) with a modulus of 290 GPa, which was found satisfactory for ballistic performance [35].

5.5 Nanotubes

This section discusses the results of the characterisation on the pristine nanotubes and preliminary investigation on their dispersibility.

5.5.1 CNT Loading in Alumina

Several studies have shown that a high volume fraction of carbon nanotubes (CNTs) affects densification [151, 148, 193]. It was shown that high loading can lead to agglomeration of CNTs, thus causing the formation of pores and defects that result in low densification and the deterioration of mechanical properties [151, 193]. Assuming hexagonal prismatic grains, a lower CNT loading limit of 0.72 vol % or 0.4 wt.% was suggested [118]. The study also suggested 6.4 vol.% or 3.56 wt% as upper limit. However, it was reported that agglomeration started at 0.6 vol.% [109]. The few available studies on BNNT loading in alumina recommend weight fractions between 1 and 2 wt.% [8]. Similar to the CNT situation, the incorporation of BNNT at higher volume fractions showed a negative effect on reinforced ceramics mechanical properties, leading to a decrease in density, an increase in porosity and severe agglomeration. The hardness was specifically found to strongly depend on the theoretical density (TD), the grain size and CNT loading. Considering the fact that the appropriate range of CNT or BNNT loading in alumina is a function of the purity and properties of the nanotubes, the variations of loading recorded in some studies may be justified.

In conclusion, from the analysis of literature studies on CNT loading in alumina, it can be inferred that up to 1wt.% CNT addition seems to favour the improvement of strength in cases where the theoretical density is close to 100% [130, 148]. Furthermore, K_{IC} can increase further even above 1wt.% CNT although a substantial reduction in density, hardness and strength can occur.

5.5.2 Composition and Morphology

Similar to previous studies, the SEM studies showed nanotubes in curvy, bent or wavy shapes, indicating a considerable degree of nanotube impurity, anomalies and structural defects [116, 119]. The strong entanglement found in this study on both nanotubes (NTs) is accompanied by variations in tubular diameter and is an indication of the high energy required to unbundle the nanotubes. Entangled and defective NTs pose even greater challenges of dispersion as loading increases [108, 109].

The XRD spectra on BNNT revealed the major peak as h-BN, which is consistent with the Raman peak [111]. BNNT diffraction also shows the presence of carbon and iron particles, as well as some other small peaks that are not directly identified, but whose presence is known to be due to impurities. On the other hand, the CNT spectra shows the presence of graphite, which corroborates with the amorphous carbon identified through the Raman peak. Also identified on the CNT spectra are impurities such as Fe_2C, Fe_3C and Fe_2N. These are known to be derived from the synthesis catalyst (which can be iron and iron related materials) and possibly from the raw materials used to produce the nanotubes [114].

The Raman pattern on both nanotubes further corroborates the level of impurities and defects found in the nanotubes. On BNNT, h-BN, which was also confirmed by the XRD pattern, is displayed on the 1369 cm^{-1} peak shift as the dominant feature and is known to correspond to an E_{2g} vibration mode of h-BN [111]. It is also recognized to cause plane stretching between boron and nitrogen. This peak also corresponds to polycrystalline h-BN, which has semi-metallic properties [111, 194]. The secondary peak occurs on the 670 cm^{-1} shift and displays broad and weak bands that are shown to correspond to B_2O_3 impurities [194] from the boron nanoparticles. Furthermore, the presence of BNNT impurities such as h-BN

flakes and micro-droplets of boron [111] are confirmed in SEM. Other undistinguishable peaks were also recorded and may be due to lattice disorder and unwanted by-products, such as boric acid, as reported in the literature [111]. The peak position is sensitive to defects within the h-BN lattice and, as lattice defects increase, the peaks will shift to higher wavelength [114].

The Raman pattern on the CNT showing a high intensity of 3872 on the D-band vibrational mode at 1350 cm^{-1} is known as the defect-induced band containing disordered residual ill-organised graphite or amorphous carbon, both of which are commonly regarded as impurities that affect the dispersion of CNT in ceramic matrices. They are most often produced through catalytic chemical vapour [175, 195]. The high intensity of this band is known to be sensitive to the CNT curvature, amorphous carbon and other carbon impurities as well as to non-polar atomic distortion [108]. The level of these impurities is further corroborated by the intensity of the ratio of the D-band and the G-band (I_D/I_G), which is also used to quantify defects and whose value was recorded as 1.12 [196]. It shows that CNT is relatively low in impurities, which is consistent with the manufacturer purity specification of 90% and the measured metal residues of 11% using TGA.

The G-band mode on CNT was found at 1582 cm^{-1} whereas literature has it noted as being visible on 1590 cm^{-1}. This mode is the tangential vibration mode of the graphitic carbon (graphite). The deviation of the shift recorded in this test is an indication of lattice defects [175, 196], which corroborates some of the curvy and kink tubes shown in SEM characterisation.

Also a notable mode on CNT, at less than 200 cm^{-1} shift, is usually called the radial breathing mode (RBM), and is often used to evaluate the internal diameter of the tube. It is found to be applicable when the tube's internal diameter is less than 2 nm. This mode is absent

in the present study, but is known to be found in single and double walled nanotubes. SEM investigation shows that our tube internal diameter is greater than 2 nm, indicating that the nanotubes are multi-walled. Also, it must be noted that the G'-band shift peak is placed at about the same value as the literature's 2700 cm^{-1}, which represents the metallicity of the CNT [197] and its semi-conducting properties.

In conclusion, the nanotubes synthesis method determines their level of defects or impurities. Primarily, synthesis parameters include: the nature of the catalyst, the quantity of the catalyst, the ratio of the catalyst in relation to the raw materials (starting compound), the temperature of synthesis, the reaction time and the environment of synthesis [115].

5.5.3 Thermal Properties

The anti-oxidation capacity of the nanotubes was corroborated by the results of both the direct heating and TGA. These results showed that CNT is stable in air up to 450^{o}C, which corroborates with the beginning of the weight loss temperature in the TGA investigation. Literature reports that CNTs start losing their structure at temperatures below 500^{o}C, primarily due to imperfections [116]. Also, the CNT structure was lost in vacuum and argon atmospheres at high temperature and prolonged dwell time above 4 hours. This is in agreement with current trends away from prolonged pressureless sintering towards rapid processes such as spark plasma sintering (SPS) and the new sintering method called rapid hot-pressing [76, 79]. Residues left at the end of TGA tests were recorded to be 11wt.% including all metal containing impurities, which is in agreement with XRD results. In contrast, the thermal stability of BNNT as shown by the direct heating tests, even at prolonged dwell times beyond 4 hours in vacuum, implies that BNNT has great potential to survive prolonged high temperature processing. The presence of impurities was reflected in the TGA results that

showed weight gain starting at 700°C, which is lower than the 900°C reported in literature [111, 120]. Another cause of the early mass gain in BNNT is structural imperfections, as shown in the Raman pattern results highlighting an active mode shift from 1367 to 1369 cm^{-1} due to lattice defects [196].

5.5.4 Wettability

The measured contact angle of 80° for BNNT is in agreement with values obtained using the Wilhelmy method, which are between 80.5° to 90.5° [121]. Most other literature publications report contact angles between 48 to 55° using simulations [115, 199]. The contact angle of 119° measured for CNT is in agreement with the literature value of 119.7°, obtained through molecular dynamics simulation and the manipulation of the separation distance and the 13A distance [198]. Using entangled CNT, similar simulations gave a contact angle of 144° [199] while modifying the CNT chirality and the CNT tube diameter gave contact angles between 103 and 106 ° [200]. It must be noted that many factors influence the contact angle measurements, including, but not limited to, impurities in nanotubes and surface during tests, morphology of the nanotubes, thickness of the nanotube forest and surface topography or smoothness of the nanotubes forest [201]. Overall, the results of this study are in agreement with the literature that BNNT is hydrophilic, while CNT is hydrophobic.

5.5.5 Nanotubes Dispersion

Ball milling is an efficient method to disperse nanotubes in alumina using a top down approach [124]. The Pulveriset planetary mill used in this study is known to provide high energy transfer during milling, which is required to unbundle and disperse the agglomerated nanotubes. However, it also destroyed the BNNT structure due to its relatively weak partial ionic bond [111]. Therefore, the use of a solvent as milling aid could help disperse the BNNTs

while reducing the energy transfer to prevent BNNT destruction. However, it is important to note that milling aids may compromise the purity of the composites, which could subsequently affect the composite properties. It must be mentioned that friction during dry milling can also cause excessive heating and deformation of BNNTs, which can be exacerbated by the low heat dissipation of the $\boldsymbol{\pi}$ electronic structure of BNNT [202]. In contrast; CNT survived ball-milling up to 4 hours, thanks to its strong covalent bond between the carbon atoms. This strong bond, coupled with the weak Vander Waal bonding separating layers of graphite, also contributes to providing excellent lubrication properties leading to low friction and reduced energy transfer between milling balls and CNTs. Moreover, CNTs feature a high deformation capacity allowing them to better survive high energy milling. The good energy dissipation ability of CNT also allows it to remain relatively cold during milling [203].

Overall, multiple literature reports suggest that CNT can be successfully milled either dry or wet using milling aids such as ethanol [8, 122]. The milling rotation speed is usually between 200 and 300 rpm with a milling duration of 2 to 20 hours. For example, a homogeneous nanotube dispersion was achieved using wet milling in ethanol and a planetary ball mill for 5 hours [204], a mixer mill for 24 hours [76], or a planetary ball mill in dry and wet conditions for 1 hour [163]. Moreover, it has been shown that ball milling of CNT, either dry or wet, is beneficial for removing the amorphous carbon and carbon particles in the CNT as well as opening the tip of the CNT to ensure good dispersions [122].

5.6 DOP

Ballistic assessment on the DOP tested ceramics including proposed performance index and semi-empirical model to correlate DOP to static properties and microstructure are discussed in this section.

5.6.1 Microstructure and Failure Pattern

The pinecone shaped pattern of fractured ceramics including both circular and radial cracks radiating away from the centre of the impact point as observed in this study is characteristic for dynamic fracture [4, 176]. The degree of fragmentation on the other side is an indication of its energy dissipation capacity [5], and the variability of DOP is related to flaws such as pores, their size distribution and/or clustering [18, 20], and to the variability in grain size as illustrated in Figure 4.55 for the DOP tested ceramics [21].

All DOP tested reinforced ceramics, including Al_2O_3-BNNT, Al_2O_3-CNT, and SiC-BNNT, showed an increase in grain size during processing. This hints to inefficient and non-uniform pinning effect of the nanotubes on their parent matrix grains [130, 155], leading to a large grain size distribution (Fig. 4.55). However, the larger grains and their size variation are not out of range for good ballistic performance [21].

A good dispersion of nanotubes is known to provide high relative density, small grain size, high strength, toughness and hardness. In this study, a slight grain size increase in Al_2O_3-BNNT, Al_2O_3-CNT, and SiC-BNNT was observed despite nanotube addition leading to a hardness decrease by 11.28%, 16.34%, and 11.02%, compared to their monolithic ceramics, respectively. The primary reasons for the decrease in hardness are clustering and non-uniform dispersion of nanotubes leading to residual porosity [110, 130, 161]. On the positive side, the fracture toughness increases by 2.86%, 3.38%, and 4.32%, for Al_2O_3-BNNT, Al_2O_3-CNT and SiC-BNNT, respectively, compared to their monolithic counterparts. This increase, however, is rather low considering the primary objective to significantly improve toughness. In fact, previous studies achieved toughness improvements of 103%, 67%, 50% for similar composites, respectively [145, 155, 167]. The unsatisfactory performance of the composites

in this study can be rationalised by poor interfacial bonding and dispersion as observed in SEM and previously reported in literature [130]. Also, the remaining porosity as analysed in Figures 4.52 is detrimental to ceramic properties and ballistic performance.

5.6.2 Ballistic Performance Indices

Existing performance indices in the literature were applied in this study as shown in Table 5.1. From the results on Table 5.1, four categories of ranking can be distinguished: First, the DEF and MEF produce the ranking B_4C>SiC>SiC-BNNT>Al2O3>Al2O3-SWCNT>Al_2O_3-BNNT. This ranking highlights the areal density as a major factor for armour ceramics, which is understandable because the weight is one of the key aspects in armour design [17]. These performance criteria yield critical thicknesses of 9.01 mm and 7.28 mm for SiC-BNNT and Al_2O_3, respectively, implying lower performance for SiC-BNNT.

Table 5.1: Performance indices of the ballistic test materials calculated using different index formulae.

Ballistic Performance Criteria	Formulae used for the evaluation	Materials					
		Al_2O_3	Al_2O_3-BNNT	Al_2O_3-SWCNT	SiC	SiC-BNNT	B_4C
Differential Efficiency Factor (DEF) [16]	$\rho_b \frac{(Px-Pr)}{\rho_{t*t_t}}$	11.64	11.20	11.44	14.38	11.95	17.40
Thickness Efficiency (TE) or Space Efficiency (SE) [17]	$\frac{p_x - p_r}{t_t}$	36.67	35.52	35.91	37.36	29.85	35.25
Mass Efficiency Factor (MEF) or SEF [17]	$\frac{TE * \rho_b}{\rho_t}$	11.58	11.19	11.52	14.46	12.14	17.40
Weight Saving (WS) [94]	$[1 - \frac{\rho_b * t_t + \rho_b}{\rho_{b*} Px}]*$ 100	73.03	70.92	71.98	74.87	59.69	72.64
DEF Scaling From 0 to 1 [100]	$1 - \frac{\rho_b * Pr + \rho_t * t_t}{\rho_b * Px}$	0.73	0.71	0.72	0.75	0.60	0.73
Ballistic Efficiency ($q^{2)}$: Product of MEF and TE [17]	TE * MEF	424.64	396.40	413.68	540.23	362.38	613.7
Total Efficiency Factor (TEF) [101]	$\frac{\rho_b * Px}{\rho_t * t_{t+ \rho_{b*} Pr}}$	3.71	3.44	3.57	4.0	2.48	3.66
Critical Thickness [46]	$\frac{t_t * Px}{(Px - Pr)}$	7.28	7.52	7.46	7.22	9.06	7.55
Ceramic Efficiency (%) [102]	$1 - \frac{Pr}{Px} *100$	80	77.90	78.8	80.4	65	77.1

Table 5.2: Test and critical thicknesses of the tested materials.

Material parameters	Materials					
	Al_2O_3	Al_2O_3-BNNT	Al_2O_3-SWCNT	SiC	SiC-BNNT	B_4C
Test tile thickness (t_t) (mm)	5.83	5.85	5.87	5.76	5.83	5.85
Critical thickness (t_c) (mm)	7.28	7.52	7.46	7.22	9.06	7.55
% difference $\frac{t_c - t_t}{t_t} *$ 100	24.9	28.5	27.1	25.3	55.4	29.1
Weight at critical thickness (g)	276.64	287.26	279.0	223.82	267.27	183.47

Second, the TE, CT and efficiency criteria support the following ranking: SiC> Al_2O_3>Al_2O_3-SWCNT>Al_2O_3-BNNT>B4C>SiC-BNNT. This ranking seems to focus on the depth of penetration (DOP). Although DOP is the main measure of performance, it requires further analysis to assess the overall ballistic performance. Moreover, Al_2O_3 has never been found in any study to outperform B4C.

Third, the WS, DEF (with scale from 0-1) and the TEF criteria yield a ranking as SiC>Al_2O_3>B_4C>Al_2O_3-SWCNT>Al_2O_3-BNNT>SiC-BNNT. This ranking is similar to the second case above. Again, the suggestion is that alumina outperforms B_4C, which is not supported by literature.

Fourth, the ballistic efficiency index produces a ranking that can be detailed as B_4C>SiC>Al_2O_3>Al_2O_3-SWCNT>Al_2O_3-BNNT>SiC-BNNT. This ranking is based on an overlap of two performance indices (MEF and TE) and seems to provide higher accuracy and agreement with literature findings.

Overall, all rankings above suggest that alumina composites are in a similar performance range and are outperformed by monolithic alumina. However, this conclusion shall be taken with caution and further extensive studies are required to better understand the performance of these materials since a variety of factors can influence the DOP tests [20, 86]. For instance, defects affect both the fragmentation [22, 106] and the fracture morphology.

Based on the discussions above, an effort was made to simulate the DOP test results using a gradient factor. The result is the proposed performance index calculated using the areal density and the inverse depth of penetration (DOP) as in Equation 5.2. The calculated indices are presented in Table 5.3.

$$\eta = \frac{\boldsymbol{DOP^{-1}}}{\boldsymbol{A_D}} = \frac{\mathbf{1}}{\boldsymbol{DOP \times A_D}} \quad (5.2)$$

The resulting performance ranking is B_4C>SiC>Al_2O_3>Al_2O_3-SWCNT>Al_2O_3-BNNT> SiC-BNNT. The new ranking is in good agreement with the total ballistic efficiency as can be seen in Table 5.4. The Table provides normalised indices with B_4C as reference.

Table 5.3: Proposed index working table.

Performance index working parameters	**Materials**					
	Al_2O_3	**Al_2O_3-BNNT**	**Al_2O_3-SWCNT**	**SiC**	**SiC-BNNT**	**B_4C**
DOP^{-1} (m^{-1})	18.63	16.90	17.65	19.11	10.70	16.31
A_D (Kg/m^2)	22.15	22.35	21.95	17.86	17.20	14.22
DOP^{-1}/A_D	8.41	7.56	8.04	10.70	6.22	11.47
Over B_4C Normalised Index	0.73	0.66	0.70	0.93	0.54	1

Table 5.4: Comparison of the proposed index with the ballistic efficiency index as normalised over the corresponding indices for B4C.

Performance index comparison	**Materials**					
	Al_2O_3	**Al_2O_3-BNNT**	**Al_2O_3-SWCNT**	**SiC**	**SiC-BNNT**	**B_4C**
Normalised ballistic efficiency index	0.69	0.65	0.67	0.88	0.59	1
Propose normalised index	0.73	0.66	0.70	0.93	0.54	1

The proposed performance index suggests that B_4C outperforms all other materials but was only marginally higher than SiC, which is in agreement with literature [204]. It also shows that SiC-BNNT provides the lowest performance.

5.6.3 Model Simulation to Correlate Properties to DOP

Table 5.5 summarises the properties used for modelling. The hardness, absolute density and fracture toughness were measured by standard methods using ASTM 1326-09, Archimedes method and ASTM 1410, respectively. The other properties were taken from relevant literature including the compressive strength [207], the Young's modulus [206, 207] and the sonic velocity [9]. For all the reinforced materials, the values were assumed base on the level of porosity compared to their monolithic materials. The largest flaw size was measured on polished samples and was taken as primary microstructure parameter, assuming that the porosity is already considered in the density.

Table 5.5: DOP results and properties of test ceramics used for modelling.

Property	**Materials**					
	Al_2O_3	**Al_2O_3-BNNT**	**Al_2O_3-SWCNT**	**SiC**	**SiC-BNNT**	**B_4C**
DOP (mm)	53.67	59.17	56.67	52.33	93.5	61.33
Standard deviation on DOP	1.15	9.22	9.11	5.86	20.20	5.13
Density (g/cm^3)	3.80	3.82	3.74	3.10	2.95	2.43
Hardness (GPa)	18.97	16.83	15.87	27.87	24.84	30.49
Toughness ($MPa\sqrt{m}$)	3.85	3.96	3.98	3.01	3.14	3.83
Compressive strength (GPa)	3.0	2.80	2.85	3.9	3.7	2.9
Young's modulus (GPa)	360	365	370	415	400	450
Sonic velocity (Km/s)	10.8	10.8	10.8	12	11.8	14
Flaw size (μm)	11	23	18	10	44	14

Modelling was performed in two steps. First, power law functions were used to determine the correlation of each individual property to DOP. The obtained equations are

presented in Table 5.6, corresponding plots are shown in Figure 5.4 and the modelled values are summarised in Table 5.7. It can be seen from Figure 5.4 that only the fracture toughness (K_{IC}), the density (ρ) and the flaw size (a) constructively correlate with DOP. They show that microstructure and processing optimisation to achieve high toughness, high density and reduced flaws would reduce DOP.

Table 5.6: Power functions data for the simulation.

Property	**Function**	**Regression R^2**
Hardness (HV)	$\mathbf{35.033}\boldsymbol{HV}^{\frac{3}{16}}$	0.0551
Fracture toughness (K_{IC})	$\mathbf{138.59}\boldsymbol{K_{IC}}^{\frac{-16}{25}}$	0.1376
Young's modulus (E)	$\mathbf{3.7639}\boldsymbol{E}^{\frac{7}{15}}$	0.0368
Absolute density (ρ)	$\mathbf{101.96}\boldsymbol{\rho}^{\frac{-13}{30}}$	0.1333
Sonic velocity (c_v)	$\mathbf{24.482}\boldsymbol{c}^{\frac{3}{8}}$	0.0321
Compressive strength (σ_c)	$\mathbf{34.457}\boldsymbol{\sigma}^{\frac{1}{2}}$	0.1157
Flaw size (a_f)	$\mathbf{22.558}\boldsymbol{a}^{\frac{7}{20}}$	0.8106

Table 5.7: Ceramics properties and DOP as measured and modelled using different approaches.

Model parameters	**Materials and model values**					
	Al_2O_3	**Al_2O_3-BNNT**	**Al_2O_3-SWCNT**	**SiC**	**SiC-BNNT**	**B_4C**
HV (GPa)	60.83	59.48	58.83	65.39	63.98	66.49
K_{IC} (MPa$\sqrt{m}$)	58.48	57.44	57.25	68.46	66.63	58.68
E (GPa)	58.69	59.07	59.45	62.72	61.65	65.13
ρ (g/cm^3)	57.17	57.04	57.57	62.44	63.80	69.40
c_v (Km/s)	59.76	59.76	59.76	62.16	61.77	65.86
σ_c (GPa)	59.68	57.66	58.57	68.05	66.30	58.68
a_f (µm)	52.21	67.59	62.04	50.50	84.82	56.81
Experimental DOP (mm)	53.67	59.17	56.67	52.33	93.5	61.33
Modelled DOP using only K_{IC}, a and ρ (mm)	55.89	60.50	58.91	59.99	71.18	61.39
% diff.	4.14	2.25	3.96	14.64	23.87	0.09
Modelled DOP using all properties (mm)	58.12	59.72	59.07	62.52	66.61	62.92
% diff.	8.28	0.92	4.23	19.47	28.76	2.60
Matlab derived DOP using only K_{IC}, a and ρ (mm)	48.28	61.80	57.03	54.25	91.33	61.08
% diff.	10.05	4.45	0.63	3.66	2.32	0.41

*% diff. means difference of modelled DOP to experimental DOP.

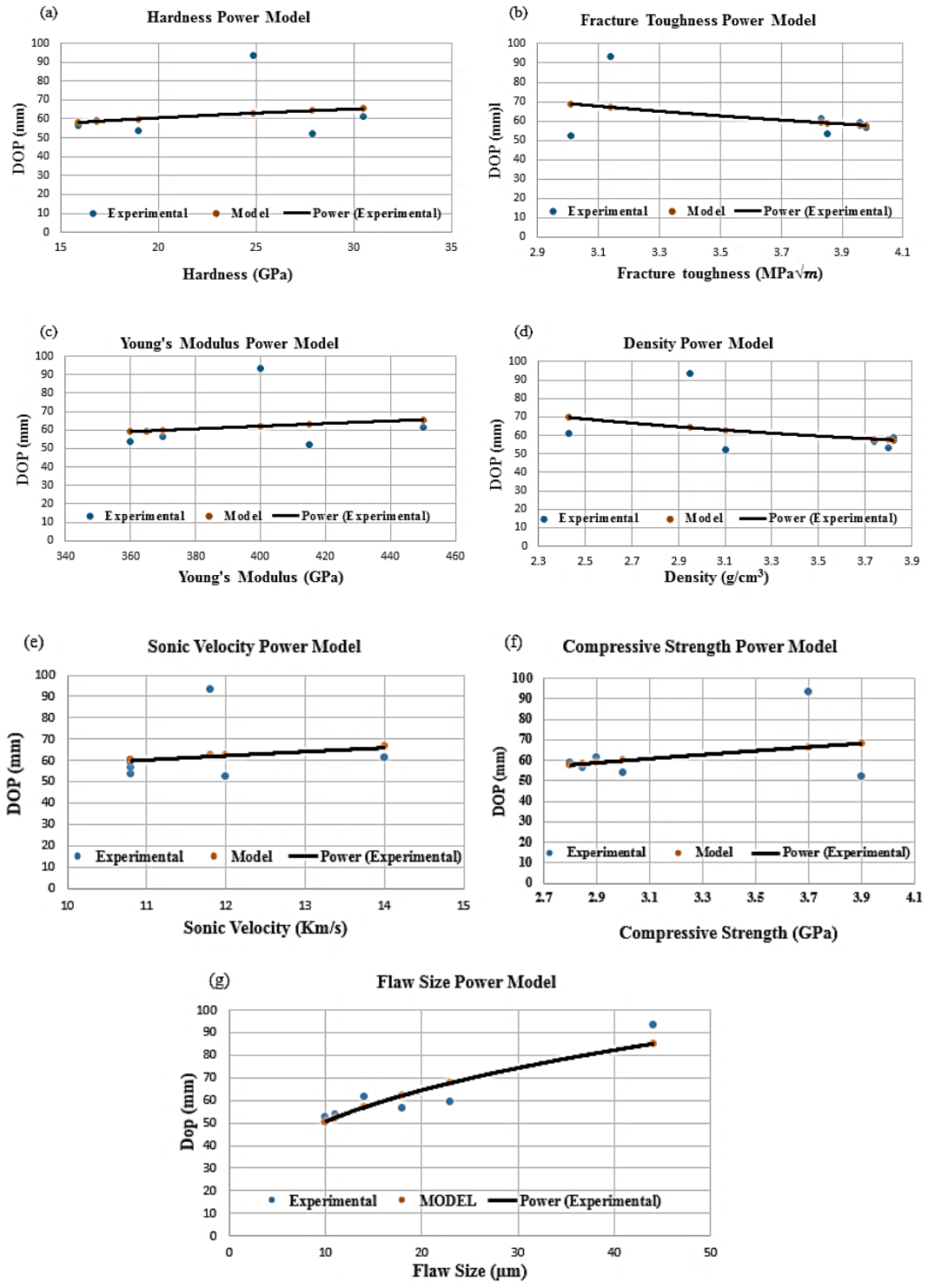

Figure 5.4: Power law models showing the correlation between mechanical properties and DOP: (a) hardness; (b) fracture toughness; (c) Young's modulus; (d) density; (e) sonic velocity; (f) compressive strength; and (g) flaw size.

Therefore, only these three parameters were combined in the first cumulative model approach to describe DOP, as in Equation 5.3. Solving the product yields Equation 5.4 plotted in Figure 5.5.

$$\mathbf{DOP} = (\mathbf{138.59}\, K_{IC}^{\left(\frac{-16}{25}\right)} * \mathbf{101.96}\, \rho^{\left(-\frac{13}{30}\right)} * \mathbf{22.558}\, a_f^{\left(\frac{7}{20}\right)})^{1/3} \tag{5.3}$$

$$\mathbf{DOP} = \mathbf{68.31} * \frac{a_f^{\left(\frac{7}{60}\right)}}{K_{IC}^{\left(\frac{16}{75}\right)} * \rho^{\left(\frac{13}{90}\right)}} \tag{5.4}$$

For the sake of completeness, all seven properties were also combined into a product in a second general model as in Equation 5.5. This product simplifies to Equation 5.6 and is plotted in Figure 5.6.

$$\mathbf{DOP} = [\mathbf{35.033}HV^{\left(\frac{3}{16}\right)} * \mathbf{138.59}\, K_{IC}^{\left(\frac{-16}{25}\right)} * \mathbf{101.96}\, \rho^{\left(-\frac{13}{30}\right)} * \mathbf{3.7639}E^{\left(\frac{7}{15}\right)} * \mathbf{24.482}c_v^{\left(\frac{3}{8}\right)} * \mathbf{34.457}\sigma_c^{\left(\frac{1}{2}\right)} * \mathbf{22.558}a_f^{\left(\frac{7}{20}\right)}]^{1/7} \tag{5.5}$$

$$\mathbf{DOP} = \mathbf{32.14} * \frac{HV^{\left(\frac{3}{112}\right)} * E^{\left(\frac{1}{15}\right)} * c_v^{\left(\frac{3}{56}\right)} * \sigma_c^{\left(\frac{1}{14}\right)} * a_f^{\left(\frac{1}{20}\right)}}{K_{IC}^{\left(\frac{16}{175}\right)} * \rho^{\left(\frac{13}{210}\right)}} \tag{5.6}$$

The regression plots for the two cumulative models are shown in Figure 5.7.

.

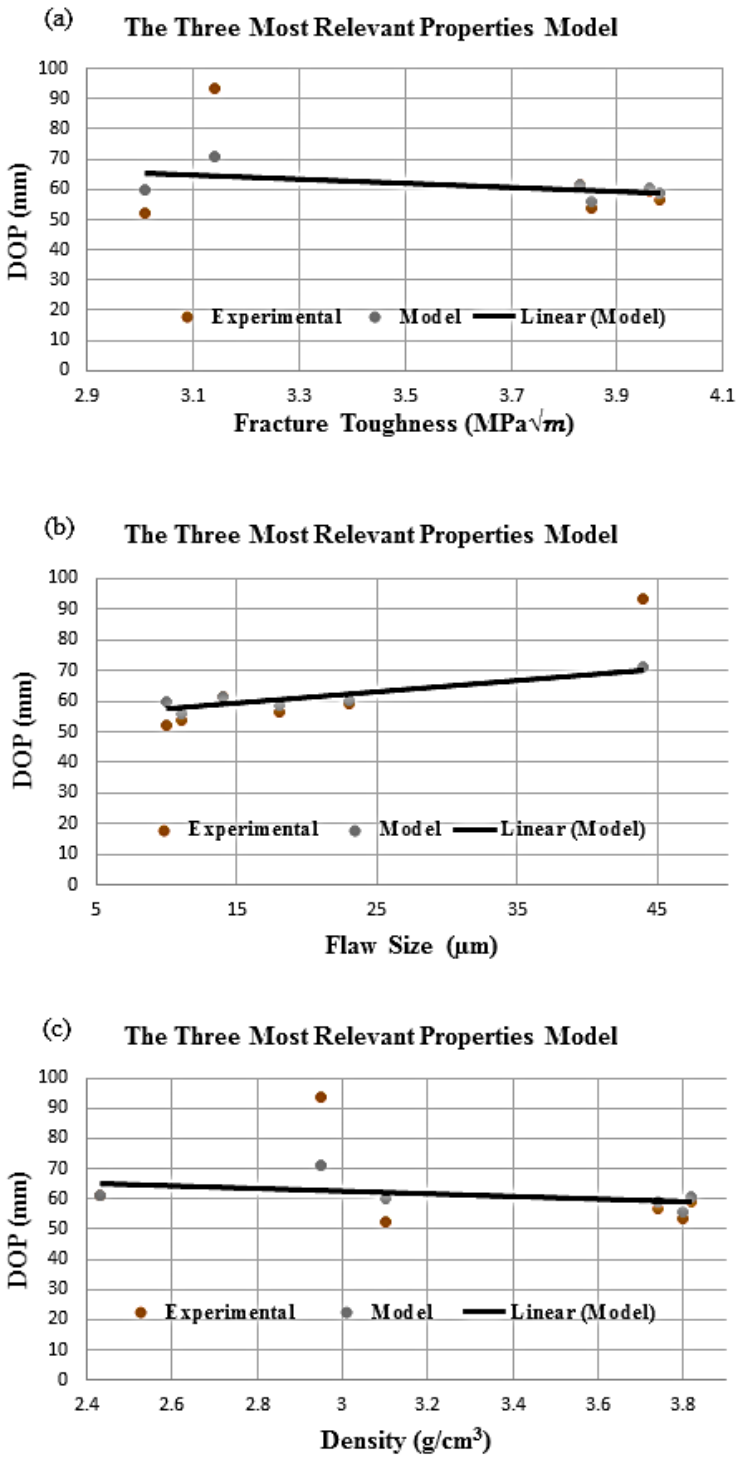

Figure 5.5: Models including only K_{IC}, af and ρ expressing the DOP as a function of: (a) fracture toughness; (b) flaw size; and (c) density.

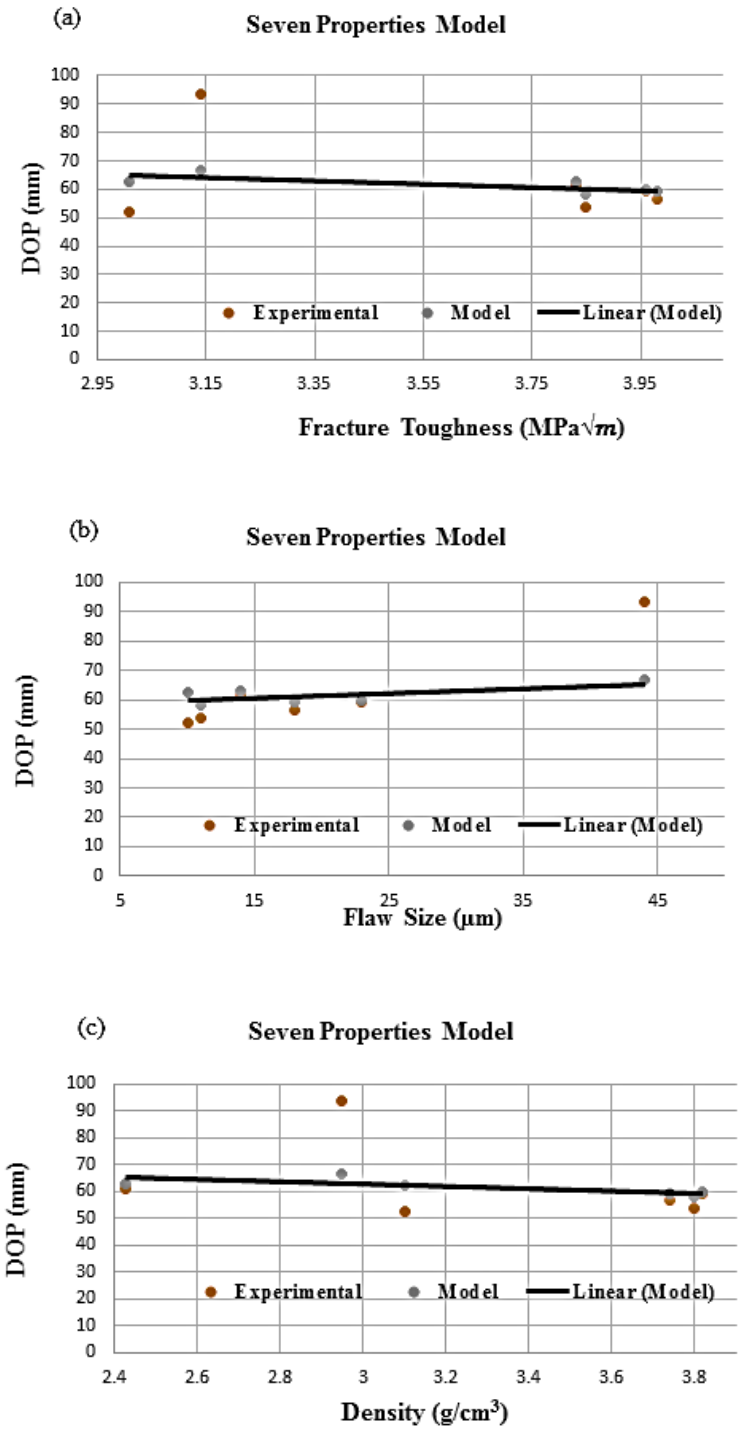

Figure 5.6: Model including all measured properties expressing the DOP as a function of: (a) fracture toughness; (b) flaw size; and (c) density.

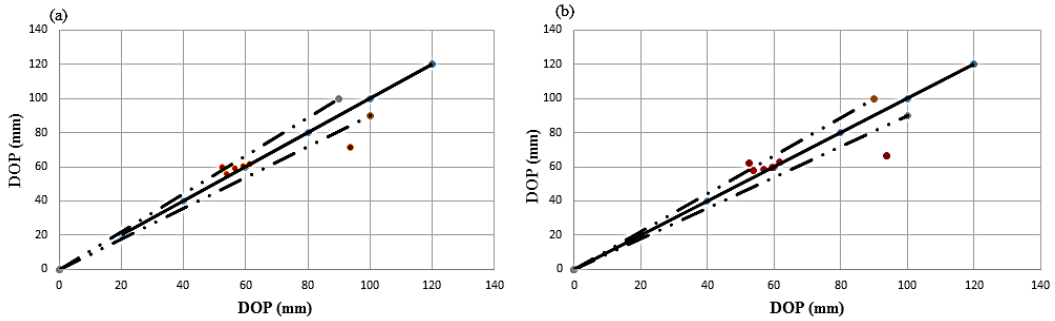

Figure 5.7: Regression plot and 10% error ranges for the semi-empirical models and the experimental DOP data: (a) Modelling including only K_{IC}, af and ρ; and (b) model including all seven properties.

Matlab modelling including only K_{IC}, a_f and ρ yielded the correlation shown in Equation 5.7 and Figure 5.8. Matlab results are consistent with model Equation 5.4 and Figure 5.5 in term of the position of the individual properties within the equation (numerator or denominator) and how they can be expected to influence the DOP. In contrast, Matlab modelling using all seven properties as shown in Equation 5.8 and Figure 5.8 was inconclusive due to the large amount of data necessary to determine the large number of unknowns. As a result, all individual properties were assigned a positive power law exponent (numerator), which is inconsistent with the semi-empirical models and experimental observation of the individual properties influence on the DOP. Therefore, similar to the semi-empirical models, Matlab suggests that modelling shall only include the major factors such as K_{IC}, a_f and ρ as the inclusion of less relevant properties such as HV, E, c_v and σ_c can lead to erroneous conclusions.

$$\mathbf{DOP} = \mathbf{51.0118} * \frac{\boldsymbol{a_f}^{(\frac{7}{20})}}{\boldsymbol{K_{IC}}^{(\frac{1}{3})} * \boldsymbol{\rho}^{(\frac{1}{3})}} \tag{5.7}$$

$$\mathbf{DOP} = \mathbf{0.1129} * \boldsymbol{HV}^{\frac{3}{16}} * \boldsymbol{E}^{\frac{7}{15}} * \boldsymbol{c_v}^{\frac{3}{8}} * \boldsymbol{\sigma_c}^{\frac{23}{50}} * \boldsymbol{a_f}^{\frac{2}{5}} * \boldsymbol{K_{IC}}^{\frac{7}{50}} * \boldsymbol{\rho}^{\frac{3}{10}} \tag{5.8}$$

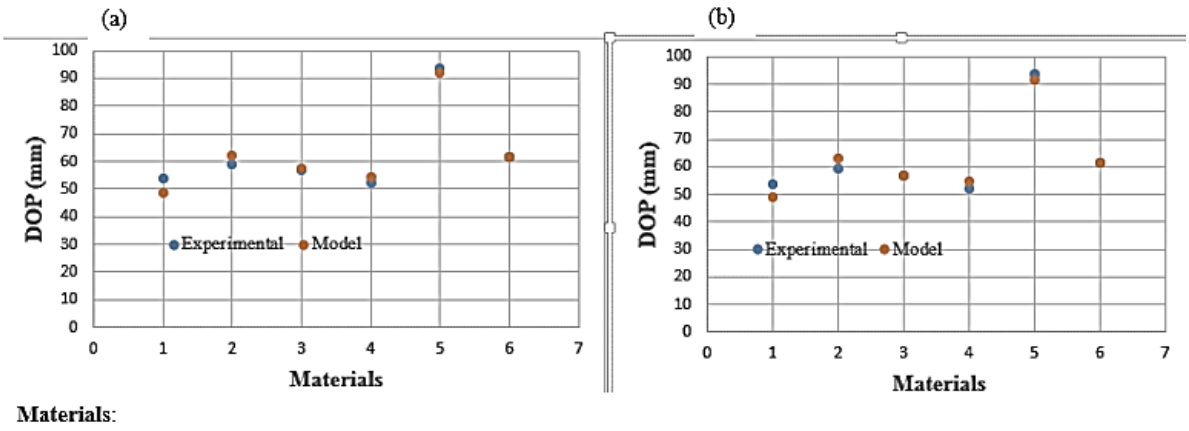

Figure 5.8: Matlab DOP prediction using (a) only K_{IC}, a and ρ for all tested ceramics; and (b) all seven properties for all tested ceramics.

Modelling suggests that the hardness, the Young's modulus, the strength and the sonic velocity do not play any constructive or systematic role in the ballistic performance for the DOP set-up used in this study. These properties are much higher for the tested ceramics than for the projectile used for DOP testing. Therefore, relatively small changes do not affect the DOP results making them behave irrelevant for the ballistic performance.

Overall, the models are in agreement with previous studies highlighting a reduction in flaws and porosity or an increase in toughness and density as key for armour ceramic performance [19, 30, 208]. However, although unanimously supported by the armour ceramic community, the present conclusion that improved toughness leads to better ceramic armour performance is in contradiction with some existing literature [19, 26, 28]. This apparent contradiction with literature can be rationalised by the fact that increased toughness is often accompanied by an even greater drop in hardness, which can overcompensate or overwrite the positive effect of toughening, leading to an overall drop in ballistic performance.

CHAPTER 6

CONCLUSIONS

Through this study, capabilities and expertise were developed for the characterisation of ceramics. It was shown that the proper method for ceramic characterisation depends on the microstructure. This study also demonstrates that the influence of microstructural features on the ballistic performances of ceramic is enormous, which corroborates the studies completed by other researchers. Following are specific conclusions of the work:

1. Knoop indentation is more appropriate than Vickers indentation for hardness measurement on ZTA and SiC due to the microstructure anisotropy in these ceramics. For both methods, a strong indentation size effect is observed with load independent hardness values measured above 2 kgf indentation load.
2. The Vickers indentation technique is successfully used to measure the fracture toughness and provided values that are in agreement with the results from drop weight, ring-on-ring and Charpy impact tests.
3. It is shown that second phase particles introduced during the manufacturing of ZTA and SiC not only improved fracture toughness but also downplayed the effect of porosity or inclusions. The fracture toughness of both materials was higher compared to their monolithic counterparts and literature values even with 10% porosity on ZTA and inclusions in SiC.
4. Additionally, the second phase particles demonstrated a trade-off between hardness and K_{IC}. Furthermore, the porosity and inclusions in ZTA and SiC, respectively, lead to a drop in hardness, strength and Young's modulus.

5. Nanotube reinforcement increases the ceramic toughness, but decreases the hardness and strength to an even greater extent. Therefore, a CNT content below 1wt.%, for instance, is recommended for toughening alumina. Higher contents lead to nanotube agglomeration, increased porosity and ultimately to poor ballistic performance.
6. A new ballistic performance index is proposed using the inverse DOP (1/DOP) and areal density as an indicator of ballistic performances for armour ceramics. The new index proves to produce a better ranking of the tested ceramics as compared to existing literature indices.
7. A new semi-empirical model for simulating the depth of penetration (DOP) is developed using quasi-static mechanical properties and existing flaws. The model reveals that only the fracture toughness, the maximum flaw size and the density are appropriate for predicting the DOP. The other mechanical properties, including the hardness, the strength and the elastic modulus, are much higher than comparative values of the used hard steel projectile. Therefore, their relatively small improvements achievable by manufacturing process optimisations do not remarkably increase the ballistic performance.

OUTLOOK

The current study suggests that toughening, specifically using nanotubes, can also lead to an even greater decrease in hardness that can result in an overall drop in ballistic performance. This is contrary to the overall objective of improving armour ceramics. Therefore, the following is recommended for future work.

1. More DOP ballistic tests on both monolithic and nanotubes reinforced ceramics to better cover statistical variations and re-assess the proposed performance index and semi-empirical model.
2. Further work is needed on microstructural design to achieve the desired properties in armour ceramic. This should primarily focus on determining the appropriate second phases as well as their optimal volume fraction, particle size and distribution.
3. Further ball milling testing to optimise milling aid, intensity and duration may allow a more uniform nanotube dispersion and consequently better ballistic performance.
4. Expand the developed model and other existing simulations in order to establish a single performance correlation considering all the microstructural parameters including grain size, porosity, inclusions, their sizes and distribution.
5. Consider gradient ceramic composites with nanotube content increasing towards the back of the armour plate. This can provide the needed hardness at the impact face while improving the toughness in the bulk of the ceramic.

SCIENTIFIC CONTRIBUTIONS

The following new contributions have been made in this work.

A. Characterised two commonly used armour ceramics, SiC and ZTA. The characterisation included microstructure assessment and experimental testing. Furthermore, multiple equations for indentation fracture toughness determination were assessed showing that the equations for median type cracking by Lawn et al and Nihara are the most accurate.

B. Contributed to the understanding of the toughening capacity of nanotubes (CNT, BNNT) in armour ceramics.

C. Developed a new ceramic performance ranking index as:

$$\frac{\mathbf{1}}{\boldsymbol{DOP} * \boldsymbol{A_D}}$$

This new index is found to be more accurate and in agreement with experimental observations than most currently used indices.

D. Developed a model to correlate mechanical properties and microstructure to the depth of penetration (DOP). This new semi-empirical model shows that only ceramic armour properties in the range of their projectile counterparts shall be considered. These include the fracture toughness, the flaw size and the density.

E. Publications:

Journal Papers:

1. Nastic, A.; Merati, A.; Bielawski, M.; **Fakolujo, O.;** Bolduc, M.; and Nganbe, M. (2015). Instrumented and Vickers Indentation for the Characterization of Stiffness, Hardness and Toughness of Zirconia Toughened Al_2O_3 and SiC Armor. Journal of Materials Science & Technology 31, 773-783.

2. **Fakolujo, O.**; Merati, A.; Bielawski, M.; Bolduc, M.; and Nganbe, M. (2016). Role of Microstructural Features in Toughness Improvement of Zirconia Toughened Alumina. J. of Mineral and Mater. Charact. & Eng. 4 87 - 102

Book Chapter

1. **Fakolujo, O**.; Merati, A.; Bielawski, M.; Bolduc, M.; and Nganbe, M. (2014). A Study of Armour Related Properties of Ceramics. Ceramic Transaction 249, 82 – 90.

International Conference Abstracts and Presentations:

1. **Fakolujo, O.**; Merati, A.; Bielawski, M.; Bolduc, M.; and Nganbe, M. A Study of Armour Related Properties of Ceramics. International Conference on Materials Science and technology, MST 2013.
2. **Fakolujo, O**.; Merati, A.; Bielawski, M.; Bolduc, M.; and Nganbe, M. A Study of Toughening Mechanism in Zirconia Toughened Alumina ICANM 2015: International Conference & Exhibition on Advanced & Nano Materials, Ottawa, Ontario, Canada, 2015.

NRC Internal Reports:

1. Merati, A.; **Fakolujo, O**; and Nastic,A. Characterization of Armour Ceramics-Summary Report. Volume 1 of 1. Report No LTR-SMPL-2013-0070 by Aerospace-Structures, Materials and Manufacturing (SMM) National Research Council Canada, 2013.

2. Bielawski, M.; Au, P.; **Fakolujo, O**.; Guan, J.; Lee, R.; Lin, S.; Lo, J.; Merati, A.; Morphy, D.; Nastic, A.; Santos, R.; Saragosa, J.; Simard, B.; Walsh, D.; Zhang, R. Improvement of Ceramic Armour Materials for the Canadian Special Forces-Progress, Report No. 2 Vol. 1 of 1. Report No: LTR-SMPL-2013-0077, by Aerospace-Structures, Materials and Manufacturing (SMM), National Research Council Canada, 2013.
3. Merati, A.; Lupandina, O.; and **Fakolujo, O**. 2015, Failure Analysis of DOP Tested Armour Ceramic Tiles, Vol. 1 of 1. Report No: LTR-SMM-2015-0403 0077; by Aerospace-Structures, Material and Manufacturing (SMM), National Research Council Canada, 2015.

REFERENCES

[1] Den Reijer, P. C., (1991), "Impact on Ceramic Faced Armour". Ph.D. Thesis, University of Technology, Delft, Netherland.

[2] Karandikar, P., Givens, B., and Liszkiewicz, A., (2015), "Effects of Novel Geometric Designs on the Ballistic Performance of Ceramics," 38th International Conference on Advanced Ceramics and Composites, J. C. LaSalvia, ed. Wiley, U.S.A., 4: 13-22.

[3] Fellows, N., and Barton, P., (1999), "Development of Impact Model for Ceramic-Faced Semi-Infinite Armour," Int. J. Impact Eng., **22**(8): 793-811.

[4] Sujirote, K., Dateraska, K., and Chollacoop, N., (2007), "Some Practical Requirements for Alumina Armour System," Advances in Ceramic Armour III: 71-89.

[5] Cho J., Boccacini. A. R, and Shaffer, M. S. P., (2009), "Review Ceramic Matrix Composites Containing Carbon Nanotubes," Mater. Sci., **44**:1934-1951.

[6] Evans, G. A., (1982), "Structural Reliability: A Processing Dependent Phenomenon" J. Am. Ceram. Soc., **65**(3): 127-137.

[7] Medvedovski, E., (2010), "Ballistic Performance of Armour Ceramics: Influence of Design and Structure. Part 1," Ceram. Int, **36**: 2103-2115.

[8] Wang, W., Bi, J., Sun, K., Bu, M., Long, N., and Bai, Y., (2011), "Fabrication of Alumina Ceramic Reinforced with Boron Nitride Nanotubes with Improved Mechanical Properties," J. Am. Ceram. Soc, **94**(11): 3636-3640.

[9] Savage, G., (1990), "Ceramic Armour," J. Metals and Mater.: 487-495.

[10] Niesz, D. E., and McCauley, J. W., (2007), "Advanced Metals and Ceramics for Armour and a High-Fidelity Design and Processing of Advanced Armour Ceramics." Report of U.S. Army Research Laboratory Material Centre of Excellence ARL-CR 594, 81-90.Anti-Armour Applications. Aberdeen Proving Ground MD.

[11] Ullner, C., Germak, A., Doussal, H. L., Morrell, R., Reich, T., and Vandermeuleu, W., (2001), "Hardness Testing on Advanced Technical Ceramics" J. Eur. Ceram. Soc., **21**: 439-451.

[12] Morrell, R., (1990), "Ceramics Guideline for Conducting Hardness Tests on Advanced Ceramic Materials," VAMAS Technical Report 8, National Physics Laboratory.

[13] Machaka, R., Derry, T. E., and Sigalas, I., (2011), "Analysis of the Indentation Size Effect in the Microhardness Measurements in B6O," J. Advances in Matl. Sc. and Eng Article ID 539252, doi:10.1155/2011/539252: 539-544.

[14] Guder, H. S., Sahin, E., and Sahin, O., (2011), "Vickers and Knoop Indentation Microhardness Study of SiAlON Ceramic," Acta Physica Polonica A, 120(6): 1026-1033.

[15] Quinn, G. D., and Bradt, R. C., (2007), "On the Vickers Indentation Toughness Test," J. Am. Ceram. Soc, **90**(3): 673-677.

[16] Rosenberg, Z., Bless, S. J., and Yeshurun, Y., (1988), "A New Definition of Ballistic Efficiency of Brittle Materials Based on the Use of Thick Backing Plates," Impact Loading and Dynamic Behaviour of Materials, **1**: 491-498.

[17] Madhu, V., Ramanjaneyulu, K., Bhat, T. B., and Gupta, N. K. (2005), "An Experimental Study of Penetration Resistance of Ceramic Armour Subjected to Projectile Impact," Int. J. Impact Eng., **32**: 337-350.

[18] Kaufmann, C., Cronin, D., Worswick, M., Pageau, G and Beth, A. (2003), "Influence of Material Properties on the Ballistic Performance of Ceramics for Personal Body Armour" J. Shock Vibration, **10**: 51-58.

[19] Krell, A., and Strassburger, E., (2014), "Order of Influence on the Ballistic Resistance of Armour Ceramics and Single Crystals," Mater. Sci. Eng.: A, **597**: 422-430.

[20] Bakas, M., McCauley, J. W., and Greenhut, V., (2012), "Quantitative Analysis of Inclusion Distributions in Hot Pressed Silicon Carbide" Int. J. Impact Eng., **50**: 40-48.

[21] Goncalves, D., De Melo, F.C.L., Nklein, A., and Al-Qureshi, H.A., (2004), "Analysis and Investigation of Ballistic Impact on Ceramic/Metal Composite Armour" Int. J. of Mach. Tool Manuf. **44**: 307-316.

[22] Bakas, M. P., (2006), "Analysis of Inclusion Distributions in Silicon Carbide Armor Ceramics," Ph.D. Thesis, the State University of New Jersey Rutgers.

[23] Demibras, M. V., 2008, "Microstructure-Property Relationship in Silicon Carbide Armour Ceramics," Ph.D. Thesis, the State University of New Jersey Rutgers.

[24] Swab, J. J., (2004), "Recommendations for Determining the Hardness of Armour Ceramics," J. Appl. Ceram. Technol. **3**: 219-225.

[25] Horsfall, I., Edwards, M. R., and Hallas, M. J., (2010), "Ballistic and Physical Properties of Highly Fractured Alumina," Adv. Appl. Ceram., **109**(8): 498-503.

[26] Flinders, M., Ray, D., Anderson, A., and Cutler, R.A. (2005), "High-Toughness Silicon Carbide as Armor," J. Am. Ceram. Soc., **88**(8): 2217-2229.

[27] Nesphor, V. C., Zaitsav, G. P., Dovgal, E. J., Maystrenko, A. L., and Dasevskaya, O. B., (1995), "Armour Ceramics Ballistic Efficiency Evaluation," Proceedings of the 8th CIMTEC on Ceramics Charting the Future Italy., 28: 2395-2396.

[28] Woodward, R., Gooch, W., and Odonnell, R., (1994), "A Study of Fragmentation in the Ballistic Impact of Ceramics," Int. J. Impact Eng., **15**(5): 605-618.

[29] Samal S. S., and Bal, S., (2008), "Carbon Nanotube Reinforced Ceramics Matrix Composites-A Review" J. of Minerals and Materials Characterisation Eng., **7**(4): 355-370.

[30] Savio, S. G., Madhu, V., and Gogia, A. K., (2014), "Ballistic Performance of Alumina and Zirconia-Toughened Alumina against 7.62 Armour Piercing Projectile," Defence Science Journal, **64**(5): 464-470.

[31] Ren, H. L., Chen, W., and Guo, T. T. (2013), "Numerical Simulation in Anti-Penetration Properties of Ceramics Target" Beijing Ligong Daxue Xueba/Transaction of Beijing Institute of Technology, **33**(2): 111-115.

[32] Rice, R. W., 2003, "Ceramic Fabrication Technology Marcel Dekker, Inc., New York.

[33] Carter, C. B., and Grant, M. N., 2013, " Ceramic Materials: Science and Engineering." Springer, New York.

[34] Walley, S. M., (2010), "Historical Review of High Strain Rate and Shock Properties of Ceramics Relevant to their Application in Armour," Advances in Applied Ceramics, **109**(8): 446-466.

[35] Karandikar, P. G., Evans, G., Wong, S., and Aghajanian, M. K., (2009), "A Review of Ceramics for Armour Application," Ceramic Engineering and Science, American Ceramics Society, **29**: 163-175.

[36] Wilkins, M. L., Cline, C. F., and Honodel, C. A., (1969) "Fourth Progress Report on Light Armor Program, Report No UCRL-50694, Lawrence Radiation Laboratory Livermore C.A USA.

[37] Colombo, P., Zordan, F., and Medvedovski, E., (2006), "Ceramic-Polymer Composites for Ballistic Protection," Adv. Appl. Ceram. **105**(2): 78-83.

[38] Shokriel, M. M., and Javadpour, G. H., (2008), "Penetration Analysis of a Projectile in Ceramic Composite Armour," Compos. Struct. **82**: 269-276.

[39] Hetherington, J. G., (1992), "The Optimization of Two Component Composite Armours," Int. J. Impact Eng. **12**(3): 409-414.

[40] Medvedovski, E., (2010), "Ballistic Performance of Armour Ceramics: Influence of Design and Structure. Part 2," Ceram. Int. **36**: 2117-2127.

[41] Medvedovski, E., (2006), "Lightweight Ceramic Composite Armour System," Adv. Appl. Ceram. **105**(5): 241-245.

[42] López-Puente, J., Arias, A., and Zaera, R., (2006), "The Effect of the Thickness of the Adhesive Layer on the Ballistic Limit of Ceramic/Metal Armours. An Experimental and Numerical Study," Int. J. Impact Eng. **32**(1-4): 321-336.

[43] Shockey, D. A., Simons, J. W., and Curran, D. R., (2010), "The Damage Mechanism Route to Better Armor Materials," Int. J. Appl. Ceram. Technol. **7**(5): 566-573.

[44] Kesharaju, M., and Nagarajah, R., (2014), "Determination of Density Variation and Microstructure in Reaction-Sintered SiC Ceramics using Ultrasonic Time-of-Flight" Int. J. Appl. Ceram. Technol., **11**(2): 303-310.

[45] Quinn, J. B., and Quinn, G. O., (1997), "Indentation Brittleness of Ceramics: A Fresh Approach," J. Mater. Sci.: 4331-4347.

[46] Hazell, P.J., 2006, "Ceramic Armour Design and Defeat Mechanics," Argos Press Canberra, Australia, pp. 168.

[47] Quinn, G. D., 1998, "Hardness Testing of Ceramics-Metallography," Adv. Mater. and Pro. Magaz. **154**(2): 7 pp.

[48] ASTM International, West Conshohocken, PA, 2008, ""Standard Test Method for Vickers Indentation Hardness of Advanced Ceramics" ASTM Standard C 1327.

[49] ASTM International, West Conshohocken, PA, 2013, "Standard Test Method for Knoop Indentation Hardness of Advanced Ceramics" ASTM Standard C1326.

[50] Krell, A., and Schadlich, S., (2001), "Nanoindentation Hardness of Submicrometer Alumina Ceramics," J. Mater. Sci. and Eng. **307**(1-2): 172-181.

[51] Sakai, M., (1993), "Energy Principle of the Indentation Induces Inelastic Surface Deformation and Hardness of Brittle Materials," Acta Metall. Mater., **41**(6): 1251-1258.

[52] Marshall, D. B., (1983), "Controlled Flaws in Ceramics. A Comparison of Knoop and Vickers Indentation," J. Am. Ceram. Soc, **66**(2): 127-131.

[53] ASTM International, West Conshohocken, PA, 2010, "Standard Test Methods for Determination of Fracture Toughness of Advanced Ceramics at Ambient Temperatures," ASTM Standard C1421.

[54] Sergejev, F., and Antonov, M., (2006), "Comparative Study on Indentation Fracture Toughness Measurements of Cemented Carbides," Proc. Estonian Acad. Sci. Eng., **12**(4): 388-398.

[55] Rocha-Rangel, E., (2011), "Nanocomposites with Unique Properties and Application in Medicine and Industry,"Intechopen: 21-39.

[56] Szutkowska, M., (2012), "Fracture Toughness of Advanced Alumina Ceramics and Alumina Matrix Composites used for Cutting Tool Edges," J. of Achivements in Mater. Manuf. Eng. **54**(54): 202-208.

[57] Ubeyli, M., Yildirim, R. O., and Ogel, B. (2005), "On the Drop-Weight Testing of Alumina/Aluminum Laminated Composites," Sadhara, **30**(5): 673-686.

[58] ASTM International, West Conshohocken, PA, 2013, "Standard Test Method for Flexural Strength of Advanced Ceramics at Ambient Temperature," ASTM Standard C1161.

[59] ASTM International, West Conshohocken, PA, 2009, "Standard Test Method for Monotonic Equibiaxial Flexural Strength of Advanced Ceramics at Ambient Temperature," ASTM Standard C1499-09.

[60] Ritter, J. E., (1980), "Appraisal of Biaxial Strength Tests," J. Non-Crystalline Solids, **38 & 39**: 419-424.

[61] Nakamura, S., Tanaka, S., Kato, Z., and Uematsu, K. (2009), "Strength-Processing Defects Relationship Based on Micrographic Analysis of Fracture Mechanic in Alumina Ceramics," J. Am. Ceram. Soc., **92**(3): 688-693.

[62] Nielsen, L. F., (1990), "Strength and Stiffness of Porous Materials" J. Am. Ceram. Soc., **73**(9),: 2684-2689.

[63] Wang, SF., Hsu, YF., Pu, JC., Sung, J. C., and Hwa, L. G. (2004), "Determination of Acoustic Wave Velocities and Elastic Properties for Diamond and Other Hard Materials," J. Mater. Chemistry and Physics, **85**: 432-437.

[64] Zimmermann, K., and Schneider, G. A., (2009), "Elastic to Elastic-Plastic Transition of Al2O3/TiC Ceramics Studies by Nanoindentation," J. Mater. Res., **24**(6): 1960-1966.

[65] Phani, K. K., and Niyogi, S. K., (1987), "Young's Modulus of Porous Brittle Solids," J. Mater. Sci. **22**: 257-263.

[66] Gyger, Jr. L. S., Kulkarni, P., Bruck, H.A., Gupta, S.K. and Wilson, Jr. O. C. (2007) Replamineform Inspired Bone Structures (RIBS) Using Multi-Piece Molds and Advanced Ceramic Gelcasting Technology" Mater Sci. & Eng: C **27**(4), 646–653

[67] Basu, B., and Balani, K, 2009, "Advanced Structural Ceramics," John Wiley & Sons Inc., Hoboken New Jersey.

[68] Ray, D. A., Kaur, S., and Cusher, R. A., (2008), "Effects of Additives on the Pressure-Assisted Densification and Properties of Silicon Carbide," J. Am. Ceram. Soc., **91**(7): 2163-2169.

[69] Gubernat, A., Stobierski, L., and Labaj, P., (2007), "Microstructure and Mechanical Properties of Silicon Carbide Pressureless Sintered with Oxide Additive," J. Eur. Ceram. Soc., **27**: 781-789.

[70] Magnani, G., Beaulardi, L., and Pillotti, L., (2005), "Properties of Liquid Phase Pressureless Sintered Carbide Obtained Without Sintering Bed," J. Eur. Ceram. Soc., **25**: 1619-1627.

[71] Trongklaig, W., Dateraksa, K., and Atong. D, (2006), "The Effect of Raw Material, Composition, and Processing on Properties of Pressureless Sintered Spray-dried Alumina Ceramics", The Fourth Thailand Materials Science and Technology Conference, March 2006.

[72] King, A.G., 2002, "Ceramic Technology and Processing," William Andrew Noyes, Norwich, N.Y. U.S.A.

[73] Deng, ZY., Fukasawa, T., Ando, M., Zhang, GJ., and Ohji, T. (2001), "Microstructure and Mechanical Properties of Porous Alumina Ceramics Fabricated by the Decomposition of Aluminum Hydroxide," J. Am. Ceram Soc, **84**(11): 2638-2644.

[74] Lee, S., and Kim, Y., (2001), "Relationship between Microstructure and Fracture Toughness of Toughened Silicon Carbide Ceramics," J. Am. Ceram. Soc., **84**(6): 1347-1353.

[75] Ganesh, I., Sundararajan, G., Olhero, S. M., and Ferreira, J. M. F. (2011), "Influence of Chemical Composition on Sintering Ability of ZTA Ceramic Consolidated from Freeze Dried Granules," Ceram. Int., **37**: 835-841.

[76] Jiang, D., Thomson, K., Kuntz, J. D., Agerb, J. W., and Mukherjee, A. K. (2007), "Effect of Sintering Temperature on a Single Wall Carbon Nano-Toughened Alumina-Based Nanocomposite," Scripta Materialia, **56**: 959-962.

[77] Teng, C. H., Ting, C. Y., Tan, S., and Ramesh, W. D. (2008), "Sintering of Alumina with Titania as Sintering Additive." The International Conference on Construction and Building Technology ICCBT 2008.

[78] Ahmad, I., Cao, H., Chen, H., Zhao, H., and Kennedy, A. (2010), "Carbon Nanotube Toughened Aluminium Oxide Nanocomposite", J. Eur. Ceram. Soc., **30**: 865-873.

[79] Hanzel, O., Sedlácek, J., and Hadzimová, E., (2015), "Thermal Properties of Alumina-MWCNTs Composites," J. Eur. Ceram. Soc., **35**(5): 1559-1567.

[80] Evans, G. A., (1990), "Perspective on the Development of High-Toughness Ceramics," J. Am. Ceram. Soc. **73**(2): 185-205.

[81] Asenov, St. Lakov, L. and Toncheva, Kr. (2013), "Promising Ceramic Materials for Ballistic Protection," J. Chemical Technol. and Metall., **48**(2): 190-195.

[82] Shockey, D. A., Marchand, A. H., and Skaggs, S. R., (1990), "Failure Phenomenology of Confined Ceramic Targets and Impacting Rods," Int. J. Impact Eng, **9**(3): 263-275.

[83] James, B., (2003), "Practical Issues in Ceramic Armour Design", Ceramic Armor Materials by Design, Ceramic Transactions."American Ceramic Society, Vol. 134: 33-44.

[84] Ben-Dor, G., Dubinsky, A., and Elperin, T., (2009), "Improved Florence Model and Optimization of Two-Component Armor against Single Impact or Two Impacts," Composite Structures, **88**(1) pp. 158-165.

[85] Franzen, R. R., Orphal, D. L., and Anderson, C. E. (1997), "The Influence of Experimental Design on Depth-of-Penetration (DOP) Test Results and Derived Ballistic Efficiencies," Int. J. Impact Eng., **19**(8): 727-737.

[86] Carton, E. P., Roebroeks, G. H. J. J., and Vandar Wal, R. (2013), "Dynamic Material Characterization by Combining Ballistic Testing and an Engineering Model," 8 pp.

[87] Zaera, R., and Sanchez-Galvez, V., (1998), "Analytical Modelling of Normal and Oblique Ballistic Impact on Ceramic/Metal Lightweight Armours," Int. J. Impact Eng., **21**(3): 133-148.

[88] Chi, R., Serjouei, A., and Sridhar, I., (2013), "Ballistic Impact on Bi-Layer Alumina/Aluminium Armor: A Semi-Analytical Approach," Int. J. Impact Eng., **52**: 37-46.

[89] Anderson Jr., C. E., and Walker, J. D., (2005), "An Analytical Model for Dwell and Interface Defeat," Int. J. Impact Eng., **31**(9): 1119-1132.

[90] Ballistic Resistance of Body Armour NIJ Standard-010.(2008) Office of Law Enforcement Standards, National Institute of Standards and Technology United States of America.

[91] Department Of Defense, (1998), "Test Method Standard Ballistic Performance Ranking of Ceramic Armor Plates against High Density Penetrators", MIL-STD-376 A.

[92] NATO Standard, (2003), "Ballistic Test Method for Personal Armour Materials and Combat Clothing 2003 NATO Standard." Stanag 2920 PPS (Edition 2).

[93] Roberson, C., and Hazell, P. J., (2003), "Resistance of Silicon Carbide to Penetration by a Tungsten Carbide Cored Projectile," Ceramic Transactions, 151: 165-174.

[94] Hazell, P. J., Fellows, N. A., and Hetherington, J. G., (1998), "A Note on the Behind Armour Effects from Perforated Alumina/Aluminium Targets," Int. J. Impact Eng., **21**(7): 589-595.

[95] Lundberg, P., and Lundberg, B., (2005), "Transition between Interface Defeat and Penetration for Tungsten Projectiles and Four Silicon Carbide Materials," Int. J. Impact Eng., **31**(7): 781-792.

[96] Zhang, X. F., and Li, Y. C., (2010), "On Comparison of the Ballistic Performance of 10% Zirconia Toughened Alumina and 95% Alumina Ceramic Target," Mater. and Design, **31**: 1945-1952.

[97] Wang, B., and Lu, G., (1996), "On the Optimization of Two Component Plates Against Ballistic Impact," J. Mater. Process Technol., **57**(1-2): 141-145.

[98] Woodward, R., (1990), "A Simple One-Dimensional Approach to Modeling Ceramic Composite Armor Defeat," Int. J. Impact Eng., **9**(4): 455-474.

[99] Savio, S. G., Ramanjaneyulu, K., and Madhu, V., (2011), "An Experimental Study on Ballistic Performance of Boron Carbide Tiles," Int. J. Impact Eng., **38**(7): 535-541.

[100] Bless, S., and Anderson, C., (1993), "Penetration of Hard Layers by Hypervelocity Rod Projectiles," Int. J. Impact Eng., **14**(1-4): 85-93.

[101] Meyers, M.A., 1994, " Dynamic Behaviour of Material,"John Wiley & Sons Inc., New York, Chap. 605.

[102] Yadav, S. and Ravichandran, G., (2003), "Penetration Resistance of Laminated Ceramic/Polymer Structures," Int. J. Impact Eng., **28**: 557-574.

[103] Chen, W. W., Rajendra, A. M., Song, B., and Nie, X. (2007), "Dynamic Fracture of Ceramics in Armour Application," J. Am. Ceram. Soc., **90**(4): 1005-1018.

[104] LaSalvia, J. C., Campbell, J., Swab, J.J., and McCauley, J.W, (2010), "Beyond Hardness Ceramics and Ceramic-Based Composites for Protection," J. of Mater. for Crashworthiness and Defense, **62**(1): 1543-1548.

[105] Riou, P., and Denoual C., (1998), "Visualisation of the Damage Evolution in Impacted SiC Ceramics," Int. J. Impact Eng., **21**(4): 225-13.

[106] Nanda, H., Appleby-Thomas, G. J., and Wood, D. C., (2011), "Ballistic Behaviour of Explosively Shattered Alumina and Silicon Carbide Targets" Adv. Appl. Ceram., **110**(5): 287-292.

[107] Rosenberg, Z., (2008), "On the Mechanisms for Defeating AP Projectiles," International Journal of Modern Physics B, **22**(9-11): 1277-1284.

[108] Fawad, I., (2009), "Development of Ceramic-Carbon Nanotube (CNT) Nanocomposites," Ph.D Thesis. University of London.

[109] Sarkar, S., and Das, P. K., (2014), "Processing and Properties of Carbon Nanotube/Alumina Nanocomposites: A Review," Reviews on Adv. Mater. Sci., **37**(1-2): 53-82.

[110] Yamamoto, G., Omori, M., and Hashida, T., (2008), "A Novel Structure for Carbon Nanotube Reinforced Alumina Composites with Improved Mechanical Properties," Nanotechnol., **19**(31): 7 pp.

[111] Zhi, C. Y., Bando, Y., and Tang, C. C., (2010), "Boron Nitride Nanotubes." Mater. Sci. Eng. Res., **70**: 92-111.

[112] Wang, W., Bi, J., and Wang, S. (2011), "Microstructure and Mechanical Properties of Alumina Ceramics Reinforced by Boron Nitride Nanotubes," J. Eur. Ceram. Soc., **31**(13): 2277-2284.

[113] Ahmad, I., Yazdani, B., and Zhu, Y., (2015), "Review Recent Advances on Carbon Nanotubes and Graphene Reinforced Ceramics Nanocomposites," Nanomater., **5**: 90-114.

[114] Tanur, A. E., (2012), "Structure and Properties of Nanomaterials: From Inorganic Boron Nitride Nanotubes to the Calcareous Biomineralized Tubes of *H.* Dianthus Ph.D. Thesis University of Toronto. Canada.

[115] Kalay, S., Yilmaz, Z., and Çulha, M., (2013), "Synthesis of Boron Nitride Nanotubes from Unprocessed Colemanite," Beilstein J. Nanotechnol., **4**: 843-851.

[116] Ahmad, A., Kholoud, M. M., Abou, E. N., Reda A. A. A., and Abdulrahman, A.W, (2012), " Review Carbon Nanotubes, Science and Technology Part (I) Structure, Synthesis and Characterisation:" Arabian J. of Chemistry, **5**: 1-23.

[117] Collins, P.G., (2009), "Oxford Handbook of Nanoscience and Technology: Frontiers and Advances" . A.V. Narlikar, & Y.Y. Fu, Eds. Oxford Univ. Press, Oxford.

[118] Hu, N. (2012), "Composites and Their Properties" a Chapter 20 Intech ISBN 978-953-51-0711-8.

[119] Lehman, J. H., Terrones, M., and Mansfield, E., (2012), "Review: Evaluating the Characteristics of Multiwall Carbon Nanotubes" Carbon, **49**: 2581-2602.

[120] Kim, K. S., Kingston, C. T., and Hrdina, A., (2014), "Hydrogen-Catalyzed, Pilot-Scale Production of Small-Diameter Boron Nitride Nanotubes and their Macroscopic Assemblies," ACS Nano. 2014, **8**(6): 6211-6220.

[121] Yum, K., and Yu, M. F., (2006), "Measurement of Wetting Properties of Individual Boron Nitride Nanotubes with the Wilhelmy Method using a Nanotube-Based Forced Sensor," J. of Nano Letters, **6**(2): 329-333.

[122] Munkhbayar, B., Nine, M. J., and Jeoun, J., (2013), "Influence of Dry and Wet Ball Milling on Dispersion Characteristics of the Multi-Walled Carbon Nanotubes in Aqueous Solution with and without Surfactant," Powder Techn., **234**: 132-140.

[123] Kukovecz, A., Kanyo, T., Konya, Z., and Kiricsi, I, (2005), "Long-Time Low-Impact Ball Milling of Multi-Wall Carbon Nanotubes " Carbon, **43**: 994-1000.

[124] Yadav, T. P., Yadav, R. M., and Singh, D. P., (2012), " Mechanical Milling: A Top Down Approach for the Synthesis of Nanomaterials and Nanocomposites," Nanosci. and Nanotechnol., **2**(3): 22-48.

[125] Kim, G., Bae, G. and Kim, H. (2014), "The Characterisation of Alumina Reinforced with Carbon Nanotube by the Mechanical Alloying Method," Mater. Res. Innovations, 18(SUPPL. 3): S12-S15.

[126] Fan, J. P., Zhao, D., and Wu, M., (2006), "Preparation and Microstructure of Multi-Wall Carbon Nanotubes Toughened Al_2O_3 Composite " J. Am. Ceram. Soc., **89**(2): 750-753.

[127] Xia, Z., Riester, L., and Curtin, W. A., (2004), "Direct Observation of Toughening Mechanisms in Carbon Nanotube Ceramic Matrix Composites," Acta Materialia, **52**(4): 931-944.

[128] Yamamoto, G., Shirasu, K., and Hashida, T., (2011), "Nanotube Fracture during the Failure of Carbon Nanotube/Alumina Composites," Carbon, **49**: 3709-3716.

[129] Pavia, F., and Curtin, W. A., (2013) "Molecular Modeling of Cracks at Interfaces in Nanoceramic Composite". J. of The Mech. and Phy. of Solids **61**(10): 1971-1982

[130] Ahmad, K., and Pan, W., (2015), "Microstructure-Toughening Relation in Alumina Based Multiwall Carbon Nanotube Ceramic Composites," J. Eur. Ceram. Soc., **35**(2): 663-671.

[131] ASTM Standard E112, (2012), "Standard Test Methods for Determining Average Grain Size" ASTM International, West Conshohocken, PA, 2012, DOI: 10.1520/E112-12, Www.Astm.Org.

[132] ASTM Standard E1245-03, (2008), "Standard Practice for Determining the Inclusion Or Second-Phase Constituent Content of Metals by Automatic Image Analysis", ASTM International, West Conshohocken, PA, 2008, DOI: 10.1520/E1245-08, www.Astm.Org.

[133] ASTM Standard B962-08, (2008), "Standard Test Methods for Density of Compacted Or Sintered Powder Metallurgy (PM) Products using Archimedes' Principle", ASTM International, West Conshohocken, PA, 2008, DOI: 10.1520/B0962-08,www.Astm.Org.

[134] Mandache, C., Brothers, M., and Merati, A., (2012), "Concomitant Measurement of Sound Velocity and Path Length in a Ceramic Test Piece by Ultrasonic Waves," LM-SMPL-2012-0071, National Research Council, Montreal Road Ottawa.

[135] Asmani, M., "Influence of Porosity on Young's Modulus and Poisson's Ratio in Alumina," J. Eur. Ceram. Soc.: 1066-1081.

[136] Luo, J. S. R., (1999), "Porosity-Dependency of Elastic Moduli and Hardness of 3Y-T2P Ceramic," Ceram. Int., **25**: 281-286.

[137] Lankford, J., (1982), "Indentation Microfracture in Palmqvist Crack Regime: Implication for Fracture Toughness Evaluation by the Indentation Method," J. Mater. Sci. Lett. 1: 493-495.

[138] Liang, K. M., (1990), "Evaluation by Indentation Fracture Toughness of Ceramic Materials," J. Mater. Sci., **35**: 207-214.

[139] ASTM Standard D5628, (2010), "Standard Test Method for Impact Resistance of Flat, Rigid Plastic Specimens by Means of a Falling Dart (Tup or Falling Mass)", ASTM International, West Conshohocken, PA, 2010, DOI: 10.1520/C1327-10, Www.Astm.Org.

[140] Yi, J., Xue, W. J., and Xie, Z. P., (2015), "A Novel Processing Route to Develop Alumina Matrix Nanocomposites Reinforced with Multi-Walled Carbon Nanotubes," Mater. Res. Bulletin, **64**: 323-326.

[141] Bakhsh, N., Khalid, F. A., and Hakeem, A. S., (2014), "Effect of Sintering Temperature on Densification and Mechanical Properties of Pressureless Sintered CNT-Alumina Nanocomposites," IOP Conference Series: Materials Science and Engineering, 60, doi:10.1088/1757-899X/60/1/012059 7 pp.

[142] Ahmad, I., Islam, M., and Almajid, A. A., (2014), "Investigation of Yttria-Doped Alumina Nanocomposites Reinforced by Multi-Walled Carbon Nanotubes," Ceram. Int., **40**(7 Part A): 9327-9335.

[143] Ghobadi, H., Nemati, A., and Ebadzadeh, T., (2014), "Improving CNT Distribution and Mechanical Properties of MWCNT Reinforced Alumina Matrix," Mater. Sci. Eng. A, **617**: 110-114.

[144] Yamamoto, G., Shirasu, K., and Nozaka, Y., (2014), "Microstructure-Property Relationships in Pressureless-Sintered Carbon Nanotube/Alumina Composites," Mater. Sci. Eng.: A, **617**: 179-186.

[145] Inam, F., Heaton, A., and Brown, P., (2014), "Effects of Dispersion Surfactants on the Properties of Ceramic-Carbon Nanotube (CNT) Nanocomposites," Ceramics International, **40** (1 Part A): 511-516.

[146] Kasperski, A., Weibel, A., and Estournès, C., (2014), "Multi-Walled Carbon Nanotube-Al_2O_3 Composites: Covalent or Non-Covalent Functionalization for Mechanical Reinforcement," Scripta Materialia, **75**: 46-49.

[147] Hanzel, O., Sedlácek, J., and Šajgalík, P., (2014), "New Approach for Distribution of Carbon Nanotubes in Alumina Matrix," J. Eur. Ceram. Soc., **34**(7): 1845-1851.

[148] Bakhsh, N., Khalid, F. A., and Hakeem, A. S. (2013), "Synthesis and Characterization of Pressureless Sintered Carbon Nanotube Reinforced Alumina Nanocomposites", Mater. Sci. Eng.: A, **578**: 422-429.

[149] Puchy, V., Hvizdos, P., and Dusza, J., (2013), "Wear Resistance of Al_2O_3–CNT Ceramic Nanocomposites at Room and High Temperatures," Ceram. Int., **39**: 5821-5826.

[150] Kasperski, A., Weibel, C., Laurent, Ch. E., and Peigney, A., (2013), "Preparation-Microstructure-Property Relationships in Double-Walled Carbon Nanotubes/Alumina Composites." Carbon, **53**: 62-72.

[151] Sarkar, S., and Probal K. D., (2012), "Temperature and Load Dependent Mechanical Properties of Pressureless Sintered Carbon Nanotube/Alumina Nanocomposites." Mater. Sci. Eng.: A, **531**: 61-69.

[152] Sarkar, S., and Probal K. D., (2012), "Microstructure and Physicomechanical Properties of Pressureless Sintered Multiwalled Carbon Nanotube/Alumina Nanocomposites," Ceram. Int., **38**: 423-432.

[153] Thomson, K. E., Jiang, I. D., and Yao, W., (2012), "Characterization and Mechanical Testing of Alumina-Based Nanocomposites Reinforced with Niobium and/or Carbon Nanotubes Fabricated by Spark Plasma Sintering," Acta Materialia, **60**: 622-632.

[154] Yamamoto, G., and Hashida, T., 2012, "Composite and their Properties Material," A Chapter in a Book, InTech, Japan: 483-502.

[155] Fu, Z., Huang, L., and Zhang, J., (2012), "Ultra-Fast Densification of CNTs Reinforced Alumina Based on Combustion Reaction and Quick Pressing," Science China Technological Sciences, **55**(2): 484-489.

[156] Inbaraj, SR., Francis, RM., Jaya, NV., and Kumar, A., (2012), "Processing and Properties of Sol Gel Derived Alumina-Carbon Nanotube Composites," J. of Ceram. Int., **38**: 4065-4074.

[157] Zaman, A. C., Üstündag, C. B., and Kaya, F., (2012), "OH and COOH Functionalized Single Walled Carbon Nanotubes-Reinforced Alumina Ceramic Nanocomposites," Ceram. Int., **38**(2): 1287-1293.

[158] Wu, X. W., Xiao, J. Z., Xia, F., Hu, Y. G., and Peng, Z., (2011), "Preparation and Mechanical Properties of Carbon Nanotubes Reinforced Alumina Ceramic Composite," Adv. Mater. Res., 237-242: 2721-2727.

[159] Lee, K., Mo, C. B., and Park, S. B., (2011), "Mechanical and Electrical Properties of Multi-Walled CNT-Alumina Nanocomposites Prepared by a Sequential Two-Step Processing of Ultrasonic Spray Pyrolysis and Spark Plasma Sintering" J. Am. Ceram. Soc., **94**(11): 3774-3779.

[160] Bi, S., Hou, G., and Su, X., (2011), "Mechanical Properties and Oxidation Resistance of a-Alumina/Multi-Walled Carbon Nanotube Composite Ceramics," Mater. Sci. Eng.: A, **528**(3): 1596-1601.

[161] Zhang, S.C., Fahrenholtz, W. G., Hilmas, G. E., and Yadlowsky, E. J., (2010), "Pressureless Sintering of Carbon Nanotube–Al_2O_3 Composites", J. Eur. Ceram. Soc., **30**: 1373-1380.

[162] Ahmad, I., Unwin, M., and Cao, H., (2010), "Multi-Walled Carbon Nanotubes Reinforced Al_2O_3 Nanocomposites: Mechanical Properties and Interfacial Investigations: "Compos. Sci. Technol., **70**: 1199-1206.

[163] Kim, S., Chung, W. S., Sohn, K., Son, C., and Lee, S: (2009), "Improvement of Flexure Strength and Fracture Toughness in Alumina Matrix Composites Reinforced with Carbon Nanotubes" " Mater. Sci. Eng.: A, **517** 293-299.

[164] Zhang, T., Kumari, L., and Du, G. H., (2009), "Mechanical Properties of Carbon Nanotube–Alumina Nanocomposites Synthesized by Chemical Vapor Deposition and Spark Plasma Sintering"," Compos.: A, **40**: 86-93.

[165] Lei, S., Yue-Feng, Z., Chan, Z., and Ji, L. (2009), "Heterocoagulation System Assisted Adsorption of Carbon Nanotubes on Alumina for Toughening Ceramics", J. Reinforced Plastics Compos., **27**(3): 245-253.

[166] Estili, M., Kawasaki, A., and Sakamoto, H., (2008), "the Homogeneous Dispersion of Surfactantless, Slightly Disordered, Crystalline, Multiwalled Carbon Nanotubes in Alumina Ceramics for Structural Reinforcement: Acta Materialia, **56**: 4070-4079.

[167] Wei, T., Fan, Z., and Luo, G., (2008), "A New Structure for Multi-Walled Carbon Nanotubes Reinforced Alumina Nanocomposite with High Strength and Toughness," Mater. Lett., **62**: 641-644.

[168] Wei, T., Fan, Z., and Luo, G., (2008), "The Effect of Carbon Nanotubes Microstructures on Reinforcing Properties of SWNTs/Alumina Composite," Mater. Res. Bulletin, **43**(10): 2806-2809.

[169] Fan, J. P., Zhuang, D. M., and Zhao, D. Q., (2006), "Toughening and Reinforcing Alumina Matrix Composite with Single-Wall Carbon Nanotubes," Appl. Phys. Lett., **89**: 121910-1-4.

[170] Gao, L., Jiang, L., and Sun, J., (2006), "Carbon Nanotube-Ceramic Composites." J Electroceram, **17**: 51-55.

[171] Chan, B., Mo, C. B., and Cha, S. I., (2005), "Fabrication of Carbon Nanotube Reinforced Alumina Matrix Nanocomposite by Sol–gel Process," Mater. Sci. Eng.: A, **395**: 124-128.

[172] Sun, J., Gao, L., and Jin, X., (2005), "Reinforcement of Alumina Matrix with Multi-Walled Carbon Nanotubes," Ceram. Int., **31**: 893-896.

[173] Sun, J., Gao, L., and Li, W., (2002), "Colloidal Processing of Carbon Nanotube/Alumina Composites," Chem. Mater., **14**: 5169-5172.

[174] Zhan, G. D., Kuntz, J. D., and Wan, J., (2002), "Single-Wall Carbon Nanotubes as Attractive Toughening Agents in Alumina Based Nanocomposites," Nat. Mater., **2**: 38-42.

[175] Datsyuk, V., Kalyva, M., Papagelis, K., Parthenois, J., Tasis, D., Siokou, A., Kallitsis, I., and Galiotis, C. (2008) "Chemical Oxidation of Multiwalled Carbon Nanotube" J. of Carbon, **46**: 833-840.

[176] Merati, A., Lupandina, O., and Fakolujo, O., (2015), "Failure Analysis of DOP Tested Armour Ceramic Tiles", Aerospace-Structures, Materials and Manufacturing (SMM), National Research Council Canada, LTR-SMM-2015-0403 0077 Vol. 1 of 1.

[177] Casellas, D., Nagl, M. M., Llanes, L., and Anglada, M. (2003) "Fracture Toughness of Alumina and Zirconia Toughened Alumina"

[178] Du, B., Zhao, B., and Duan, T., (2012), "Influence of Zirconia Content and Grain Size on Physical and Mechanical Properties of ZTA Ceramics," J. Appl. Mechanics Mater., **143-144**: 485-488.

[179] Ray, J. C., Panda, A. B., Saha, C.R., and Pramanik, P., (2003), "Synthesis of Niobium (V) Stabilised Tetragonal Zirconia Nanocrystalline Powders," J. Am. Ceram. Soc., **86**(3): 514-516.

[180] Flinder, R. M., (2008) "Microstructural Control of Silicon Carbide for Ballistic Application" M.Sc. Thesis, The University of Utah, United States of America.

[181] Kristic, V. D., and Vlajic, M., (1999), "Making of Sintered Silicon Carbide Bodies," Patent number: 123,918 (5470806) 8 pp.

[182] Sciti, D., Balbo, A., and Bellosi, A., (2005), "Improvement Offered by Coprecipitation of Sintering Additives of Ultrafine SiC Materials," Adv. Eng. Mater., **7**(3): 152-158.

[183] Mercurio, S., and Haber, R. A., 2008, "Silicon Carbide Microstructure Improvements for Armor Applications," *Advances in Ceramic Armor III*, Lisa Prokurat Franks, ed. American Ceramics Society: 155-159.

[184] Forquin, P., Tran, L., Louvigne, PF., Rota, L., and Hild, F., (2003), "Effect of Aluminum Reinforcement on the Dynamic Fragmentation of SiC Ceramics," Int. J. Impact Eng., **28**: 1061-1076.

[185] Yang. X., Liu, X., Huang, Z., Yao, X., and Liu, G., (2013), "Vickers Indentation Crack Analysis of Solid Phase Sintered Silicon Carbide," Ceram. Int., **39**: 841-845.

[186] Curkovic, L., Rede, V., Grilec, K., and Mulabdic, A., (2007), "Hardness And Fracture Toughness Of Alumina Ceramics," 12 Conference on Materials, Processes Friction and Wear MATRIB 07: 40-45.

[187] Karandikar, P. G. Evans, G., Wong, S., and Aghajanian, M.K., (2010), "Effect of Grain Size, Shape and Second Phases on Properties of Sintered SiC," Material Concepts, Processes and Characterization: Ceramic Armour V American Ceramic Society: 69-81.

[188] Wang, J., and Stevens, R., (1989), "Review Zirconia-Toughened Alumina (ZTA) Ceramics," J. Mater. Sci., **24**: 3421-3440.

[189] Dıaz, A., and Hampshire, S., (2005), "Comparison of Mechanical Properties of Silicon Nitrides with Controlled Porosities Produced by Different Fabrication Routes," J. Am. Ceram. Soc., **88**(3): 698-706.

[190] Medvedovski, E., 2006, "Advanced Ceramics for Personnel Armor: Current Status and Future," 107th Annual Meeting of the American Ceramic Society, April 10, 2005 - April 13, American Ceramic Society, Baltimore, MD, United states, 178: 3-17.

[191] Huang, S., Binner, J., Vaidhyanathan, B., Brown, P., Hampson, C., and Spacie, C., (2011), "Development of Nano Zirconia Toughened Alumina for Ceramics Armour Application," Advanced in Ceramics Armour VII Ceramic Engineering and Science, J. Swab, ed. American Ceramic Society.

[192] Spriggs, R. M., (1961), "Expression for Effect of Porosity on Elastic Modulus of Polycrystalline Refractory Material Particularly Aluminum Oxide," J. Am. Ceram. Soc.: 628-629.

[193] Zapata-Solvas, E., Gómez-García, D., and Domínguez-Rodríguez, A., (2012), "Towards Physical Properties Tailoring of Carbon Nanotubes-Reinforced Ceramic Matrix Composites," J. Eur. Ceram. Soc., **32** (12): 3001-3020.

[194] Matveev, A. T., Firestein, K. L., and Steinman, A. E., (2015), "Boron Nitride Nanotube Growth via Boron Oxide Assisted Chemical Vapor Transport-Deposition Process using $LiNO_3$ as a Promoter," Nano Res., **8**(6): 2063-2072.

[195] Dresselhaus, M. S., Dresselhaus, and G., Saito, R., (2005), "Raman Spectroscopy of Carbon Nanotubes Phys. Reports, 409: 47-99.

[196] M. Zdrojek, M., Gebicki, W., and Jastrzebski, C., (2004), "Studies of Multiwall Carbon Nanotubes using Raman Spectroscopy and Atomic Force Microscopy," Solid State Phenomena, **99**(265): 4pp.

[197] Tune, D. D., Blanch, A. J., and Krupke, R., (2014), "Nanotube Film Metallicity and its Effect on the Performance of Carbon Nanotube–silicon Solar Cells," Phys. Status Solid A, **211** (7): 1479-1487.

[198] Yijin Mao, Y., Chen, C. L., and Zhang, Y., (2013), "Molecular Dynamic Study on Contact Angle of Water Droplet on a Single-Wall Carbon Nanotube (SWCNT) Plate," Appl. Phys.:A, **111** (3): 747-754.

[199] Pavese, M., Musso, S., Bianco, S., Giorcelli, M, and Pugno, N, (2008), "An Analysis of Carbon Nanotube Structure Wettability before and After Oxidation Treatment," J. Phys. Condens. Matter, **20** (474206): 7 pp.

[200] Werder, T., Walther, J. H.., and Koumoutsakos, P., (2002), "Hydrodynamics of Carbon Nanotubes - Contact Angle and Hydrophobic Hydration": Inst. of Computational Sciences Nanotech, **2**: 490-493.

[201] Yuan, Y., and Lee, T.R., (2013), "Surface Sciences,"Springer, Berlin.

[202] Jiesheng Wang, J., Lee, C.H., and Bando, Y., (2009) "Multiwalled Boron Nitride Nanotubes: Growth, Properties, and Applications B-C-N Nanotube and Related Nanostructure, Springer,: 23-45.

[203] Pathak, S., Lim, E. J., and Abadi, P. P. S. S., (2012), "Higher Recovery and Better Energy Dissipation at Faster Strain Rates in Carbon Nanotube Bundles: An in-Situ Study," Acs Nano, **6**(3): 2189-2197.

[204] Ramasamy, N., Thangasamy, S., and Ramalingam, R. J., (2014), "MWCNT/Alumina Nanocomposite Characterization and Toughening Mechanism of Uniform Dispersion," Synthesis and Reactivity in Inorganic, Metal-Organic and Nano-Metal Chemistry, **44** (7): 1050-1053.

[205] Moynihan, T. J., Cho, SC., and Mihakin, A.L., (2000) "Application of the Depth-of-Penetration Test Methodology to Characterize Ceramics for Personnel Protection" Army Research Laboratory, ARL-TR-2219, United States.

[206] Shackelford, J. F., and Alexander, W., (2000), "Materials Science and Engineering handbook, Third Edition, ISBN-1-4200-3840-8, CRC.

[207] Auerkari, P., (1996), "Mechanical and Physical Properties of Engineering Alumina Ceramics ISBN 951-38-4987-2," pp. 26..

[208] Huang, F., and Zhang, L. (2007), "Investigation on Ballistic Performance of Armor Ceramics against Long-Rod Penetration," Metallurgical and Materials Transactions A: Physical Metallurgy and Materials Science, **38** A (12): 2891-2895.